UNIVERSITÀ DELLA CALABRIA

UNIVERSITA' DELLA CALABRIA

Dipartimento di Fisica

Dottorato di Ricerca in

Scienze e Tecnologie Fisiche, Chimiche e dei Materiali

CICLO

XXIX

TITOLO TESI

From basic to advanced: design, fabrication and characterization of functional Terahertz devices

Settore Scientifico Disciplinare: Fisica della Materia FIS/03

Coordinatore: Ch.mo Prof. Vincenzo Carbone

Firma

Supervisore/Tutor: Dr. Roberto Caputo, PhD

Firma

Supervisore/Tutor: Ing. Romeo Beccherelli, PhD

Firma

Dottorando: Dott. Antonio Ferraro

Firma

To Denise

Contents

List of Publications resulting from this thesis work

[1] **A. Ferraro**, D. C. Zografopoulos, M. Missori, M. Peccianti, R. Caputo, and R. Beccherelli, "Flexible terahertz wire grid polarizer with high extinction ratio and low loss," Opt. Lett., vol. 41, no. 9, pp. 2009–2012, 2016.

[2] **A. Ferraro**, D. C. Zografopoulos, R. Caputo, and R. Beccherelli, "Periodical Elements as Low-Cost Building Blocks for Tunable Terahertz Filters," IEEE Photonics Technol. Lett., vol. 28, no. 21, pp. 2459–2462, 2016.

[3] **A. Ferraro**, D. C. Zografopoulos, R. Caputo, and R. Beccherelli, "Broad- and narrow-line terahertz filtering in frequency-selective surfaces patterned on thin low-loss polymer substrates," IEEE J. Sel. Top. Quantum Electron., vol. accepted, 2017, DOI: 10.1109/JSTQE.2017.2665641.

[4] **A. Ferraro**, D. C. Zografopoulos, R. Caputo, and R. Beccherelli, "Terahertz polarizing component on cyclo-olefin polymer," submitted

[5] **A. Ferraro**, D. C. Zografopoulos, R. Caputo, and R. Beccherelli, "Angle-resolved and polarization-dependent investigation of cross-shaped frequency-selective surface terahertz filters," submitted.

[6] **A. Ferraro**, D. C. Zografopoulos, R. Caputo, and R. Beccherelli, "Squeezing narrow band terahertz radiation through extremely subwavelength slits in guided-mode resonant cyclo-olefin thin films," submitted.

Acknowledgements

At the end of this experience, I would write few words of acknowledgement.

I would like to acknowledge Dr. Roberto Caputo and Ing. Romeo Beccherelli, who gave me the opportunity to work with them.

I would say thanks to all my family that encouraged me during all my study.

Least but not last, a very special thanks is for a very exceptional person, my future wife Denise, who followed me in this experience staying always by my side.

Abstract

Terahertz (THz) radiation is an emerging research field with a broad range of potential applications in cross-disciplinary fields spanning material science, pharmaceutical industry, security and safety for screening drugs and explosives, wireless communication in some windows of the atmosphere that allows covering the “last mile”. This frequency range is located inside the electromagnetic spectrum between the microwaves and infrared optics ranges. However, the absence of powerful sources and sensitive detectors have generated the wording “THz gap”. This gap is being progressively filled and now THz sources and detectors with significant enhanced performance becoming available.

In this scenario, the ability to control the properties of THz waves is a primary issue. As in optics, also in the THz regime novel devices able to control some features of the radiation like polarizers, beam splitters, filters, lens, amplitude and phase modulator, waveplates, diffractive optics, and so on are needed. However, in order to give a real boost to the progress of the THz frequency range, these components should be realized at an affordable cost.

For these reasons, the driving concept of the work presented in this research activity is the carry out the entire cycle of development of these devices, starting from their design and its optimization, following their fabrication by means of low cost techniques and finally characterizing them in the THz operating frequency range.

Chapter 1 introduces the main features of THz radiation, describing the systems for generating and detecting the THz waves, its application in various fields and a detailed study of the potential market. Moreover, a survey on the properties of various materials to be used as substrates is reported. After a critical evaluation, the best trade-off material is identified in the low cost, low-loss, and mechanically stable cyclo-olefin polymer Zeonor®, manufactured by Zeon Co. This material is available in thin flexible foils from 13 μm to 188 μm, thick rigid plates and pellets. In order to achieve our aim, in this dissertation all the proposed components were designed and fabricated on thin flexible foils having thickness of 40, 100 and 188 μm.

In chapter 2, we demonstrate wire grid polarizers with extremely low insertion losses and high extinction ratio fabricated on 40 and 100 μm thick Zeonor® substrates by means of standard photolithography techniques. The general design and rules are illustrated by conducting a systematic parametric study on the relevant geometrical parameters. Moreover, one of the proposed polarizers is characterized in two different bending configurations maintaining its high-performances.

Chapter 3 and Chapter 4 focus on two novel types of bandpass filters constituted by an aluminium layer opportunely patterned on the available Zeonor® substrates. In particular, the filters proposed in Chapter 3 are based on the Frequency Selective Surface (FSS) cross-shaped apertures design. For this class of filters, an extensively numerical study and experimental characterization both at normal and oblique incidence are presented. Moreover, the influence of the polarization angle of the impinging THz wave on the devices spectral response is discussed. As in case of the polarizer, the performance of the filters is evaluated in bending conditions as well. The investigation of these filtering components reveals the manifestation of a secondary effect, known as guided mode resonance (GMR) that shows up in presence of a substrate of finite thickness. This interesting concept is the core of Chapter 4. There, we report the fabrication and characterization, also at oblique incidence, of bandpass filters based on this concept that exhibit high transmittance and high quality factor. For all considered filters, their spectral response lays in the two THz communication windows.

Thanks to the flexible substrate employed for their realization, the proposed polarizers and filters can be fabricated with large area electronics and/or roll-to-roll techniques.

Finally, in Chapter 5, we present a low-cost, easy-to-fabricate, and high-quality mechanical tuneable Fabry-Perot filters, made by a simple stacking procedure of Zeonor® thin films. The spacing between successive Zeonor®/air layers is readily controlled by using a simple bi-adhesive tape. The general design and rules are reported.

All the presented devices, exhibiting outstanding performances, can open the route for a novel class of flexible and conformal devices operating in the THz frequency range.

Introduzione

L’intervallo di frequenze dello spettro elettromagnetico denominato terahertz (THz), situato tra le microonde e l’intervallo del visibile, è un settore emergente nell’ambito della Ricerca scientifica. Tale interesse è dovuto alle sue innumerevoli potenziali applicazioni in campi interdisciplinari quali la Scienza dei Materiali, l’Industria farmaceutica, la Sicurezza personale, le Comunicazioni wireless che potrebbero coprire il cosiddetto "ultimo miglio", ed altre ancora. L'assenza di sorgenti e detector ad elevate prestazioni ha generato la dicitura "THz-gap"; tuttavia, dopo intensa attività della comunità scientifica stanno diventando disponibili anche a prezzi relativamente accettabili. In questo contesto, la capacità di controllare le proprietà della radiazione THz è una questione di primaria importanza, pertanto vi è la necessità di sviluppare nuovi dispostivi in grado di manipolare la radiazione THz, con funzionalità equivalenti a quelli comunemente usati in ottica. Tra di essi troviamo, ad esempio, polarizzatori, divisori di fascio (*beam splitter*), filtri, lenti, modulatori di fase e/o ampiezza, sensori, lamine a mezzo e a quarto d'onda, ottiche diffrattive, e così via. Tuttavia, al fine di fornire una reale spinta allo sviluppo ed utilizzo della radiazione THz, questi dispositivi devono poter essere realizzati a basso costo così come avviene per i componenti ottici.

Per tale motivo, la linea guida del lavoro presentato in questa attività di ricerca è lo sviluppo di dispositivi operanti nell’intervallo della radiazione THz, con funzionalità equivalenti a quelle dei corrispondenti dispositivi ottici. Per la realizzazione di tali dispositivi, si è partiti dall'ottimizzazione della loro progettazione, seguita poi dalla loro fabbricazione mediante tecniche a basso costo e infine dalla loro caratterizzazione usando radiazione THz.

Il Capitolo 1 introduce la radiazione THz, descrivendo i sistemi per la sua generazione e rilevazione, le sue applicazioni in vari ambiti disciplinari e riportando uno studio dettagliato del mercato potenziale. Inoltre, viene riportata un'indagine sulle proprietà di vari materiali che potrebbero essere utilizzati come substrati. Dopo una valutazione critica, la scelta è ricaduta sul polimero ciclo-olefinico denominato Zeonor®, avente basse perdite e basso costo. Tale materiale viene prodotto dalla Zeon Co. Lo Zeonor® è disponibile in lamine sottili e flessibili con spessori da 13 a 188 micron, lastre rigide e pellet. Per raggiungere il nostro scopo, tutti i dispositivi illustrati in questa tesi sono stati progettati e fabbricati su lamine sottili e flessibili aventi spessore di 40, 100 e 188 micron.

Nel capitolo 2, presentiamo alcuni polarizzatori (Wire Grid Polarizer) aventi perdite di inserzione estremamente basse e alto rapporto di estinzione. Tali polarizzatori sono fabbricati su substrati di Zeonor®, aventi spessori di 40 e 100 micron, mediante l’utilizzo di tecniche di fotolitografia standard.

Le regole generali del loro funzionamento e l'ottimizzazione del loro design sono illustrate da uno studio dettagliato dei principali parametri geometrici. Inoltre, essendo flessibile, uno dei polarizzatori è stato misurato in due diverse configurazioni di curvatura, mantenendo comunque alte prestazioni.

Nel Capitolo 3 e Capitolo 4, l'attenzione si concentra su due nuove tipologie di filtri passa-banda composti da uno strato di alluminio opportunamente fotolitografato sui substrati Zeonor® disponibili. In particolare, i filtri proposti nel Capitolo 3 si basano sul tipico design a Frequency Selective Surface (FSS), costituito da aperture a forma di croce. Per questa classe di filtri, dopo la procedura di ottimizzazione delle loro proprietà, viene riportata un'ampia investigazione numerica e sperimentale sia ad incidenza normale che obliqua. Viene inoltre valutata l'influenza dell'angolo di polarizzazione dell'onda THz incidente sulla risposta spettrale dei dispositivi. Come nel caso del polarizzatore, la risposta spettrale di un filtro viene analizzata curvandone la superficie su un apposito supporto introdotto lungo il cammino del fascio THz. Lo studio di questi filtri dimostra la presenza di un effetto secondario, conosciuto come *Guided Moded Resonance* (GMR) e dovuto alla presenza di un substrato che sostiene il filtro stesso. Il concetto di GMR è l'argomento principale del capitolo 4. Infatti, quest'ultimo riporta la fabbricazione e la successiva caratterizzazione, anche ad incidenza obliqua, dei filtri passa banda basati su questo concetto. Tali filtri mostrano alta trasmissione e alto fattore di qualità. La loro risposta spettrale è opportunamente disegnata nelle due finestre THz di comunicazione, ovvero a 625-725 GHz e 780-910 GHz.

Grazie al substrato flessibile impiegato per la loro realizzazione, i polarizzatori e i filtri presentati possono essere fabbricati con tecniche usate per la fabbricazione di elettronica di grandi dimensioni e/o con tecniche di roll-to-roll.

Successivamente, nel capitolo 5, presentiamo una seria di filtri di tipo Fabry-Perot accordabili meccanicamente. Tali filtri sono facili da fabbricare utilizzando tecniche a basso costo, essendo fabbricati semplicemente alternando film sottili di Zeonor®. La spaziatura tra strati successivi di Zeonor®/aria viene facilmente controllata utilizzando, nel caso di studio, un semplice nastro bi-adesivo.

Tutti i dispositivi presentati, esibendo prestazioni eccezionali, possono aprire la via per una nuova classe di dispositivi flessibili e conformabili con funzionalità nella gamma di frequenze THz.

Chapter 1:

Terahertz radiation

1.1 Introduction to terahertz radiation

The electromagnetic spectrum between 0.3 – 10 THz is currently referred to as THz radiation, THz waves or T-rays [1], [2]. In this range, the radiation is characterised by a wavelength between 1 and 0.03 mm, a photon energy between 1.24 and 41.4 meV, a Boltzman temperature between 14.4K and 480K, and a wavenumber of 10-334 cm^{-1}, respectively. As a reference, a 1 THz photon has a period of 1 ps, a wavelength of 300 μm, an equivalent Boltzman temperature of 47.6 K, energy of 4.1 meV and wave-number of 33.4 cm^{-1} [3]. Hystorically, Terahertz (THz) radiation has been referred to as "far infrared" or "sub-mm" waves as the THz frequency range is located between microwaves and optics [4], [5], as illustrated in Figure 1. For decades, the main interest was limied to high-resolution spectroscopy and remote sensing where heterodyne and Fourier transform techniques have allowed astronomers and chemists to measure, catalogue and map thermal emission lines for a wide variety of light-weight molecules. Applications outside those specialised fields was hampered by shortage of emitters and detectors able to produce and detect THz signals with reasonable cost and acceptable performances. This shortage has originated the so-called "THz gap". Nowadays, innovative THz sources and detectors are becoming available, with improved performances and relatively low cost, allowing to progress in the production of new instrumentations and measurement systems.

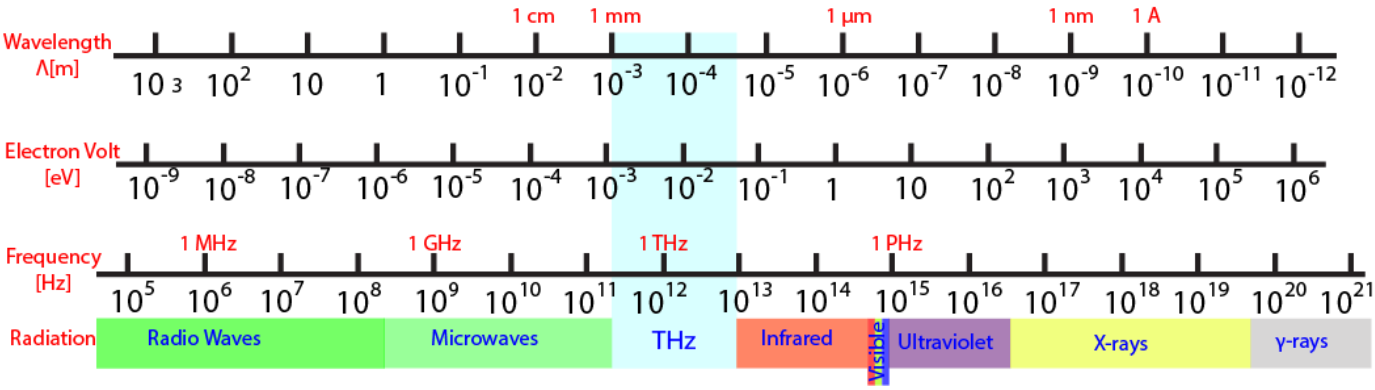

Figure 1: Terahertz radiation inside the whole electromagnetic spectrum.

One of the main advantages of THz wave is that it can penetrate human tissues even if it is not ionizing like X-rays, thus representing an ideal candidate to replace X-rays in diagnostics, the latter with energies in the range 100eV to 100 keV [6]. Another benefit is that materials like paper, plastic, wood, ceramic, clothes are transparent to the wave enabling several novel applications, as will be reported later. However, it cannot pass through metal (it is reflected) and it is highly absorbed by water. This absorption is mainly due to the vibrational-rotational levels of water vapour [7].

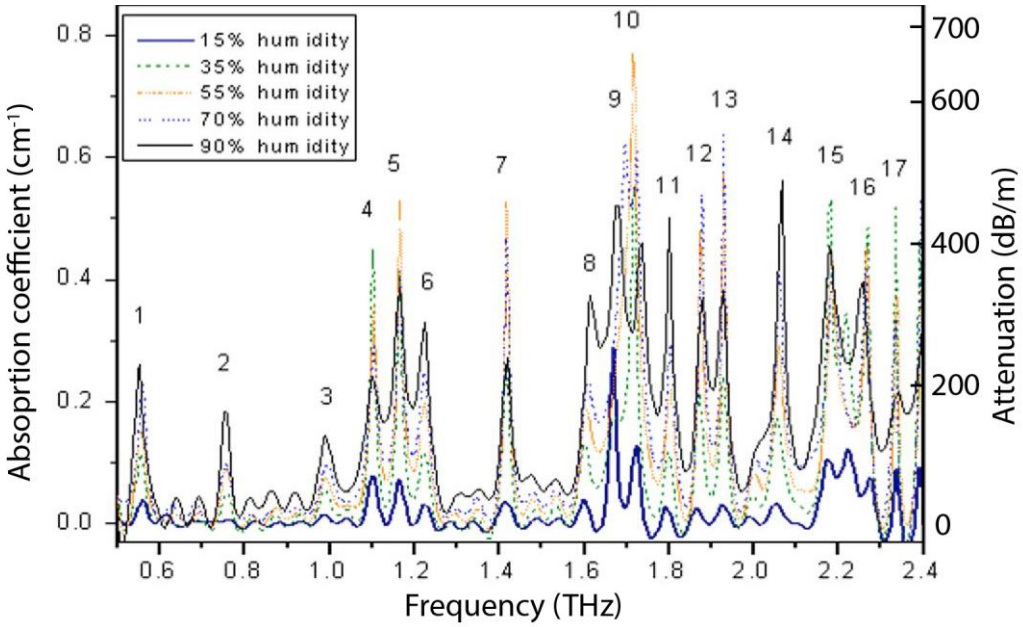

Figure 2: Absorption coefficient absorption and attenuation of the atmosphere with five different percentage of relative humidity at 296 ±2 K; adapted from [8].

Figure 2 reports the absorption coefficient of atmosphere with five different rates of relative humidity (RH) at room temperature of 296 ±2 K (23°C), from 15 to 90 RH %, in the range 0.5 to 2.4 THz [8]. As observed in Figure 2, the absorption of the THz radiation increases by increasing the relativity humidity, representing therefore an important parameter to deal with. Moreover, Figure 2 shows a series of "sharp" absorption lines, whose number and width depend, as before, on the humidity percentage. Two spectral windows, with almost 150-200 GHz width, are present below 1 THz and remain usable also at high humidity. One spans over [0.6 and 0.75] THz range, and the other between is 0.8 and 1 THz. Above 1 THz the presence of absorption lines is predominant and there are not practically useful spectral windows for Telecom. However, this part of spectrum is of particularly interest since many molecules have their fingerprint in this region and may be useable at short range. Atmosphere purged with nitrogen represents the most common and easily implemented solution to solve the humidity absorption. An alternative is represented by a vacuum chamber with a rotary vacuum pump.

1.2 Terahertz market

The focus on THz radiation in the last decade is reinforced by various studies on THz papers, patents and market trend [9]–[14]. In order to have a reliable idea of the phenomenon, we performed an analysis on the Scopus database [15] by searching how many papers contain the word “terahertz” as topic (title, abstract, key word) in the timeframe from 1973 to 2015, data reported in Figure 3. The latter shows an exponential growth of the number of paper started, essentially, around 2000. Only in 2015, more than 3500 papers have been published and this number should increase over the year.

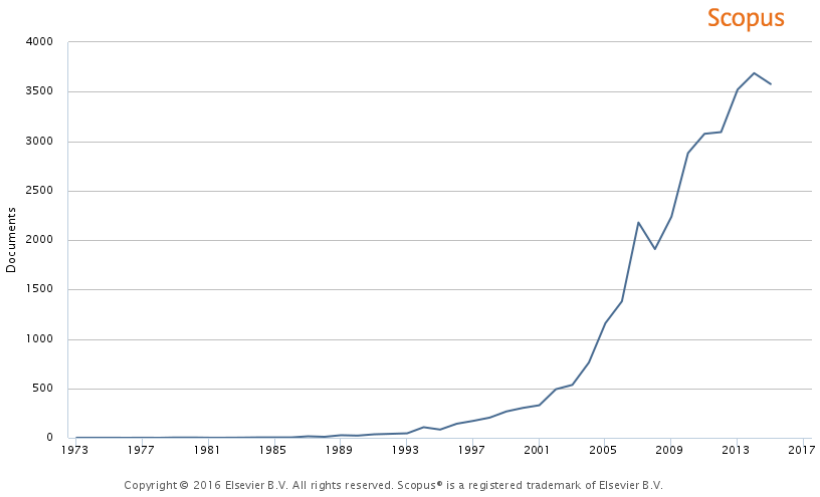

Figure 3: Number of published papers on terahertz paper versus year. Figure from “Scopus”.

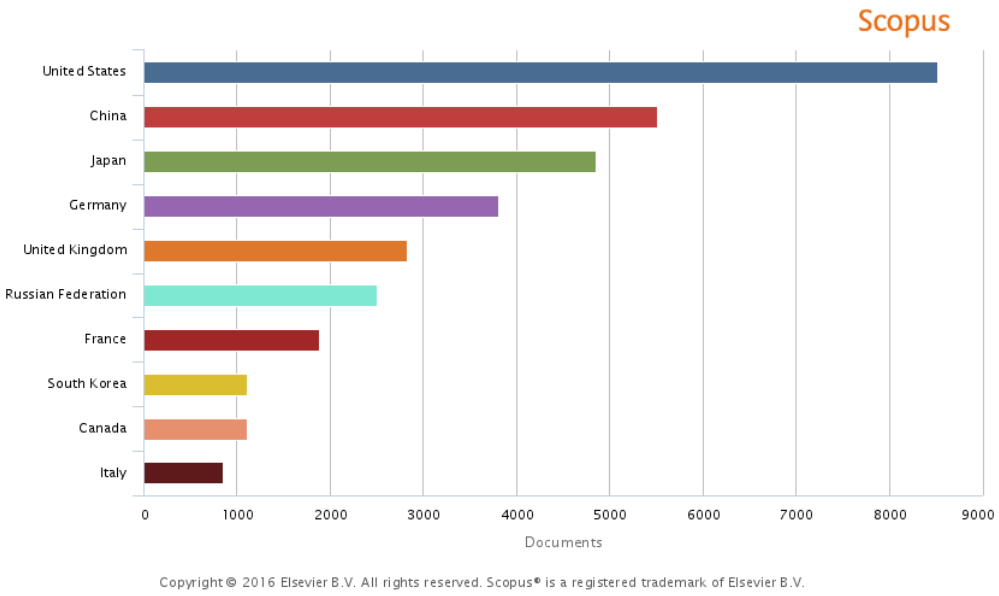

Figure 4: Number of published papers on terahertz paper by country. Figure from “Scopus”.

From the same data collection, we extracted information on the country performance on publishing papers dealing THz. At the first position, as expected, we find USA with more than 50% of the papers,

followed by China and Japan, the latter is a pioneer in science and technology of the THz range research from the very beginning. Germany ranks forth; indeed, most THz company/distributors have their headquarters there.

Another significant factor explaining the great attention of the scientific community on the THz field can be found on patents analysis, which gives an indication from an industrial and commercial point of view. We collected data, until 2015, from "Lens.org" free patent website [16] by searching the key word "terahertz", Figure 5 and Figure 6 report the patent versus application years and versus jurisdictions, respectively. From Figure 5 a positive trend of the number of patents year by year is observed, with more than 2000 patent applications in 2015. Concerning the number of patents for country, the same trend of Figure 4 is observed.

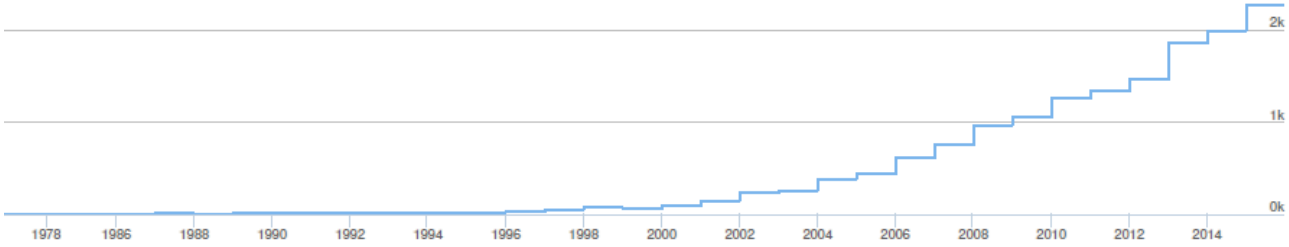

Figure 5: Terahertz patents versus years of publications. Figure from "Lens.org".

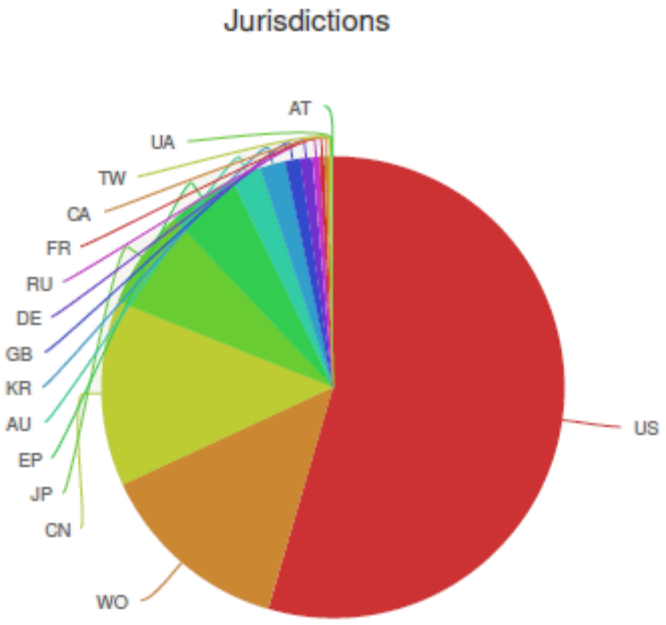

Figure 6: Terahertz patents by jurisdictions. Figure from "Lens.org".

The growing number of patents leads to an increased global THz market as shown in Figure 7 that reports data from a recent TEMATYS report on "Terahertz Components & Systems: Technology and Market trends UPDATE 2016" [10]. The report analyses the global THz market from 2015 and

provides a forecast until 2020. In 2015, the market was about 40 M€; it is expected to double to almost 100 M€ in five years, with a 16% compound annual growth rate (CAGR).

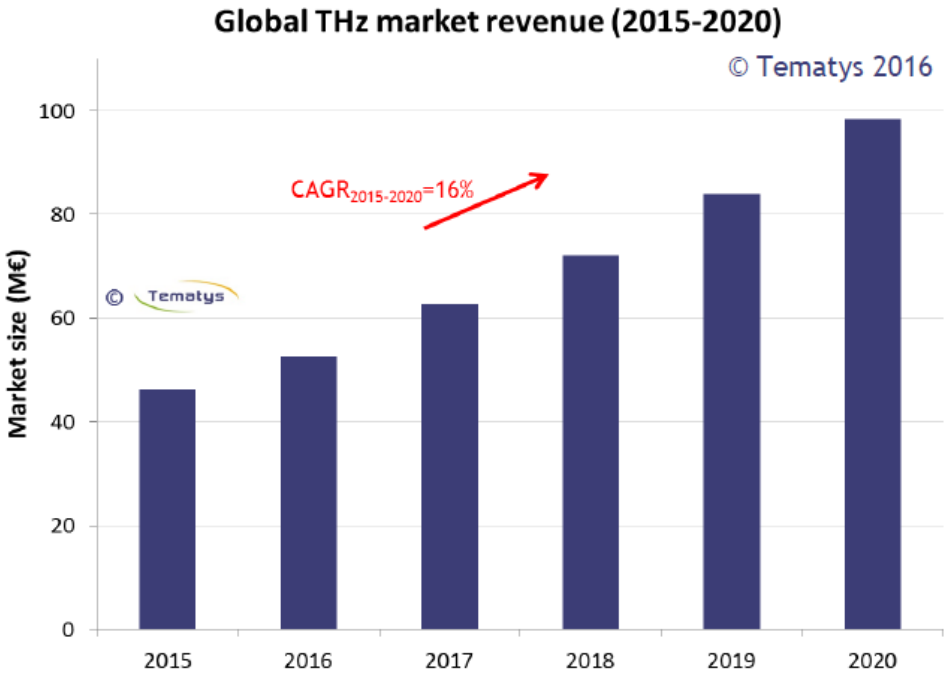

Figure 7: THz market size in millions of euro versus year. Figure from TEMATYS report on "Terahertz Components & Systems: Technology and Market trends UPDATE 2016".

Even if we are not in a blue ocean, the THz frequency range represents a very good perspective for researchers, especially for those willing to transfer research technology into spin-off companies.

1.3 Terahertz applications

The THz frequency range is under intense investigation due to its applications in cross-disciplinary fields, such as secure short-range communications, life-science, cultural heritage, defence, safety and security [17]–[24]. Among these, which is the killer application for enabling a real commercialization of products/setup based on THz wave? In other words, as cited in [25], what THz wave can do cheaper, do more of, or do better than other optical or microwave techniques ? In this section, we briefly introduce some applications of terahertz technology and try to answer this question.

One and well established application of THz radiation in material science is THz time domain spectroscopy (THz-TDS). This is a spectroscopic technique that has the striking advantage of recovering both amplitude and phase of the signal at the same time. This unique feature gives the possibility to extract the complex refractive index of the material and hence its real (refractive index) and imaginary components (from which the absorption coefficient can be extracted) [26]–[28]. The extraction of these parameters is not easy and many researchers work on developing novel and

improved algorithms that take into account all the possible problems, such as Fabry-Perot effect, multilayer, liquid and so on [29], [30]. Furthermore, most of materials often utilized in optics, such as glass, some polymer, metal oxides (ITO), are not suitable for THz wave because of their absorption and reflection of the input THz radiation [31], [32]. In the following of this thesis, we will give a review of the most common polymers used in this frequency range. On the other hand, there are some materials that are opaque in the visible range but transparent at THz such us fabrics, cardboard, some plastics, some human tissue and so on. These unique features can be implemented in process control methods of industry, for example automotive, aeronautics, pharmaceutical and so on, especially where non-destructive testing (NDT) are needed [22]–[24], [33]–[48]. However, the implementation in inline production processes is not easy for several reasons such as complex systems and high cost; thus only few applications really can be adopted in industrial processing. For instance, one potential application is paint thickness measurement in multilayer structures (supported by the high skin depth of THz wave) [49]–[51], since the THz technique has the advantage to provide information on a variety of coating films, thickness of each layer in a multilayer, map distribution and so on. Wood products are transparent to THz radiations, and sensitivity to fibre orientations with good resolution is achieved [17], [52]. In the aeronautics industry, THz imaging is employed to examine composite materials, especially to find defects as external material inserts, delamination and so on [53], [54]. In the pharmaceutical industry, THz radiation offers several benefits as individual fingerprint of active pharmaceutical ingredient (API), deep skin depth, non-ionizing energy, identifications of coating thickness and uniformity, tablet density and integrity, pharmaceutical quantifications, polymorphism and so on [55]–[61]. Related to NDT, cultural heritage represents another fascinating field of applications. THz wave possess higher skin depth with respect to IR or visible light (Figure 8), therefore it is possible to retrieve information about underlying layers which possesses unique fingerprint in the THz range [17].

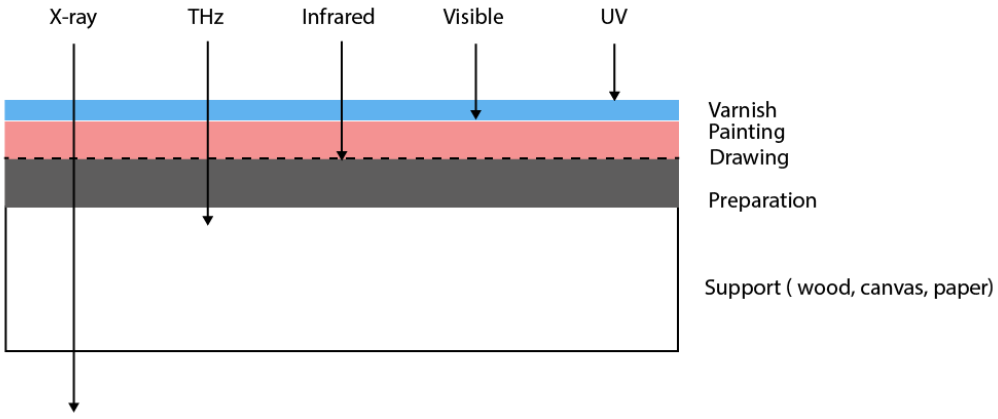

Figure 8: Electromagnetic wave skin depth comparison.

This is particularly advantageous in analysis and restoration of paintings non-destructive cross-sectional imaging and more information about the material utilized by the artist can be obtained [48], [62]–[66].

Some materials possess distinctive feature at THz, like a "fingerprint" and this property is used for detect and identify explosive and drug. THz waves can then be applied overall in the security and defence field, as identification of concealed weapons, land mines and so on. Moreover, since THz is health safety, it is possible to use it for scanning people at security check desk [21], [67]–[71].

In this context, we can also include life-science applications especially for bio-sensing and for imaging. In the first case, the unique fingerprint of the molecules is analysed. In the latter case, the research community has put many efforts in order to develop imaging systems that could replace X-ray imaging. The reason lies in the fact that THz radiation is not ionizing, since it excites only vibrational and rotational states, not altering the electronic state of molecules, therefore is safer than X-ray [28], [55], [72]–[78].

There is an increasing demand of high data rate telecom communication, especially for the wireless one. In fact, the exponential growth of the data traffic, especially for internet protocol, is due to the increasing number of the devices able to receive and transmit data. Today, the radio-frequency wireless communication conventionally uses a carrier frequency of maximum 60 GHz with a bandwidth of 7-9 GHz that is almost saturated, therefore the use of higher frequency is necessary to meet the end-user requirements [79], [80]. However, the atmospheric attenuation of THz waves represents a great obstacle. For this reason, the optimistic applications lie in short range communication systems such as, home, office or conference room wireless networks, device-to device communication and so on [19], [81]–[86].

1.4 Terahertz generation and detection

The principal reason that restricted the investigation of the material interaction in THz frequency region, as already said, is due to the technological limitation of source and detector. Regarding the sources, generally, they can be divided in two classes: Time Domain Generation and Frequency Domain Generation. These usually result in broadband and narrowband spectra, respectively. We briefly introduce these two classes, starting from the Time Domain one [3], [87].

Figure 9 reports a schematic representation of a THz broadband system, where a pulse of a femtosecond laser, usually < 100 fs and λ around 1550 or 800 nm, impinges on a beam splitter and it is divided in two portions, *beam1* and *beam2*. The former is incident on the DC-biased emitter where a current spike is photo-generated, and thus THz pulse is emitted, which is directed towards the

sample and then focused on the detector. Meanwhile, the other laser pulse travels through a mechanical delay line and successively focused on the detector. This part of the process is of paramount importance since it allows recording the THz signal as a function of time. The motivation lies in the principle of operation of the THz detector, in fact it can acquire the THz signal only when both the THz pulse and laser pulse in *beam2* impinge at the same time on it, being the detected electrical signal proportional to the electric field of the THz pulse. Therefore, as a consequence of changing the time at which *beam2* impinges on the detector the time at which the THz pulse is recorded is different. Subsequently, by applying a Fast Fourier Transform (FFT) to the registered signal the amplitude and phase of the THz pulse is obtained. For this kind of system, various sources are available as for example photoconductive antennas (PCA), nonlinear crystals, photo-Dember effect emitters, electron accelerator and so on, where the first two are most used ones. We will give a briefly introduction of some of them.

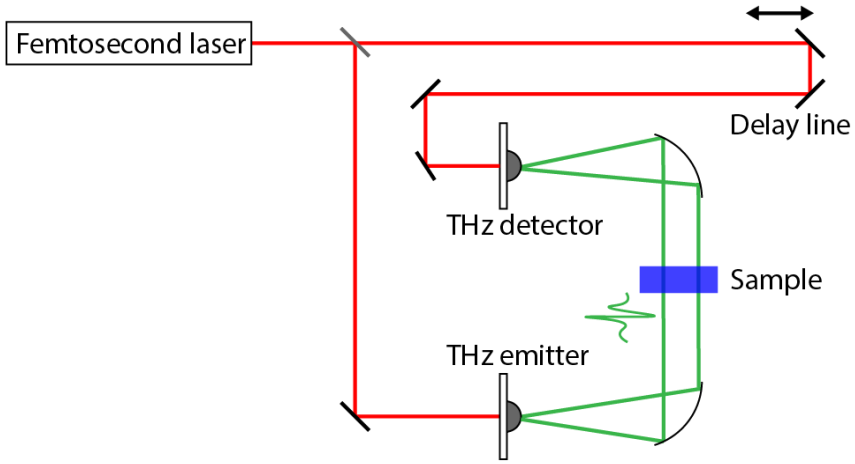

Figure 9: General scheme for THz time domain system with reflective optics. Equivalent arrangement can be assembled with refractive/diffractive optics.

In the PCA, the laser radiation activates an optical dipole switch that is part of the whole antenna. Various switch geometries are possible. However, stripe lines having a gap between them, represent the most common ones [88]. Other options are bow-ties, offset dipoles and Hertzian dipoles. The laser pulse is focused on the gap while a DC bias electric field is applied across the gap. When the optical pulse impinges on the gap, it generates photo-excited carriers which are successively accelerated by the bias voltage. The generated transient electrical current produces an ultra-short electromagnetic pulse radiation in the THz range. Regarding the materials utilized for the substrate of the PCA are semiconductors with high mobility but short recombination time such GaAs, LT-GaAs, InGaAs and InP represent the most utilized ones [88]–[91].

As already stated, crystals with nonlinear optical properties represent another common source of THz radiation and ZnTe is the most representative. Other crystals are available as $LiNbO_3$, InP, GaAs,

GaP, GaSe, $LiTaO_3$. Moreover, organic polymer and crystal can be used such as APC (amorphous polycarbonate), DCDHF (dicyanomethyllenedihydrofuran), DAST (4-N,N-dimethylamino-4′-N′-methyl-stilbazolium tosylate) and MBANP (-)2-(α-methylbenzylamino)-5-nitropyridine [3]. In a non-linear optical medium, the polarization induced in the medium is related to the incoming electric field and is described by a series of power terms of increasing order. In this context, only the second-order terms are considered. When an optical radiation impinges on a nonlinear crystal, its electric field components induces a nonlinear polarization response that depends on the angle between the incoming radiation and the crystal axes. We refer to optical rectification when a constant optical electric field produces a static polarization. However, for generating THz radiation a pulsed optical radiation is used, therefore the induced polarization is time dependent and is proportional to the envelope of the optical pulse. This dependence of the polarization is responsible of the THz signal [3], [92], [93].

A typical TDS spectrum of THz radiation generated by PCA is reported in Figure 10, on the left in time domain while on the right in frequency domain achieved after a Fast Fourier Transform (FFT). It is possible to notice in Figure 10, right side, that the spectra have a peak at low frequency that decreases by increasing the frequency, reaching the noise level.

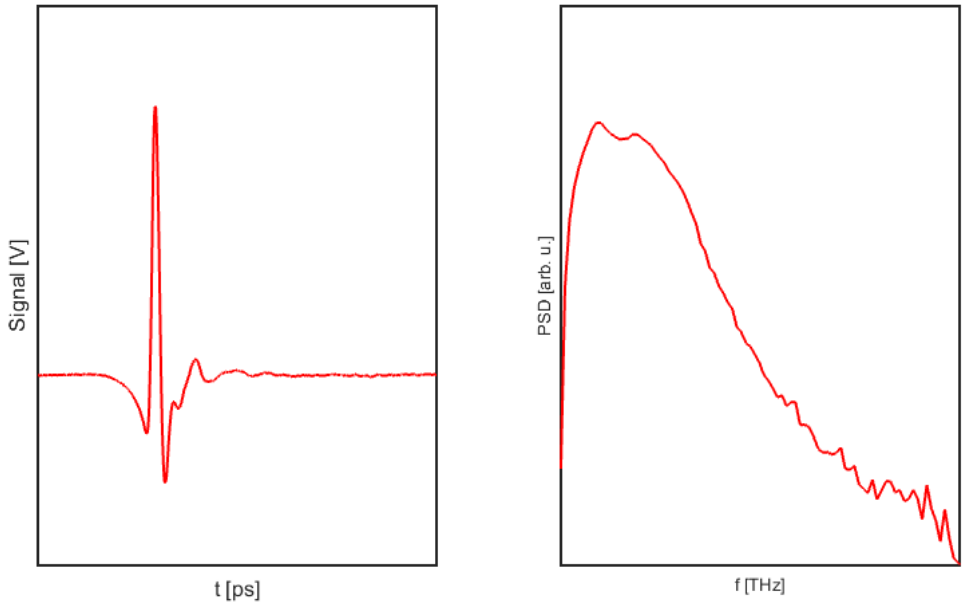

Figure 10: Typical Terahertz spectrum in time domain (left) and frequency domain (right).

Concerning the electron accelerator method, we briefly present the way to use a synchrotron for generating THz broadband radiation. An ultrashort laser pulse impinges on a GaAs surface generating ultrashort electrons clusters, successively accelerated to relativistic speed. These electrons produce THz radiation when they are steered using magnetic field, namely the Bremstralung effect[94].

After Time Domain generation, we introduce now some of the sources available for Frequency Domain generation, also known usually as Continuous Wave (CW) generation. Noticeable, examples are Photomixing, Quantum Cascade Laser (QCL), Free Electron Laser (FEL), Microwave Frequency Multipliers, and so on.

A photo-mixer represents the alter ego of PCA in the contest of Frequency Domain generation. Figure 11 illustrates a scheme of this class of system where two optical CW lasers with two adjacent different frequencies, ω_1 and ω_2 respectively, are focused on a phot-mixer interfering each other and generating a beat signal at the frequency difference $\omega = \omega_1 - \omega_2$. The photo-generated current oscillates at the frequency ω that impinges on an antenna integrated in the photo-mixer producing a THz wave. The latter can be modulated by tuning the frequency of one laser. The photo-mixer is the core of the system and it is composed of a metal-semiconductor-metal structure, where one between GaAs, LT-GaAs and InGaAs constitutes the semiconductor layer. As in the case of PCA, various antenna designs, such log-spiral, dipole antenna and bow-tie, have been utilised [17], [90], [95], [96].

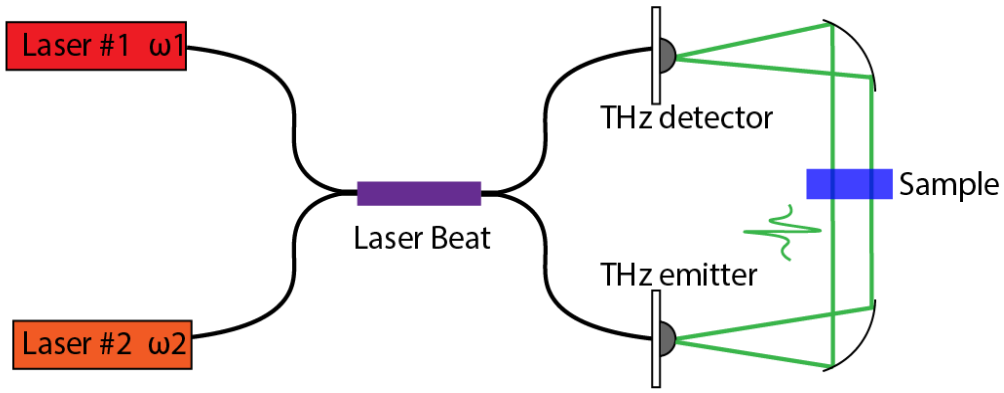

Figure 11: Example of THz Frequency Domain system representing a Photomixing setup scheme with reflective optics. Equivalent arrangement can be assembled with refractive/diffractive optics.

Quantum cascade lasers (QCL), first demonstrated in 1994 [97], have the potential to become the most common THz source if they could be made cheap, powerful and operating at room temperature [98]–[101]. Much effort is been spent by the research community to increase the operating temperature, however the highest reached is around 225K [102]; at the moment this denotes the major drawback hampering the potential of this technology; though some novel approach are being pursued to raise the temperature [103]. In a QCL, laser emission results from inter-sub-band transition of electrons in semiconductor heterostructure quantum wells. The latter is made up of repetition periods of wells and barriers where each period is separated by an injection region. The general concept is to force the electron to emit photons inside the well in a transition from the upper energy level to the lower one. Once the photon is emitted the electron, through the injection region, is injected in the upper energy level of the following well and the same process occurs. Thus, one electron produces

many photons. This is in contrast to what usually happens in a common semiconductor laser where an electron-hole pair emits only one photon. The thickness of the quantum well and barriers determines the photon energy and therefore the emitted wavelength without the need to change the materials stoichiometry of the active region.

The other THz source that we briefly discuss here is the expensive free electron laser (FEL). In this case, free electrons, with relativistic speed, travel inside a laser cavity where a sinusoidal magnetic field is present. This field induces a sinusoidal motion of the electrons releasing monochromatic photons at THz frequency [104].

Frequency multipliers are based on Schottky diodes acting as the equivalent of nonlinear crystals. In fact, utilizing the reactive and resistive non-linearity of the diode, they generate an output wave having a frequency that is the multiple of the incoming one. Their use in the THz region is due to the fact that microwave source at around 100 GHz are easily available [105].

After the discussion on various THz source we briefly introduce some THz detector , such PCA, nonlinear crystal, heterodyne detection, bolometer; however others detector configurations are available [106].

PCA and nonlinear crystals can be employed for detecting THz radiation in a similar manner as discussed above concerning the generation. In the first case, the THz pulse accelerates the photo-excited carriers generated in the detector by the optical *beam2*. The generated current is converted to voltage that is detected usually with a lock-in amplifier. As for the generation case, the delay line permits to map the THz signal over time. Also in the second case, i.e. nonlinear crystal, the concept is similar to the generating one above described. Stickily speaking, in this situation the THz signal impinging on the detector induces a proportional change in the polarization of the optical pulse. This variation is analysed through a photo-diode obtaining a THz signal [107], [108].

In the heterodyne detection process a mixer, typically a Schottky diode, allows the beating of a reference signal (known as local oscillator) with the unknown incoming radiation generating signals at the sum frequency and difference frequency of the original frequencies. The sum frequency is absorbed (at least to some extent), while the signal with the difference frequency is detected. Thus, the amplitude of the detected signal is proportional to the amplitude of the incoming radiation [109]. This is the optical extension of the heterodyne detection long used for radio signal, where the sum frequency is filtered out by parasitic reactance.

The bolometer is one of the possible thermal detectors utilized in the THz frequency range. The main part of the bolometer is an broadband absorbing element typically made of metal or semiconductor (Si, Ge). The incoming radiation produces an increase of the temperature causing a variation of the electrical resistance of the active element. The detection is based on measuring this variation [110].

To sum up there is no a unique choice for implementing THz systems, each source and detector possesses benefits and disadvantages that have to be evaluated depending on the user requirements. For instance, time domain systems show a broadband THz signal, very fast acquisition time but low spectral resolution; it is usually used for materials spectroscopy or thickness measurement. Applications that require high spectral resolution employ frequency domain systems even if the time speed is lower with respect to the time domain one.

1.5 Materials with low loss in the terahertz range

As mentioned in the previous paragraph, the absorption of materials represents one important parameter to be considered when dealing with THz devices. Therefore, it is of paramount importance to find a low loss material suitable as a substrate in the THz frequency range for passive components and components incorporating some type of dynamic modulation as liquid crystal [111], [112], graphene [113]–[115], and so on. For this reason, a literature survey was conducted and the results are illustrated in Figure 12 and Figure 13, which report the absorption coefficient of several materials in the range between 0.3-2 THz, data collected from [4], [26]–[28], [83], [116]–[123].

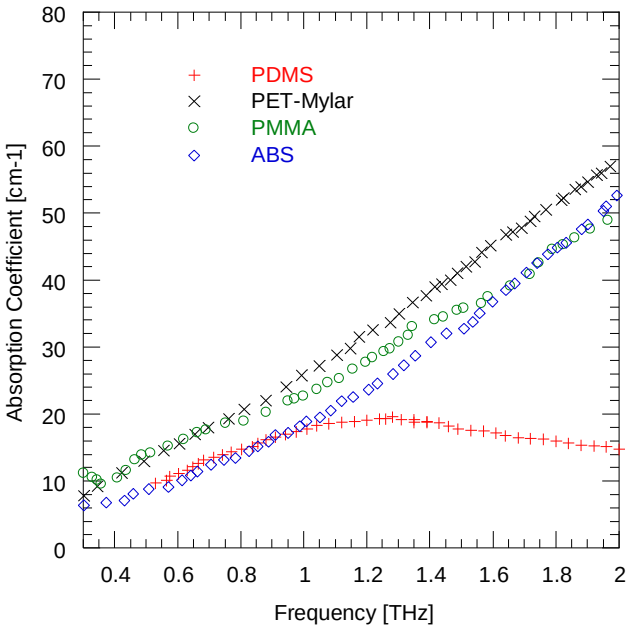

Figure 12: Terahertz absorption coefficient of Polydimethylsiloxane (PDMS), Polyethylene terephthalate (PET), Poly(methyl methacrylate) (PMMA) and Acrylonitrile butadiene styrene (ABS). Reprocessed from data extracted from [4], [26]–[28], [83], [116]–[123].

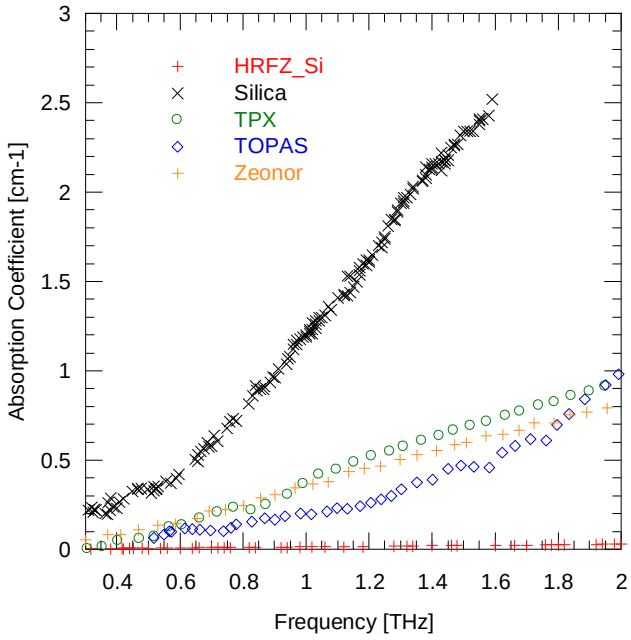

Figure 13 Terahertz absorption coefficient of High Resistivity Floating Zone Silicon (HRFZ_Si), amorphous Silica, TPX®, Topas® and Zeonor®®. Reprocessed from data extracted from [4], [26]–[28], [83], [116]–[123].

In particular, Figure 12 reports the data for Polydimethylsiloxane (PDMS), Polyethylene terephthalate (PET), Poly(methyl methacrylate) (PMMA) and Acrylonitrile butadiene styrene (ABS), while Figure 13 for High-Resistivity Floating Zone Silicon (HRFZ-Si), Silica, Polymethylpentene (TPX®), Cyclic olefin copolymer (TOPAS®) and Cyclo-olefin polymer (Zeonor®). Among these, HRFZ Silicon presents the lowest absorption coefficient followed by three polymers, TOPAS, TPX and Zeonor®. For all these four materials, the attenuation at 1 THz stays below 0.5 dB/mm. Unfortunately, the exact composition and molecular weight of these low loss polymers are trade secrets and is not possible to retrieve a general understanding of the causes of the different absorption coefficient. However, other parameters like cost, compatibility with fabrication processes, water absorption and so on are also relevant for an accurate decision. Regarding the cost, HRFZ Silicon is the most expensive ones, typically more than €100 for a 2'' wafer. The polymers, are less expensive and are pellets sold typically for less than 100€/Kg. Among the TPX®, TOPAS® and Zeonor®, following a market survey we found that the latter is the cheaper one and it is available, also, in plate of various millimetre or in thin film. In the latter cases, the substrate is ready to be used. Moreover, its water absorption is nearly as low as that of simple glass. Finally, they are compatible with all solvents and temperature changes involved in the fabrication processes for photolithography and wet-etching of metals [124]. Hence, we focused our attention on Zeonor® produced by Zeon Co. The latter is a cyclo-olefin polymer (COP) with excellent combination of optical and electronic properties enabling its use in various application fields such as lighting, automotive, electronics, bioscience, packaging and so on [124]. Its synthesis is illustrated in Figure 14 [125].

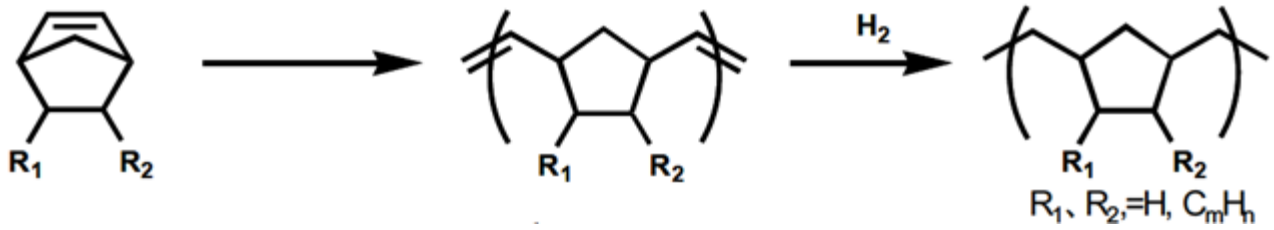

Figure 14: Synthesis of COP from [125].

We were kindly provided by Zeon Co. with thin foils having thickness of 40, 100 and 188 μm and 2-mm thick Zeonor® plate. The latter was characterized by means of THz time-domain spectroscopy (THz-TDS) in transmission mode with a collimated beam in the range 0.3-2 THz by using the available Menlo System TERA K15 [89], an all fiber-coupled spectrometer. In order to prevent absorption of THz radiation by water vapour, the measurements have been conducted in an atmosphere purged with nitrogen (N_2). The power transmittance of the sample is normalized to the one in absence of the sample. Then, by using the software provided with the spectrometer and by applying Fast Fourier Transform (FFT) to the normalized signal, it is possible to retrieve the material properties, namely the refractive index and the absorption coefficient.

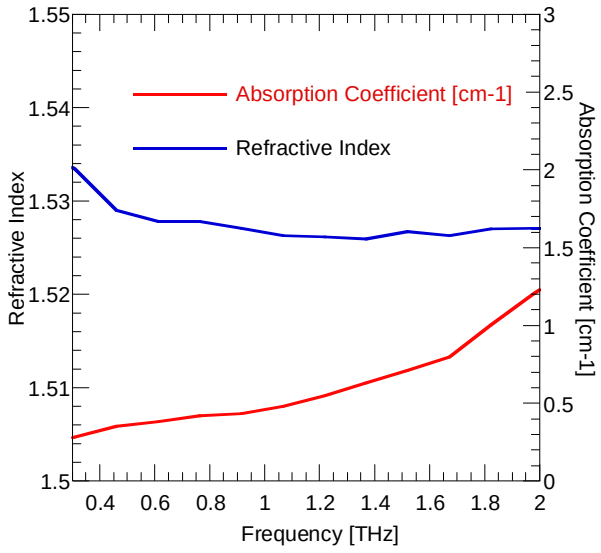

Figure 15: Material properties of a 2-mm thick Zeonor® plate characterized by means of THz time-domain spectroscopy.

The extracted refractive index is equal to 1.525 with minor dispersion in the spectral range under investigation while the absorption coefficient increases almost linearly from 0 to 1.3 cm^{-1} in the 0.3 to 2 THz range. This corresponds to an almost constant imaginary part of the refractive index of approximately 10^{-3} and a loss tangent of approximately $1.3 \cdot 10^{-3}$. Given their very low absorption, it has not been possible to characterize 100 μm thick Zeonor® foils individually because the difference

between the reference signal and the sample measurement were comparable to the noise level of the THz signal. As such, a stack of ten of these foils was assembled and measured as well. The material parameters are fully consistent with the accuracy in estimating the foils and slab thicknesses.
To sum up, for the above-mentioned reasons, Zeonor® thin films have been chosen as substrates for in all cases reported in this dissertation.

1.6 Conclusion

In this chapter, we have reported an overview on the terahertz frequency range that, as already mentioned, lays between the microwave and infrared optics ranges. Therefore, THz sources and detectors are developed by levering techniques from both sides of the electromagnetic spectrum, as illustrated above.
Moreover, we described applications of THz frequency range in several fields, such as life-science, materials science, telecommunication, cultural heritage and more. Furthermore, from the conducted analysis on the THz market, it is realised that the growing interest of scientists is associated with an increasing THz market size. However, this research field is relatively new and although quite some efforts have been devoted to the development of sources and detectors with improved performance and relatively more affordable cost, much work remains to be done. At the same time, the development of THz components with functionality equivalent to those easily available in optics, but at an affordable cost, such as polarizer, polarizing beam splitter, beam splitters, filters, phase shifters, absorbers, lenses, diffractive optics, and so on. Hence, during my research activity, the main focus was the realization of a new class of flexible and conformal THz devices both static and with dynamic control. We developed a flexible wire gird polarized, two novel classes of bandpass filtering elements, bandstop filter and, in conclusion, tuneable bandpass filters are much required to fully exploit the potential of THz waves. Hence, we performed a detailed analysis in order to find the best substrate choosing in the end the cyclo-olefin polymer Zeonor®, as reported above. Then, by means of finite-element method (FEM) implemented in commercial solver several designs were analyzed, among these the ones with the best performance were selected for the fabrication. The latter was mainly performed using standard UV-photolithography. Successively, the fabricated components were characterized using terahertz time domain spectroscopy system.

Chapter 2:

Flexible terahertz wire grid polarizers

Part of the work herein reported is reprinted/adapted, with permission, from [A. Ferraro, D.C. Zografopoulos, D. C., M. Missori, M. Peccianti, R. Caputo, and R. Beccherelli, R.: 'Flexible terahertz wire grid polarizer with high extinction ratio and low loss', Optics Letters, 2016]

and

Part of the work herein reported is reprinted/adapted, with permission, from [A. Ferraro, D.C. Zografopoulos, R. Caputo, and R. Beccherelli, R.: 'Terahertz polarizing component on cyclo-olefin polymer, submitted, 2017]

2.1 Introduction

A particular feature that characterises THz sources such as quantum cascade lasers [100], [101], diode based frequency multiplier [90], [105], vacuum tubes (BWO, Gyratron, FEL etc) [3], [87] is that their output radiation is polarized to some extent. Terahertz time domain spectroscopy (TDS) setups often employ a low conductivity GaAs antenna, which radiates a field intrinsically polarized along the axis of the antenna. Hence, there is often a necessity to process, control and analyse the state of polarization of the THz beam. While in optics, prism polarizers offer 50-60 dB extinction ratio and low insertion losses and iodine loaded stretched polymer offers 30-40 dB at a negligible cost, no equivalent devices exist at THz mainly due to material absorption. Various THz polarizers have been so far developed using different approaches, for instance, based on aligned carbon nanotubes [126], nematic liquid crystals [127], tunable metamaterials [128], thin-film metallic grating [129], [130] or spoof surface plasmon polaritons [131]. Among these, the majority is based on some configurations of metallic wire grids, which may be either free-standing or deposited on a dielectric substrate. In most respects, a wire grid polarizer (WGP) with a deep sub-wavelength pitch can be thought of as the

simplest metamaterial device with sub-wavelength features, whose anisotropic performance stems from the polarization-dependent properties of the effective medium composed by the metallic grid and the surrounding isotropic dielectric. Free-standing THz WGPs that are already commercially available offer high transmittance [132], [133]. However, they are expensive and mechanically fragile. Conversely, wire-grids patterned on a dielectric substrate are less expensive and easier to produce, because they can be fabricated using standard photolithography, as well as various large-area techniques. In [134] an extinction ratio (ER) of 35 dB at 0.5 THz is achieved, but the transmittance of the polarizer is approximately 50% owing to the high reflectivity of the Si substrate. In [135], Pickwell-MacPherson's group achieved an ER between 20 and 49 dB in the 0.2-2 THz range and an insertion loss (IL) lower than 1 dB. Nevertheless, the employed fabrication process relies on dry bulk micromachining of a silicon wafer. As such, it requires a significant amount of process consumables. Although a wet-etch process may reduce the cost, the silicon based process is intrinsically constrained by the size of crystalline wafer. A technique to improve the ER performance of the WGP is to fabricate a bilayer [136], or multilayer structure [137]. In both cases two or more single WGPs are stacked together, thus increasing the number of fabrication steps and hence the overall complexity and cost. Takano et al [138] have fabricated a WGP on a flexible substrate with 140 nm pitch by means of nano-imprinting but the device shows significant losses.

In our case, we experimentally demonstrated an Al-based THz WGPs with very low IL and high ER [139], [140] fabricated on a cyclo-olefin polymer substrate (Zeonor®) having very low loss and a high mechanical flexibility. A systematic numerical parametric study was initially performed, by varying the substrate thickness, the wire grid period and fill factor, in order to identify the structures with a favourable trade-off between insertion losses and achievable extinction ratio. Subsequently, WGPs were fabricated on both 40 and 100 μm thick Zeonor® foils. Although standard photolithography techniques have been used for this proof of concept, the polarizers can be fabricated with large metal coaters and/or roll to roll patterning techniques [141], [142] over large area at a negligible cost. Most importantly, the possibility to bend and conform the fabricated WGP over a rigid surface can open the route for new kinds of integrated and flexible THz devices.

2.2 Design

The investigated polarizer layout is reported in Figure 16 where its geometrical parameters *p*, *w* and *d* respectively represent the pitch of the metallic stripe grating, the width of the metal stripe and substrate thickness. Figure 16 illustrates the operational principle of a wire grid polarizer (WGP), where the field components of an unpolarised incident wave impinging on it experience a different

behavior. In particular, the polarization component perpendicular to the metal stripes ($E_{\perp}$) is transmitted, while the one parallel to the metal stripes ($E_{\parallel}$), that is back reflected, represents the unwanted polarization component.

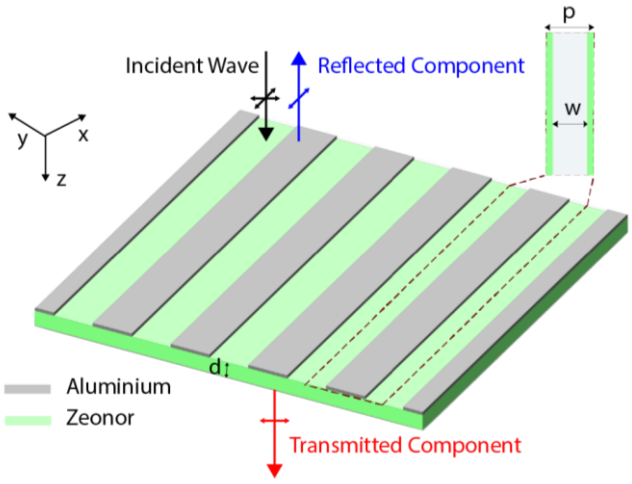

Figure 16: Schematic layout and definition of the geometrical parameters of the investigated polarizer. The Al thickness is 200 nm.

The performances of the polarizer are defined by its ER and IL, expressed as

$$ER = 10 \log_{10}(T_{\perp}/T_{\parallel}) \quad (1)$$

and

$$IL = -10 \log_{10}(T_{\perp}/T_{N_2}); \quad (2)$$

where $T_{\perp}$ and $T_{\parallel}$ are the transmitted power coefficients for the field components respectively perpendicular and parallel to the metallic stripes, while T_{N_2} is the power transmitted in absence of the polarizer.

A systematic numerical study was conducted in order to find the best performance of the WGP in terms of ER and IL by means of the finite-element method (FEM) implemented by means of the commercial solver COMSOL Multiphysics©. Aluminium was modelled as a Drude medium, with plasma frequency ω_p= 2.243x10^{16} rad/s, and electron decay rate γ=1.243x10^{14} rad/s. The incoming THz wave impinges perpendicularly (at normal incidence) on the WGP and the transmission coefficients are calculated for the E_x and E_y components of the electric field (Figure 16) which respectively represent the reflected and transmitted component.

The performances of the WGP depend on its geometrical parameters, namely its pitch (p) and the width of the metallic stripes (w). From those parameters, the fill factor (F) is derived, defined as the ratio between the stripe width and the pitch of the one-dimensional periodic lattice ($F=w/p$). Furthermore, also the Zeonor® substrate film thickness (d) has a relevant effect on the properties of the polarizer, as reported in this paragraph. Both the period and the fill factor influence the polarizer

extinction ratio; when the period increases, the extinction ratio decreases, while the opposite happens by increasing the fill factor. On the contrary, the insertion losses decrease while decreasing period and/or fill factor values.

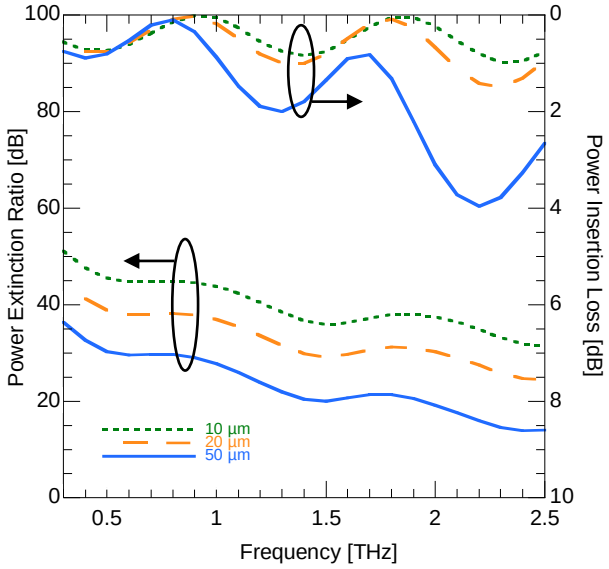

Figure 17: Numerical investigation of the WGP extinction ratio and insertion losses for pitch fill factor F=70% as a function of the pitch on a 100 µm thick foil for normal incidence.

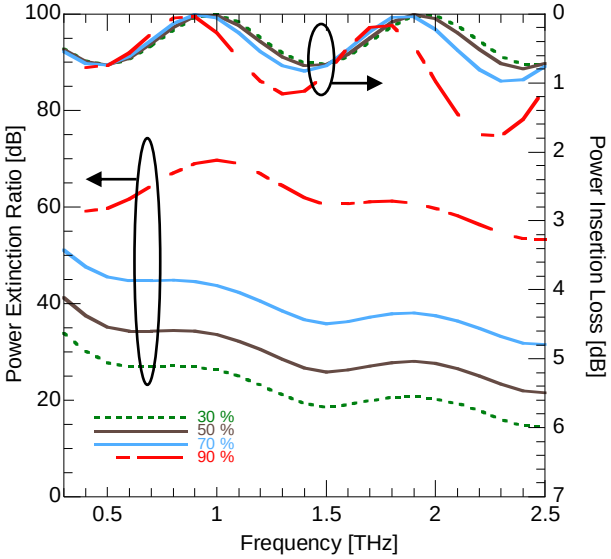

Figure 18: Numerical investigation of the WGP extinction ratio and insertion losses for pitch p=10 µm on a 100 µm thick foil as a function of fill factor for normal incidence.

Herein, we fixed the Zeonor® thickness equal to 100 µm, as physical foils were available. The first parameter that has been taken into account is the pitch of the grating structure, therefore we fixed the fill factor to 70% and varied the pitch to 10, 20 and 50 µm; the calculated power ER and IL are

illustrated in Figure 17. The polarizer with 10 μm pitch shows the highest ER, with an extremely high value of 50 dB at 0.3 THz and a minimum of 32 dB at 2.5 THz. As expected, the ER for *p*=20 μm decreases roughly by 6-7 dB while for *p*=50 μm the situation gets worse, with an observed reduction of the ER in excess of 15 dB. Regarding the IL, the Zeonor® film thickness influences this property causing Fabry-Perót (FP) effect, further details are reported later. In fact, for *p*=10 μm the IL are principally due to this effect remaining below 1 dB in the whole frequency range under investigation. At around 1 THz and 2 THz, the impedance matching condition enables a total transmission of the incoming polarization component. The 20 μm period case shows a similar trend with a slightly higher IL, owing to increased reflection of $E_{\perp}$ due to the metal. For p=50 μm, larger IL values are found, with a maximum of 4 dB. To sum up, the best performances were reached with a period of 10 μm, which represents in this case the smallest one under study.

Once we found the period, we studied the effect of the fill factor. Figure 18 reports the numerical investigation of the ER and IL of the proposed WGP where the pitch has been fixed to 10 μm and F varies from 30% to 90 %. Regarding the ER, its value increases by increasing the fill factor, as expected, because the increasing metal percentage reflects a greater amount of the unwanted polarization component (E_x). At 1 THz, ER is equal to 30 dB for F=30%, while it becomes 70 dB for F=90% representing the maximum value. However, the IL are negatively affected by a large F as more extended metallic parts in the structure also increase reflection losses for $T_{\perp}$. In fact, we can observe in Figure 18 that for F=90% the losses are between 1 and 2 dB outside the impedance matching condition frequencies.

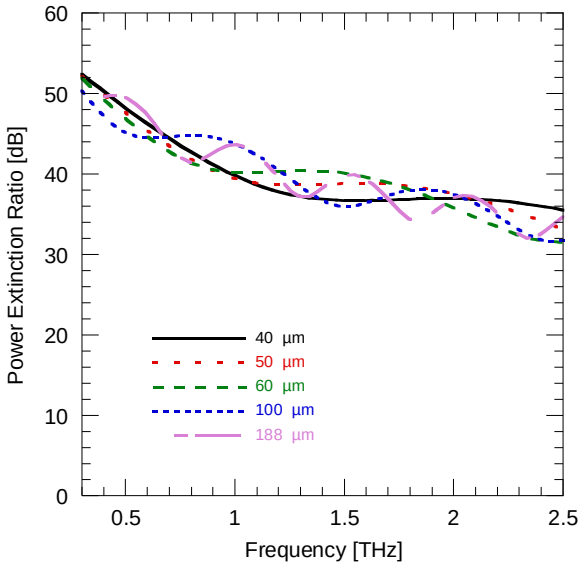

Figure 19: Numerical investigation of the WGP extinction ratio for pitch p=10 μm, F= 70% as a function of Zeonor®® film thickness for normal incidence.

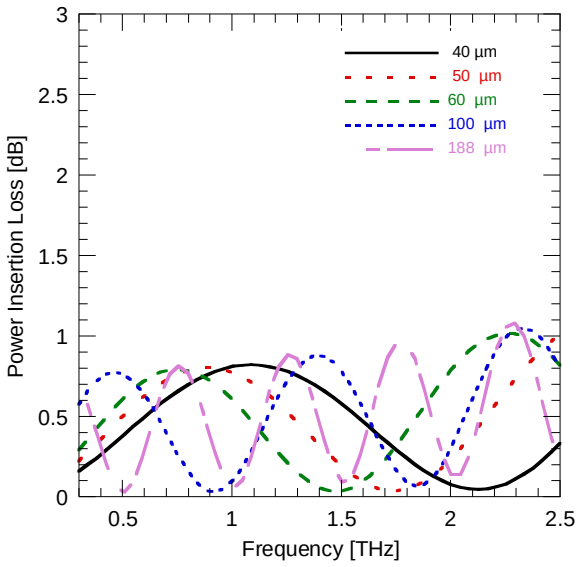

Figure 20: Numerical investigation of the WGP insertion losses for pitch p=10 µm, F= 70% as a function of Zeonor® ® film thickness for normal incidence.

Since the Zeonor® thickness influences the frequency at which the impedance condition occurs, we performed a detailed numerical analysis by varying the Zeonor® thickness and fixing the period and the fill factor. We chose the thickness values that are commercially available from Zeon Co., namely 40, 50, 60, 100 and 188 µm [31]. Figure 19 and Figure 20 report the numerical results of the extinction ratio and insertion losses, respectively, for a polarizer having pitch p=10 µm, F= 70% as a function of the Zeonor® film thickness at normal incidence. As already mentioned, the Fabry-Perot effect depends on the substrate thickness, the oscillating period of the ER and IL increases as the thickness gets higher, as observed in both Figure 19 and Figure 20. This phenomenon is of fundamental importance especially for the insertion losses since it is possible to tune the frequency at which IL=0 by only varying the substrate thickness.

In conclusion, we found a satisfactory trade-off between high extinction ratio, low loss and low fabrication cost with the following geometrical parameters: Zeonor® thickness = 100 µm, grating pitch p=10 µm, F=70% and Aluminium thickness= 200nm. However, in order to facilitate the fabrication on the 40- µm thick Zeonor®, we doubled the period keeping the same fill factor resulting in a slightly reduction of the performances.

2.3 Fabrication process

Now, we briefly introduce the photolithography procedures involved during the fabrication of our devices in clean room. Figure 16 describes the fabrication flow in which the fundamental elements

are a light source, a photomask (master) a photosensitive material (photoresist) and a developing solution.

The first step requires a foil of Zeonor® film, 1 inch size, cut with scissors and cleaned with acetone and isopropanol (IPA) in an ultrasonic tub. Then the slab is put under high vacuum and a layer of metal is thermally evaporated on it The skin depth (δ) in aluminium is 150 nm at 0.3 THz and 52 nm at 2.5 THz. Hence, we set its thickness at 200 nm thick. Later on, a positive photoresist (S1813 from Shipley) was spin-coated at 3000 rpm for 30 seconds and then backed at 115°C for 2 minutes, resulting in a uniform layer having a final thickness of 1.3±0.1 μm. The photoresist top surface is exposed to the UV light pattern (λ=365 nm and I=60 mW/cm^2) produced by a using a Karl Suss MA150 mask aligner exploiting a photomask with the desired geometry. Through the photomask, only specific areas of the resist layer are illuminated with UV light. In case of a positive photoresist, UV light induces a change in the properties of the material which becomes soluble for a suitable developing solution. On this way, after the exposure, the sample is immersed in the developer MF319 for 50 seconds, rinsed with deionized water (DI H_2O) and dried with nitrogen. Afterwards, a hard bake of the sample at 120°C for 5 minutes increases the photoresist resistance to wet chemical etching solution. Once the desired pattern is transferred on the sample surface, the exposed aluminium (area not protected by the resist) is wet-etched in a solution of H_3PO_4:H_2O:CH_3COOH:HNO_3=16:2:1:1. Finally, the sample is clean with acetone and IPA and dried with nitrogen flow in order to remove the residual photoresist.

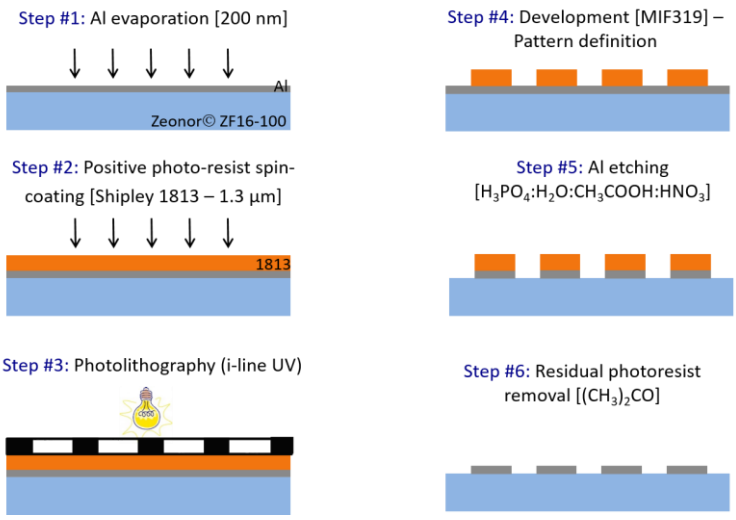

Figure 21: Fabrication processes steps.

2.4 Experimental results

After the design optimization process, a polarizer with a pitch of 10 μm and fill factor of 68% was fabricated on low loss flexible and conformal 100 μm-thick Zeonor® foils sized 2.54 cm x 2.54 cm (1 inch x 1 inch), using the technique described above. However, all fabrication steps are easily scalable to larger area as well as to a roll-to-roll process. Figure 22 illustrates the fabricated polarizer mounted on a 3D printed curved mount positioned on a manual rotation stage. The insert shows a micrograph of the fabricated WGP taken under optical microscope in transmission mode with a diffraction limited 100x /90 microscope objective, where the black parts are the Al stripes, while the transparent Zeonor® foil appears white. The width is 6.8 μm while the pitch of the structure is 10.0 μm. The deviation of 0.2 μm from the nominal value is within λ/2 of the g-line used to impress the photoresist as expected. Its electromagnetic properties were investigated by means of THz time domain spectroscopy using a Menlo Systems TERA K15 all fiber-coupled spectrometer in transmission mode. The measurements were done in an atmosphere purged with nitrogen (N_2) in order to prevent water absorption of THz radiation. As shown in Figure 18, the ER is expected to reach 70 dB for F=90%. However, the frequency dependant dynamic range of the available TDS Menlo K15, limits the ER that can be reliably measured to the case of F=70% and pitch of 10 μm.

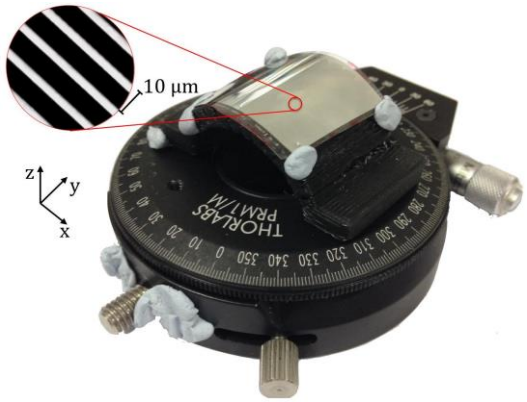

Figure 22: Flexible THz polarizer on a curved mount, placed on a rotation stage for the THz-TDS experimental setup. The insert shows a micrograph of the fabricated WGP (p=10 μm and w=6.8 μm) in X configuration under optical microscope in transmission mode. The black parts are the Al stripes, while the transparent foil appear white.

The emitted THz wave has a diameter of 25 mm, it is collimated and partially polarised with horizontal polarization. Ideally, the accurate measurement of the polarization properties would require a calibration standard with known polarizing properties and preferably, infinite extinction ratio and nil insertion loss. Unfortunately, these conditions are not fulfilled at THz, moreover the emitting and detecting antennas are polarized to some extent, but the manufacturer does not declare their properties. Hence, we have used two identical polarizers in order to perform a self-referenced

measurement. The measurement procedure is quite complicated and requires some care since the source and the detector are partially polarized. The first polarizer has been set with its easy axis, namely, the axis that defines the component of the THz wave that is easily transmitted, at 45° with respect to the polarization of the main component of the THz emitted beam. The second polarizer has been set perpendicular to the first one and $T_{\parallel}$ is measured. Then, the second WGP has been rotated by 90°, until the maximum detected signal is observed, and $T_{\perp}$ is recorded. In order to measure the IL, we have referenced the transmitted radiation when both the first and the second WGP are into the maximum transmission, i.e., with the metal wires perpendicular to the emitted polarization, and thus parallel to each other. Subsequently, the second WGP was removed and the ILs were calculated as the ratio between the maximum detected power in the presence of the second WGP and the one measured without it [139], [143].

Since the fabricated WGP has a fill factor of 68%, we have performed a new numerical analysis for a better comparison between numerical and experimental results. The performance of the polarizer was first investigated in a flat configuration. Then, given that the WGP is fabricated on a flexible and conformal substrate, we have performed the measurement also in two different bending configurations using a custom made 3D printed curved mount with a radius of curvature R=12.5 mm.

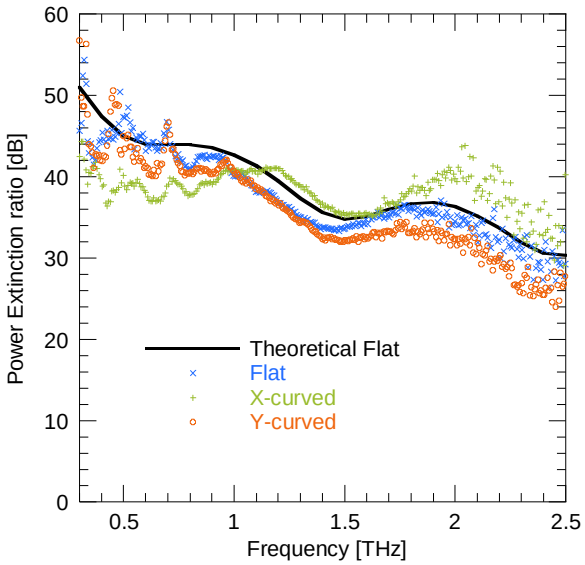

Figure 23: Comparison of experimental measurements and numerical results of the extinction ratio for the THz WGP with p=10 μm and F= 68% for normal incidence. The scattering of data at higher frequencies is due to the decreasing signal-to-noise ratio of the instrument.

We define the configuration with the bend along the Al stripes as X-curved, while the one curved perpendicular to the stripes as Y-curved. Figure 23 reports the comparison between theoretical flat configuration (black line), experimental flat (light-blue line), X-curved (green line), and Y-curved

(orange line) configuration of the power extinction ratio (ER), see Figure 22 for the axes. The ER for the flat case agrees very well with the simulation results showing an ER larger above than 30 dB for the entire range and between 35 dB and 45 dB for 0.3 – 1.5 THz. The results in curved configuration, even if the WGP is significantly distorted, are similar to the flat case showing an ER above the target value of 30 dB and values up to 50 dB at the low-frequency edge of the spectrum under study. These results confirm the extraordinary performance in terms of ER for the proposed polarizer in all the cases under study. Those values are equivalent to the state of the art polymer polarizers in the visible range. Moreover, Figure 24 reports the same comparison between theory and experimental measurements for both the flat and curved configurations in terms of insertion losses (IL). As in the case of the extinction ratio, the insertion losses for the flat and Y-curved cases agree very well with simulation, with a value below 1 dB for the entire range in consideration. In both cases, the losses are almost exclusively due to Fabry-Perót effect in the polymer, with almost no losses at approximately 1 THz and 2 THz. Instead, in the X-curve case the insertion losses are slightly affected, which is attributed to the change of the effective angle of incidence across the surface of the polarizer owing to the curvature.

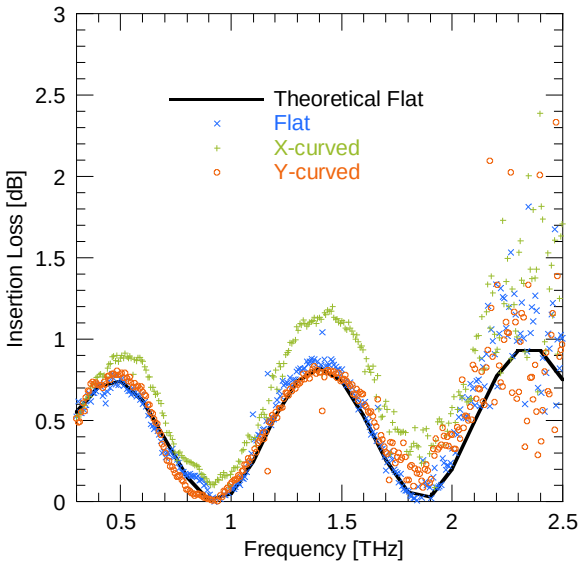

Figure 24: Comparison of experimental measurements and numerical results of the insertion losses for the THz WGP with p=10 μm and F= 68% for normal incidence. The scattering of data at higher frequencies is due to the decreasing signal-to-noise ratio of the instrument.

Successively, a WGP with a pitch 20 μm and fill factor of 70% (w =14 μm) was fabricated on 40 μm-thick Zeonor® foils, illustrated in Figure 25. The latter shows the WGP fixed on a standard 1" rotation mount while the inset reports a micrograph taken under optical microscope in transmission

mode with a diffraction limited 100x /90 microscope objective, where the black parts are the Al stripes, while the transparent parts are Zeonor®, as in Figure 22.

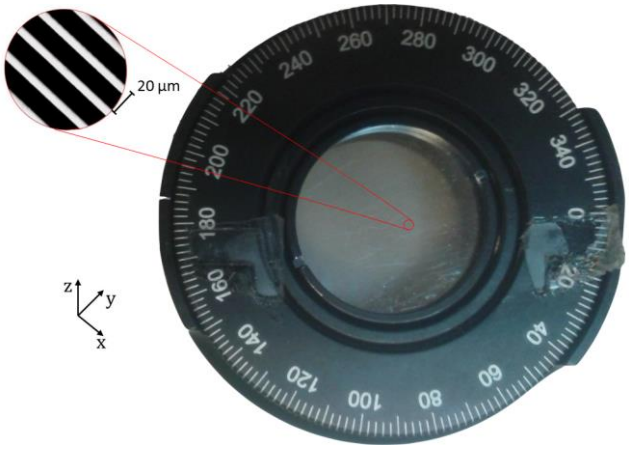

Figure 25: Terahertz polarizer on a standard 1-inch mount. The inset reports a micrograph taken under the microscope in transmission mode of a fabricated sample with p = 20 µm, w = 14 µm on a Zeonor® foil with d = 40 µm.

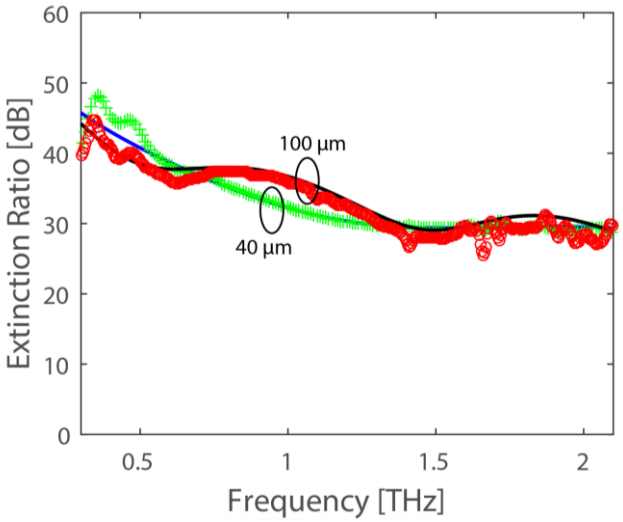

Figure 26: Comparison of experimental measurements (markers) and numerical (solid lines) results of the extinction ratio for THz WGPs with p=20 µm and F= 70% on Zeonor® foil 40 and 100 µm thick.

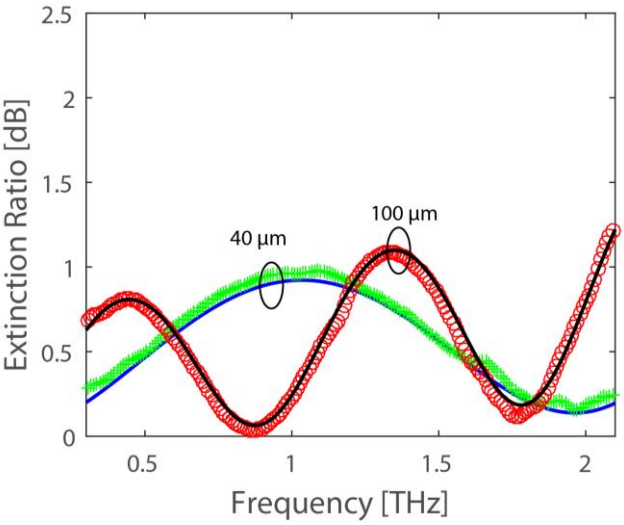

Figure 27: Comparison of experimental measurements (markers) and numerical (solid lines) results of the insertion loss for THz WGPs with p=20 µm and F= 70% on Zeonor® foil 40 and 100 µm thick.

In order to clearly demonstrate the effect of the substrate thickness on the performances of the polarizer, another WGP with the same geometrical features was fabricated on Zeonor® having thickness of 100 μm. Figure 26 shows the comparison of numerical (solid lines) and experimental (markers) results of the power ER for the proposed WGPs on 40 and 100- μm thick Zeonor® substrates having p=20 μm and F= 70%. For both WGPs, the experimental measurement are in very good accordance with the simulations ones exhibiting an ER of 45 dB at 0.3 THz which decreases as the frequency increases until the value of 30 dB at 2.1 THz. It is remarked that the slope of the ER depends on the polymer thickness, in particular for the WGP fabricated on 40 μm Zeonor® the slope is more regular respect to the 100 μm one due to the Fabry-Pérot effects. The influence of the polymer substrate on the polarizer performance is more evident in Figure 27, which reports the IL for both samples. In both cases the IL is as low as 0 dB at the matching frequency and never exceeds 1.1 dB. It is remarked that, owing to matching condition, the WGP on 40 μm thick Zeonor® shows an IL of 0.18 dB at around 2 THz which is important for use in combination with THz QCL sources because back-reflections are to be avoided [23]. Moreover, this feature is not easy to obtain because most common polymers used at THz exhibit a great attenuation a 2 THz. Regarding the sample on 100 μm Zeonor®, the IL approaches 0 dB at 0.9 and 1.7 THz, confirming the trend observed for the other class of WGP that has p=10 μm.

It is worth nothing that the matching frequency of the two devices does not simply scale with the thickness of the polymer foil. We here stress that the matching frequency is shifted to lower frequency for a larger fill factor and for a larger pitch.

2.5 Conclusion

To sum up, a low-cost Al THz WGPs were fabricated on flexible and conformal low-loss dielectric foils of Zeonor® having thickness of 40 and 100 μm. The geometrical parameters were optimized for the 100 μm case by a detailed study using the finite-element method (FEM). The final design of the proposed polarizer has a pitch of 10 μm and fill factor of 68%. Its performance in bending configurations shows little difference with respect to the properties of the flat sample, namely an extremely high ER with max of 45 dB in the 0.3-1 THz range and of 30 dB up to 2.5. Furthermore, it shows an IL less than 1 dB for the entire frequency range, and at targeted frequency the IL is almost zero. Regarding the WGP on a 40 μm thick substrate, even if we doubled the pitch for facilitating its fabrication, it is only slightly less performant respect to the optimized one showing similar value of ER and IL. Thanks to its IL behaviour it can be used with quantum cascade lasers operating at higher frequency. For all the fabricated samples, the experimental results are in excellent agreement with the

theoretical study. The outstanding properties of the polarizer pave the way for a new class of flexible and conformal THz devices. Moreover, the proposed polarizer can be fabricated with low-cost techniques used for large-area electronics such as roll-to-roll or gravure printing.

Chapter 3:

Frequency Selective Surface filtering components

3.1 Introduction

In chapter 1 we introduced THz sources and detectors and classified them in two main categories: narrowband and broadband. Hence, there is a need to manipulate the THz wave is a strategic issue and novel THz components are of paramount importance. In this context, THz transmissive filtering elements allowing for the bandpass transmission around a specific frequency are well needed, especially in such applications as telecommunications, radar science, imaging where a precise range of frequency is necessary [144]–[148]. A traditional solution for bandpass filters in the THz frequency range is based on resonant frequency selective surfaces (FSS), already known since 1983 [149], where a polarization-independent square periodic arrays of cross-shaped apertures were patterned on a free-standing nickel foil. At the time, as we discussed, this part of the electromagnetic spectrum was

referred to as far-infrared. Later, Porterfield et al. [150] applied the same geometry using copper; these two seminal works established the main design rules and explain how the performances of the filters depends on their geometry. Since this design is based on a square periodic array of cross-shaped apertures, this configuration of filter is polarization insensitive thanks to the C-4 symmetry. Later on, several works have been performed in order to transfer this geometry on dielectric substrates, as for example patterning FSS on polyimide film [151], [152], on thick polyethylene substrate [153], or on costly 525-μm high-resistivity silicon substrates, which present very good out-of-band rejection, although still accompanied by moderate peak transmittance [154]. Other substrate solutions include the use of 100 μm polyethelene terephthalate or naphthalate, which were employed in a different context, namely the design and fabrication of multi-layer stacks of split-ring resonator FSS and metamaterials in the THz spectrum [155]–[158].

The idea behind my work was to fabricate cross-shaped FSS aperture filters on Zeonor® substrates as already done for the polarizer (chapter 2). The fabricated filters show a very interesting response demonstrating that, when the cross-shaped FSS design is patterned on a thin low loss polymer substrate, two contemporary effects exist: the broadband filtering peak and a series of Fano-like asymmetric narrow band peaks. The former is the typical response of the FSS, while the latter ones are a secondary effect that arises from guided-mode resonances (GMR) in the polymer substrate. The observed guided-mode resonances (GMR) occur at resonant frequencies where the first order diffracted waves are phased-matched and thus coupled to modes guided in the dielectric substrate [159]–[164]. We carried out a detailed numerical investigation of the proposed filters varying their geometrical parameters or the substrate thickness. Then the fabricated filters were characterized by means of THz-TDS showing very good agreement with the numerical results. One of the filters was bent on a curved mount, as done for the polarizer, revealing two distinct behaviours, the robustness of the fundamental FSS filter response and the suppression of the GMR peaks [165]. Successively a set of measurements at different incident (θ) and polarization (φ) angles revealed that, when the incident wave is not at normal incident ($\theta \neq 0°$) and/or its polarization (φ) angle is not zero, the C-4 symmetry behaviour is broken, as expected. In those cases, the main peak remains almost unaffected while the GMR secondary peaks shift toward lower frequency and some of them are suppressed [165], [166].

3.2 Design

Figure 28 depicts the schematic diagram of the THz-FSS filters, argument of this chapter, indicating their fundamental geometrical parameters that are the pitch (P), the length (W) and the width (w) of

the cross-shaped apertures and the Zeonor® thin film thickness (d). The latter is normally considered an independent variable. However, we will show how it plays a significant role in the filters performance.

As for the polarizer proposed in chapter 2, the Al film thickness is 200 nm, thicker than the Al skin depth in the investigated frequencies range, at the same time, it is thin enough in order to avoid unnecessary stressing of the polymer during the fabrication process. Furthermore, Figure 28 reports the incident (θ) and polarization (φ) angle of the incoming THz wave.

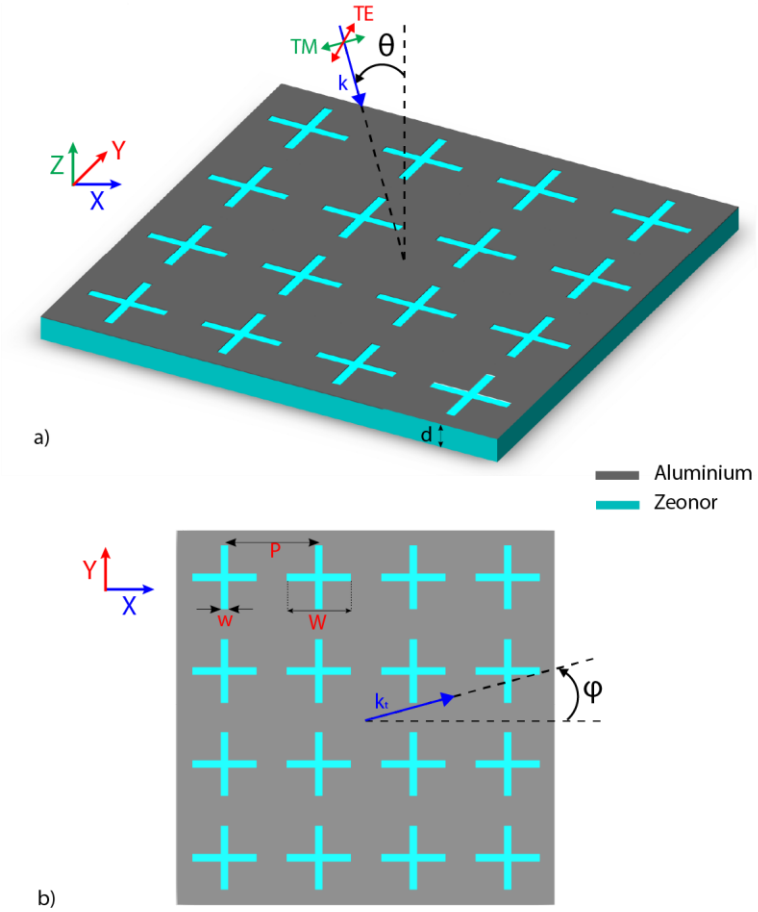

Figure 28: Schematic diagram of the proposed FSS filter, a) 3D and b) 2D where d is the Zeonor® thickness, ϑ and φ the incident and polarization angle respectively, P the lattice period, W and w the length and width of the cross-shaped apertures. The thickness of the Al layer is 200 nm.

Here too, the numerical investigation of the proposed filters was performed by means of the finite-element method (FEM), implemented in the commercial solver COMSOL Multiphysics©. A unit cell of the periodic array was simulated by properly imposing periodic boundary conditions at the x-z and y-z planes. The structure was excited with an x-polarized plane wave propagating along the z-axis as in Figure 28. The transmittance of the zero-order diffracted mode was measured at the output port of the filter, below the polymer film substrate, and normalized to the power carried by the excitation

plane wave. Aluminium was modelled as a Drude medium and the Zeonor® as a moderate lossy dielectric. Details are provided in 2.

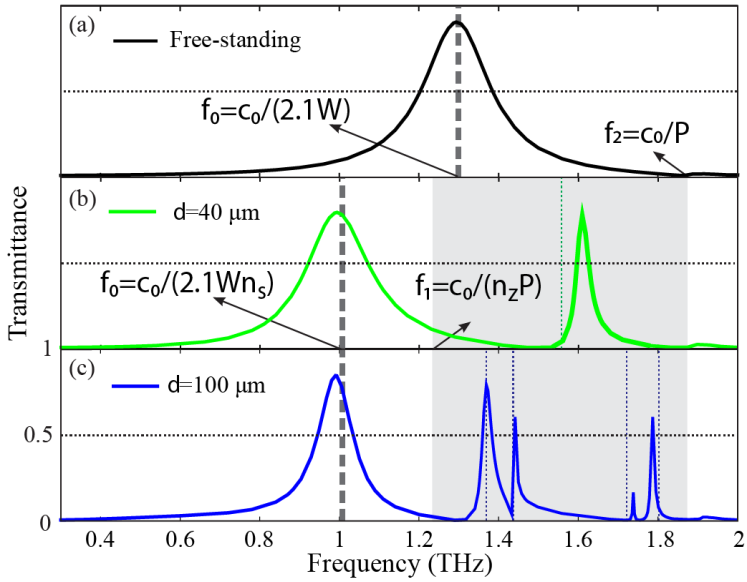

Figure 29: (a) Power transmittance of the zero-order diffracted mode, calculated for a free-standing FSS filter with P = 160 μm, W = 110 μm, and w = 10 μm. The dashed line corresponds to the frequency f_0 predicted by the approximative formula for resonant dipoles, whereas f_2 denotes the onset of diffraction, associated with Wood's anomaly that leads to zero transmittance. (b,c) Transmittance of the filter for a substrate thickness d = 40 μm and d = 100 μm, respectively, where other parameters as in (a). The shaded region denotes the frequency interval where guided-mode resonance can manifest.

In order to completely understand how the polymer substrate could affect the response of the filters, we modelled a reference free-standing THz filter, i.e. in the absence of the polymer substrate, having P = 160 μm, W = 110 μm, and w = 10 μm and its transmittance is reported in Figure 29(a). A Lorentzian-shaped filter is observed with peak transmittance T = 0.88, resonant frequency f_0 = 1.293 THz, and a FWHM of 200 GHz, i.e. 15% of f_0. This response is due to the resonance of the fundamental mode in the cross arm slots, which is maximized at the frequency f_0, due to impedance matching [167].

When w/(P − W) < 1, the resonant frequency can be well approximated by the formula for resonant dipoles [149].

$$f_0 = c_0/(2.1W) \qquad (1)$$

represented as a dashed line in Figure 29 and thereafter.

In the following, we refer to this resonant frequency as an FSS resonance (FSSR), which only slightly depends on the pitch P, since it is not diffractive in nature. In the spectrum, the Wood's anomaly

associated with zero transmittance is observed at a frequency $f_2 = c_0/P$ that indicates the edge at which the first diffractive order appears, c_0 being the speed of light in free-space [151], [168].

Later on, we performed the same numerical study but in presence of the Zeonor® substrate having a thickness of 40 and 100 μm, illustrated in Figure 29(b) and (c), respectively. With respect to the free-standing one, we can easily observe two differences, namely the shift of the FSSR and the presence of other resonances. The FSSR is shifted towards lower frequencies by a factor

$$n_a = \sqrt{\frac{(n_{zr}^2 + 1)}{2}} \qquad (2)$$

where n_{zr} represents the real part of n_z (refractive index of Zeonor®), and n_a represents the index corresponding to the average permittivity of materials on the two sides of the FSS, namely air and Zeonor®. Equation (2) is valid for substrate thicker than one tenth of the THz wavelength [151], which is our case. In general, in presence of a substrate or superstrate the THz wave has a shorter wavelength in the dielectric medium, the cross dimensions become electromagnetically larger and the FSSR frequency decreases.

The number and position of other resonances observed in Figure 29(b) and (c) depend on the polymer thickness. These resonances stem from the coupling of waves diffracted on the periodic FSS metal layer to propagating modes in the substrate, a phenomenon known as grating mode resonance (GMR) where the polymer substrate acts as dielectric slab waveguide. This class of resonance has been studied in the field of optics and photonics since 1992 [159], [160] and recently GMR filter were designed to operate at THz frequencies [164].

The interval, identified in Figure 29(b) and (c) with grey shading, where at normal incidence the first-order resonances can occur is calculated using the GMR theory by means of Equation (3):

$$\frac{c_0}{n_{zr}P} \leq f_r \leq \frac{c_0}{P} \qquad (3)$$

at those resonant frequencies f_r that satisfy:

$$n_s = c_0/(f_r P) \qquad (4)$$

where n_s is the effective index of a mode guided in the substrate slab waveguide.

Inside these regions marked as dotted lines, a set of GMR frequencies were calculated using the following steps: first, the resonant frequencies f_r calculated by the FEM simulations are identified. These are represented by transmission maxima in the gray-shaded areas of the calculated spectra in Figure 29 (b) and (c). Then, for each slab thickness, the effective modal indices at f_r are calculated using a freely available electromagnetic mode solver for 1-D dielectric multilayer slab waveguides

[169]. Among the resulting modal indices $n_s(f_r)$, the frequencies $c_0/(n_sP)$ are calculated and the one closely matching f_r is marked, with each resonant frequency associated with a different slab mode. Better agreement is achieved for higher values of *d* and for modes closer to the limit $f_1 = c_0/(n_{zr}P)$. In both cases, these modes show higher confinement thanks to either the higher slab thickness or the higher effective modal index and hence lower modal order. The presence of the reflecting metallic FSS layer, that introduce a perturbation in the geometry of the slab waveguide, is responsible of the divergence between GMR theory and FEM simulations.

Figure 30 illustrates the calculated transmittance of a series of filters with fixed d = 100 μm, P = 160 μm, w = 10 μm, for various values of the cross-arm length W. In the figure, we observe that the GMRs do not depend on W whereas the FSSR are influenced by

$$f_0 = c_0/(2.1Wn_s) \qquad (5)$$

The final step of this detailed numerical study involves the variation of the pitch P for an FSS with fixed W = 110 μm, w = 10 μm, for the three available thicknesses of the Zeonor® film thickness. Figure 31 shows that the FSSR frequency (f_0) is only slightly affected, whereas the resonances of the GMR shift towards lower frequency for higher pitch values, as expected from Equation (2).

Furthermore, a larger number of guided modes in the slab waveguide are supported by increasing the polymer thickness. These are seen as a larger number of GMR peaks.

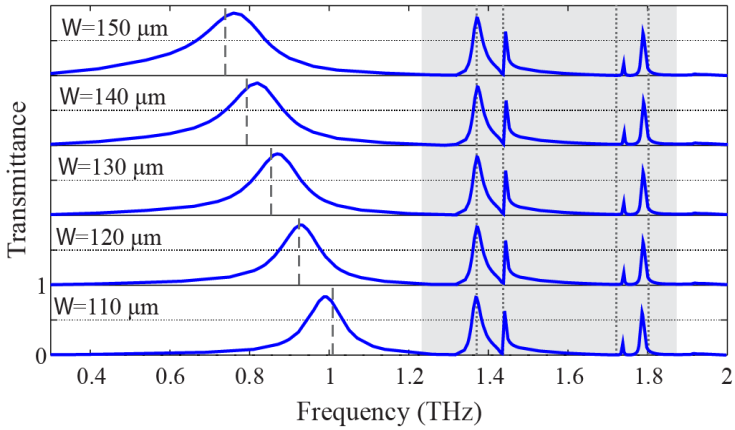

Figure 30: Transmittance of the FSS filter for d = 100 μm, P = 160 μm, w = 10 μm, for various values of the cross-arm length W. The main resonant frequency f_0 shifts towards lower frequencies for higher W, whereas the GMRs remain unaffected. The spectral position of the GMRs is well approximated by calculating the frequencies $f_i = c_0/(n_{eff,i}P)$, marked as dashed lines, where $n_{eff,i}$ are the effective indices of the modes supported by the single Zeonor® slab waveguide.

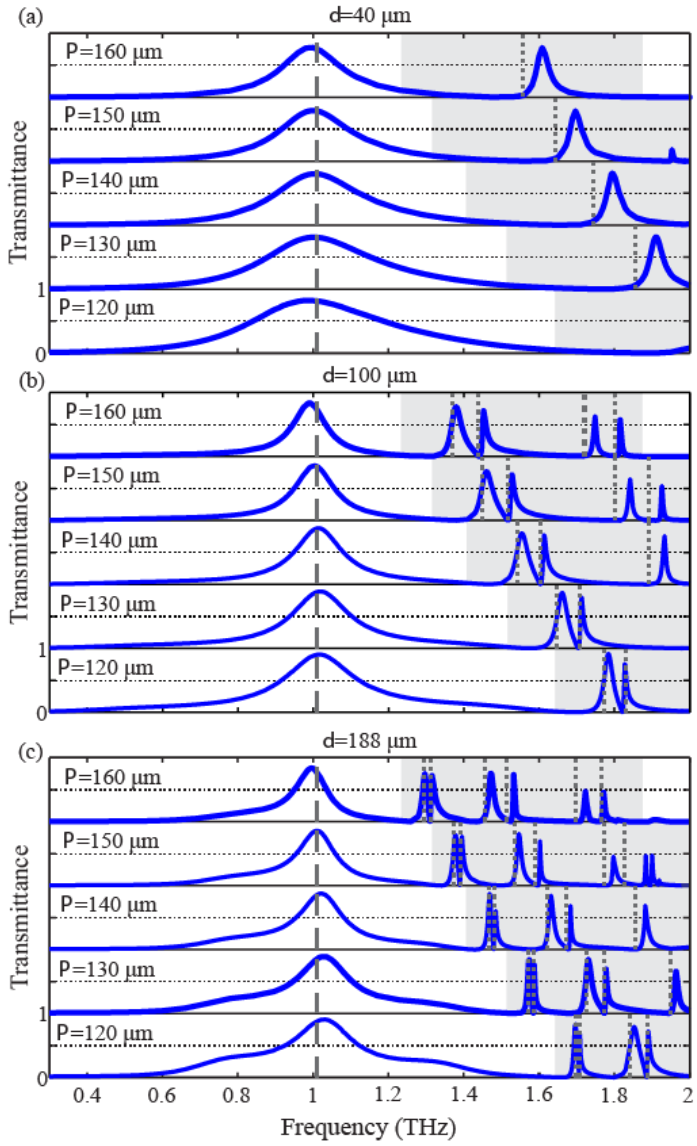

Figure 31: Transmittance of the FSS filter calculated for W = 110 µm, w = 10 µm, various values of the lattice pitch P and for three commercially available thicknesses of the Zeonor® substrate, namely (a) d = 40 µm, (b) d = 100 µm, and (c) d = 188 µm. The main resonant frequency f_0 remains fixed at $f_0 \simeq c_0/(2.1Pns)$, whereas the GMRs shift as a function of the lattice pitch and the substrate thickness.

To sum up the traditional FSS resonance exhibits a broadband response. As common in the art, by stacking multiple FSS filters narrow peaks results at the expense of a reduction of the transmittance. On the other hand, GMRs in a single device induce narrowband response peak and preserve high transmission.

3.3 Normal incidence experimental results

After the numerical study, a set of filters with different geometrical parameters was fabricated on Zeonor® films using the process described in chapter 2. The dimension of the proposed filters is 2 cm x 2 cm. Their performances were evaluated using the THz-TDS set-up available (see chapter 2

for details) in nitrogen atmosphere with a collimated spot of 10 mm and a time scan of 400 ps for a spectral resolution of 2.5 GHz. The power transmittance measured for each sample was normalized to that of the reference signal, i.e. in absence of the sample.

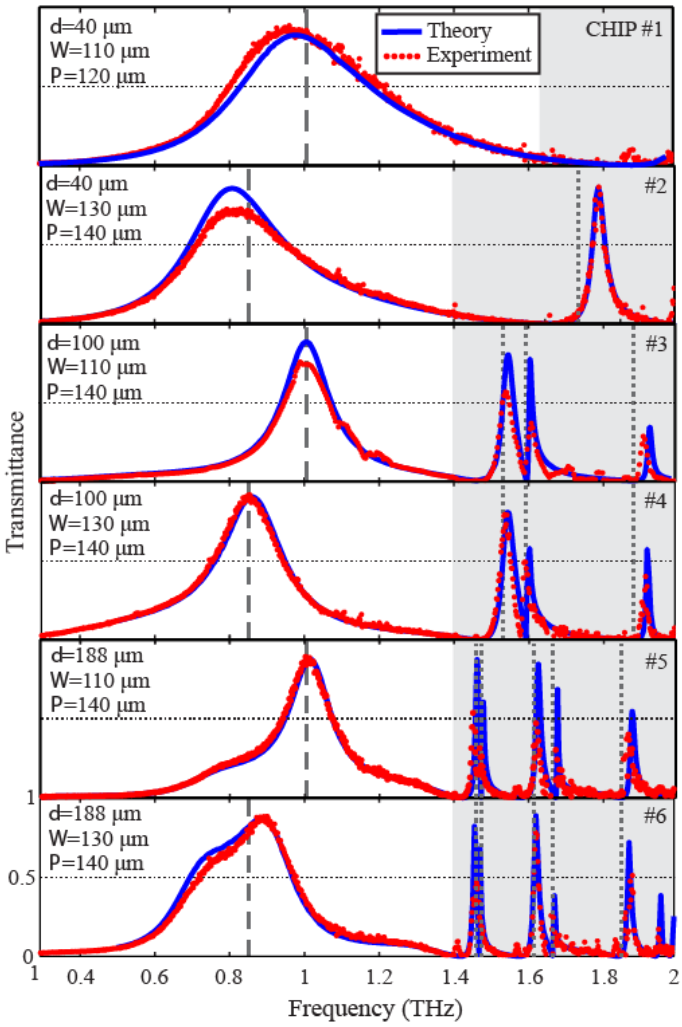

Figure 32: Comparison of the FSS filter's transmittance between numerical FEM simulations and experimental TDS measurements for a series of fabricated samples with different geometrical parameters.

The experimental THz-TDS data of six different filters (chips) agree very well with numerical data in terms of both the position and the lineshape of the various transmission peaks, as illustrated in Figure 32. Regarding d = 40 µm and P = 140 µm (chip #2), we observe two clearly separated resonances, the principal FSSR at 0.8 THz and a single GMR at 1.8 THz, showing very different linewidths: the FWHM measured for the FSSR is 40% of the resonant frequency whereas for the GMR is only 2.3%, more than one order of magnitude narrower. As already mentioned in the previous paragraph, when d = 100 µm and 188 µm, more modes in the slab waveguide exist and result in closely spaced GMR peaks. These peaks exhibit an asymmetric Fano-like linewidths, with high transmittance and even more narrow linewidths respect to d= 40 µm. In fact, a linewidth FWHM/f_0 less than 1% with high transmittance is obtained at 1.63 THz for d = 188 µm and W = 130 µm

(chip #6). In some GMR peaks, the experimentally measured transmittance values are slightly lower than the numerical simulation. This discrepancy is attributed to three factors: a) the very narrow linewidths of such resonances, particularly for d = 188 μm, which are comparable with the TDS resolution (2.5 GHz), b) minor defects in fabrication or the planarity of the samples as placed in the holder, and c) the finite dimensions of the sample and THz spot, in contrast to the infinite periodic array assumed in the simulations. The latter, in particular, is very relevant for GMR, since these are numerically calculated as the result of constructive interference between the excited waveguide modes and the diffractive waves on an infinite periodic FSS metallic layer, while the measurements are conducted over a finite structure. However, the fabricated FSS-THz filters show both broad- and narrow-band filtering, depending on the selection of the geometrical parameters.

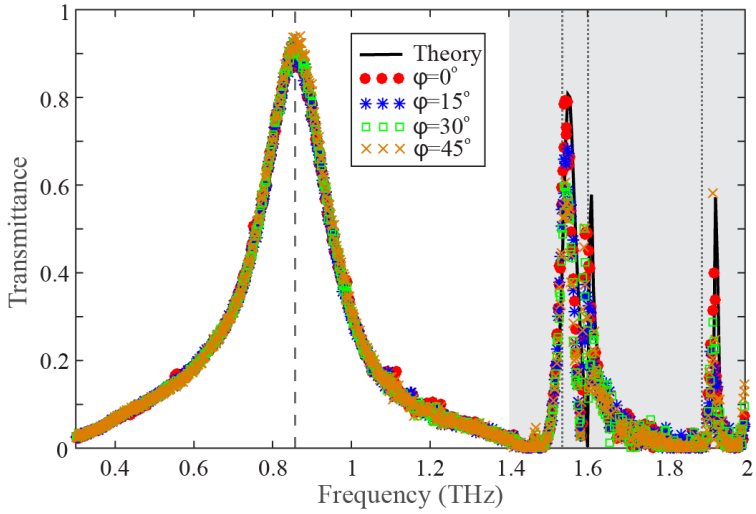

Figure 33: Experimental TDS measurements of Chip #4, as in Fig. 5, for different polarization angles (φ), demonstrating polarization-insensitive operation.

The proposed filters possess another interesting property that is their polarization-independent behaviour stemming from the C-4 symmetry of the FSS pattern. This property was experimentally proven by rotating the filter in the x-y plane, i.e. perpendicular to the propagation direction of the x- polarized THz wave, and recording the measured TDS spectra for the Chip #4 filter (with reference to Figure 32). Figure 33 reports the collected data at φ= 0°, 15°, 30° and 45° where the angle φ denotes the rotation angle of the sample, measured from the x-axis (Figure 28). There is no difference between the measurements confirming the polarization-independent response of the THz filter.

3.4 Bent configuration at normal incidence

One of the interesting properties of the employed thin polymer films is that they are flexible and can easily conform to curved surfaces as already demonstrated in chapter 2 [139]. Therefore, we have experimentally studied the transmission response at normal incident (θ=0°) of a filter characterized

by P = 140 μm, W = 110 μm, w = 10 μm, and d = 100 μm (chip #4), when bent down to a curvature with 1 cm radius. Figure 34 (b) reports a photograph of the bent filter fixed on a 3D printed mount while Figure 34(a) shows a micrograph of the fabricated filter taken under optical microscope in transmission mode with a 20x microscope objective, where the black parts are aluminium, while the transparent foil appears white. It is remarked that, after processing, the filter does not show any buckling and maintains its mechanical and electromagnetic properties after bending it several times.

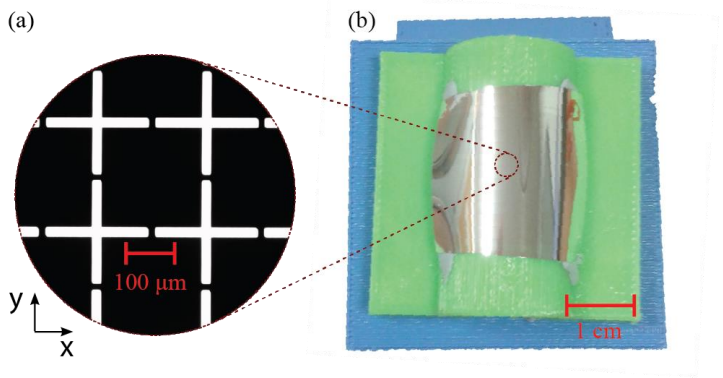

Figure 34: (a) Micrograph taken under the microscope in transmission mode of a fabricated sample with P = 140 μm, W = 130 μm, and w = 10 μm on a Zeonor® foil with d = 100 μm. (b) The same sample bent at a radius of 1 cm and fixed on a properly in-house fabricated holder.

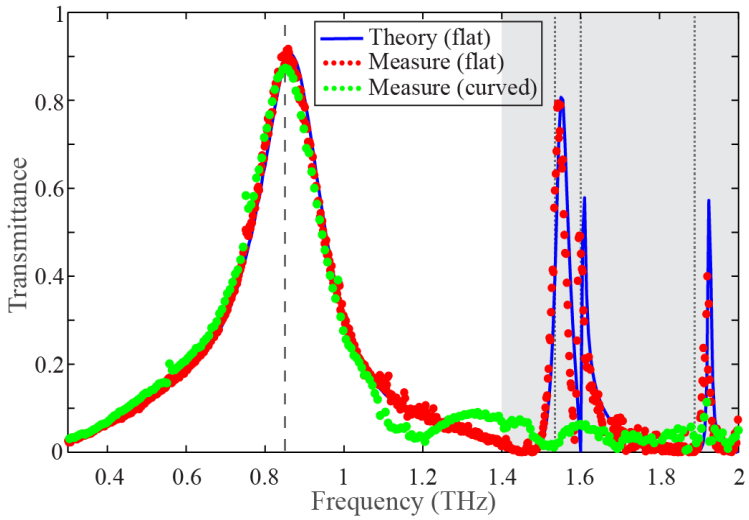

Figure 35: Comparison of the experimentally measured transmittance of the FSS filter shown in Fig. 7 between the flat and bent configuration. The numerical simulations for the flat case are also shown for reference. The main FSS resonance remains unaffected, demonstrating the capability of the fabricated samples to operate as flexible and conformal thin film THz filters. The GMR peaks in the bent configuration are suppressed.

During the measurements, the incoming THz wave was polarized along the x-axis, as defined in Figure 34(a). The collected data for the bent filter are illustrated in Figure 35 where the numerical and experimental results for the flat configuration are also reported for comparison. From Figure 35 it is clear that FSS resonance (FSSR) remains unaffected while the GMR peaks vanish. The reasons lie in the physical origin of the resonances. The FSSR involves the excitation of a localized mode

inside the cross-shaped aperture, which depends on the dimension of the aperture and is not diffractive in nature; therefore, it is independent on the lattice pitch, as already proven in Figure 31. On the other hand, the GMRs are excited due to the coupling of first-order diffracted waves into the substrate slab modes. This coupling is strongly influenced by both the lattice pitch and the thickness of the polymer films. When the sample is bent, the impinging THz plane wave does not see the same effective pitch across the surface of the filter and the substrate is no longer a flat slab dielectric waveguide leading to the suppression of GMR peaks, as shown in Figure 35.

Hence, the proposed THz filters show very interesting properties also when bent, which can be readily exploited in various applications. For example, flexible filters based on the FSSR can be designed for use as thin conformal layers on curved surfaces or components in THz setups. Moreover, the sensitivity of the GMR peaks and the FSSR on the bending radius can provide the basis for the development of sensor devices. For instance, curvature sensors or components for the measurement of the thickness and/or refractive index of thin dielectric layers at THz frequencies by placing the FSS-GMR filters on top of the sample and measuring the shift of the GMR frequencies.

3.5 Oblique incidence experimental results

In order to go further inside into the response of this category of filtering components, a new numerical study and experimental characterization was performed by varying the incident (θ) and polarization (φ) angles on the same FSS filter that has P = 140 μm, W = 110 μm, w = 10 μm, and d = 100 μm (chip #4). In this study, the incident (θ) and polarization (φ) angles have to be added in the Equations (1), (2), (3), (4), (5). The Zeonor® refractive index, as already stated in this dissertation, is to $n_p = n_{rz} - jn_{iz} = 1.52 - j0.0013$.

Now the wavevector of the TM-polarized incoming THz planewave is:

$$k = k_o \cos\theta\hat{z} + k_T = k_o(\sin\theta\cos\varphi\hat{x} + \sin\theta\cos\varphi\hat{y} + \cos\theta\hat{z}) \quad (6)$$

where $k_0 = 2\pi/\lambda$ represents the free-space wavenumber.

Thus, the GMR occurs at frequencies f_r given by [170]:

$$\left|(\sin\theta\cos\varphi - \frac{mc}{Pf_r})\hat{x} + (\sin\theta\sin\varphi - \frac{nc}{Pf_r})\hat{y}\right| = n_s \quad (7)$$

where *c* is the speed of light in vacuum, n_s is the effective index of the excited mode guided in the Zeonor® substrate, and the integers (m, n) denote the order of the THz wave diffracted by the periodic FSS.

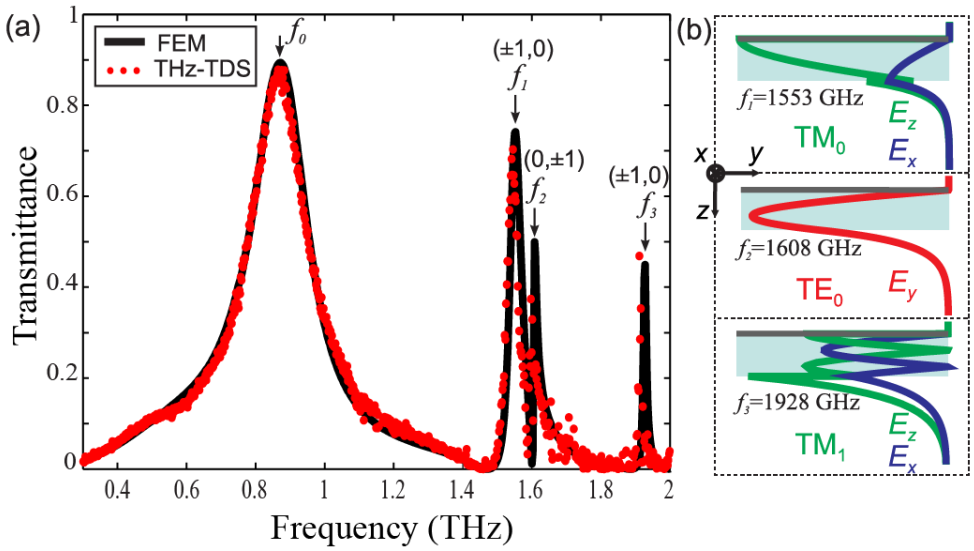

Figure 36: a) Transmittance of the FSS-THz filter under normal incidence. The frequencies f_i (i = 1, 2, 3) denote the spectral position of grating mode resonances. (b) Modal profiles of the TM0, TE0 and TM1 modes of an infinite waveguide of a 100- m thick Zeonor® film with a deposited 200-nm Al layer, calculated at the three GMR frequencies fi, respectively.

For an easier comprehension of this investigation, the transmittance at normal incidence was re-proposed in Figure 36 (a) where four different peaks are observed. The one at the lowest frequency (f_0 = 870 GHz) stems from the characteristic broadline response of THz-FSS filters, which can be approximated by the formula for resonant dipoles, Equation (5).The other three peaks at f_i (i = 1, 2, 3) are the result of the GMR, as already stated previously.

When θ = φ = 0°, Equation (7) reduces to

$$f_r = c\sqrt{m^2 + n^2}/(Pn_s) \qquad (8)$$

In the spectral window under investigation, one can observe either (±1, 0) or (0,±1) diffracted modes, that occur at frequencies f > c/(Pn_{rz}).

In order to recognise the origin of the three GMRs at f_i, the polarization of the impinging THz planewave is x-polarized. Therefore it can couple to both TM substrate modes propagating along the x-axis via the (±1, 0) diffracted waves or to the TE modes guided along the y-axis, excited by the (0,±1) diffracted waves. In a purely dielectric slab waveguide, the fundamental TE_0 mode has the higher modal effective index. However, in this filter, the dielectric slab is in direct contact with the Al layer that has a thickness higher than the skin depth in the investigated spectral region. This metallic layer causes high values of the z-component of the electric field in TM modes at the

Al-Zeonor® interface, thus increasing their effective index. This is demonstrated in the field profiles supported by the Al/Zeonor® hybrid slab waveguide shown in Figure 36 (b) that were calculated at the three resonant frequencies f_i. The fundamental mode for all frequencies of the hybrid slab is the TM_0, therefore, it is the TM_0 mode substrate that is coupled at the lowest GMR frequency f_1 = 1553 GHz. The TE_0 mode propagating along the y-axis follows next at f_2 = 1608 GHz and, last, the second-order TM_1 mode is excited at f_3 = 1928 GHz.

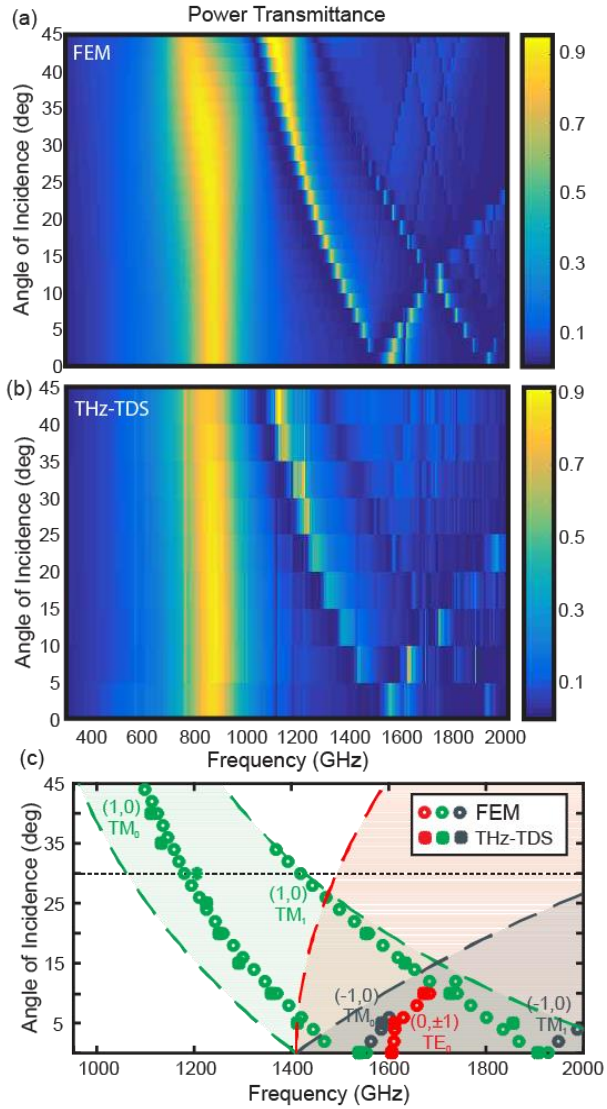

Figure 37: Transmittance of the THz-FSS filter (a) numerically calculated and (b) experimentally measured, for different angles of incidence ($\varphi = 0$). (c) Transmittance maxima for the three GMR: the resonances of the TM guided modes split into two branches for $\theta \neq 0$, which correspond to the (1, 0) and (−1, 0) diffraction orders, while the TE mode (0,±1) is degenerate. The shaded areas for each diffraction order are the spectral windows where GMR may manifest.

Figure 37 reports the numerical investigation and the experimental data when the polarization angle (φ) remains 0° and the angle of incidence (θ) varies from 0° to 45°, in steps of 2° and 5° for both numerical and TDS measurements and the experimental data agrees very well with the simulations. More in detail, in Figure 37 (a) and (b) we observe that the FSSR peak at f_0 shifts toward lower

frequencies only at incident angles higher than 25°. This behaviour leads to a successful operation of the filter also when the incoming wave impinges from various directions or, equivalently, when the filter is bent so that it conforms to a curved surface, as reported above. The analysis of the GMR peaks, instead, is more complicated since it involves the study of the propagating modes. Figure 37 (c) reports the maxima for the GMR peaks as a function of the angle of incidence (θ). The GMR frequencies at f_1 = 1553 GHz and f_3 = 1928 GHz for θ = 0° split into two different branches whose spectral distance increases with θ, while the one at f_2 = 1608 GHz is only slightly shifted until θ 10° and then diverges toward higher frequencies, described by Equation (7), when φ = 0°. For the (±1, 0) diffraction orders one obtains

$$\left|(sin\,\theta - \frac{mc}{Pf_r}\right| = n_{s,} \quad m = \pm 1 \tag{9}$$

implying that the GMR frequencies for the (±1, 0) orders are degenerate only when θ = 0°, namely at normal incidence. For other angles (θ ≠ 0°), instead, these frequencies split and lie within the two spectral windows marked as green (blue), for m = 1 (m = −1). Substituting the values of the refractive index of air and Zeonor® with n_s we retrieve the limit of these spectral windows. In addition, there is a good agreement between simulations and experimental measurements. The splitting behaviour is not present for the (0,±1) orders, which resonate at f_2 for normal incidence. Now, Equation (7) for φ = 0° gives

$$\frac{|n|c}{Pf_r} = \sqrt{n_s^2 - sin^2\theta} \quad m = 0 \tag{10}$$

Hence, the (0,±n) GMR frequencies are degenerate since they do not depend on the sign of the considered diffraction order. The spectral window where the (0,±1) mode can be excited is illustrated in Figure 37 as red-shaded region. Its boundary is delimited by:

$$\frac{c}{Pf_r} = (n_{rz}^2 - sin^2\theta)^{1/2} \tag{11}$$

In Equation (10), the term $\sin^2$ is negligible when θ has a small value, hence, the very small variation of the GMR frequency for the (0,±1) mode. It is also remarkable to observe in Figure 37 (c) the interference of the (0,±1) TE_0 mode with the (−1, 0) TM_0 and (1, 0) TM_1 modes. The latter arises when their resonant frequencies become closely spaced, namely at approximately 1610 and 1700 GHz, respectively. This interference leads to discontinuities in the shifting of the resonant frequencies and in the suppression of the (−1, 0) TM_0 mode at 1610 and of the (0,±1) TE_0 mode at 1700 GHz.

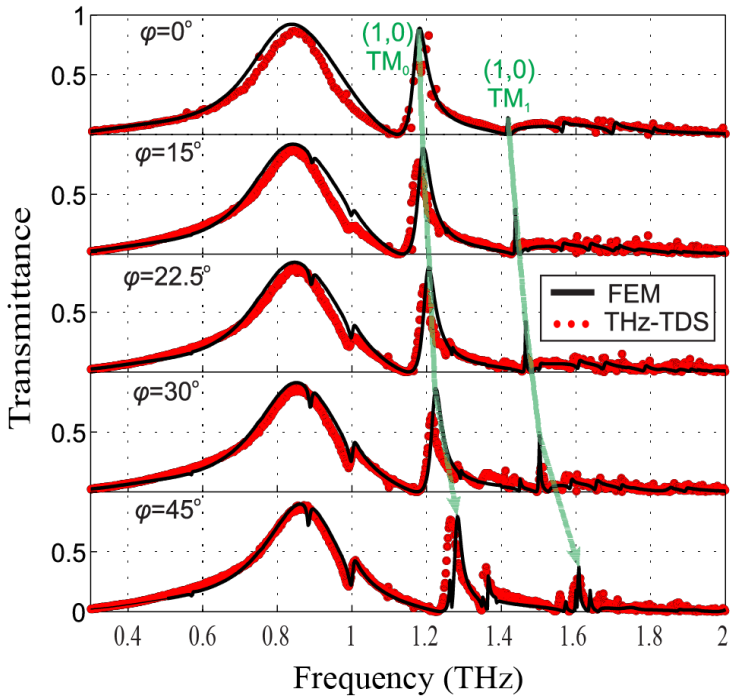

Figure 38: Comparison of the FSS filter's transmittance between numerical FEM simulations and experimental TDS measurements for incident angle $\theta = 30°$ at different values of polarization angle φ.

The final part of this chapter reports the filtering performance when the incident angle (θ) is fixed at 30° while the polarization angle varies (φ) from 0° to 45°, as shown in Figure 38. Two GMR peaks are present corresponding to the (1, 0) TM_0 and (1, 0) TM_1 modes, as illustrated by the horizontal dashed line in Figure 37 (c). For θ = 30°, m = 1, and n = 0 Equation (8) simplifies to

$$\frac{c}{Pf_r} = \frac{cos\,\varphi}{2} + \sqrt{n_s^2 - \left(\frac{sin\,\varphi}{2}\right)^2} \qquad (12)$$

The right end side of Equation (12) monotonically decreases in the interval $\varphi \in [0, 180°]$, thus leading to an increase in the resonant frequency f_r of the two (1, 0) modes. In Figure 38, which shows the simulation and experimental result for φ up to 45°, this phenomenon is clearly visible. Furthermore, the values of this frequency shift increase by increasing the polarization angle φ.

These results suggest that by fixing the angle of incidence, it is possible to tune the GMR frequencies by simply rotating in-plane the filter. To sum up, by varying the incident and polarization angle the filter performance can be adjusted in a wide spectral range.

3.6 Conclusion

A detailed numerical and experimental analysis of a novel types of THz filters, based on the patterning of metallic cross-shaped FSS on thin films of Zeonor®, was proposed and the influence of

geometrical parameters, incident and polarization angle was fully studied. Two different categories of peaks were recognized, the first stemming from the transmittance of THz waves through FSS cross-shaped apertures which leads to a broadband response and the second deriving from the excitation of guided-mode resonances in the polymer substrate that results in narrowband peaks. The latter are explained via grating theory. Furthermore, one of the proposed filters, thanks to the flexibility of the Zeonor®, was successfully characterized in bending configuration paving the way for conformal THz filters integrated on curved surfaces. In this case, the broad peak remains unaffected while the diffractive nature of GMR renders them sensitive to deformations or changes of the properties of the substrate. Finally, on the same sample, an exhaustive study of the impact of the incident and polarization angles of the impinging THz radiation was conducted. Also in this case the broadband resonance induced by the FSS remain unchanged while the narrowband GMRs, excited in the substrate, undergo a frequency shift. In addition, the guidelines for tuning the response of the proposed THz filter were reported. This new class of THz filters may provide narrowband filtering in future THz devices and systems for telecommunication or sensing.

Chapter 4:

Thin-film Guided-Mode Resonant bandpass filters

Part of the work herein reported is reprinted/adapted, with permission, from [A. Ferraro, D.C. Zografopoulos, R. Caputo, and R. Beccherelli: 'Squeezing narrow band terahertz radiation through extremely subwavelength slits in guided-mode resonant cyclo-olefin thin films', submitted, 2017]

4.1 Introduction

Chapter 3 reports a detailed analysis about the most common class of THz bandpass filters which are represented by frequency-selective surface (FSS) filter based on cross-shaped apertures [122], [150], [157], [171], [172]. The latter ones were fabricated on thin flexible foils of polymer Zeonor® [165], [166]. The presence of the substrate influenced the spectral response of those filters by introducing a secondary effect defined as guided mode resonance (GMR) [159]–[162], [173], [174]. That is responsible for Fano-like narrow transmitted peaks. Starting from this phenomenon, validated in the THz frequency range only recently [164], in this chapter we describes the design, fabrication and characterization of very narrow band THz bandpass filter [175] specifically designed to operate in the THz communication windows at 625-725 GHz and 780-910 GHz [81] . The latter ones are very broad, 100 GHz and 130 GHz, respectively. Thus, dedicated allocation of spectral channels may be necessary for different application or different operators. The investigation describes the overall design guidelines studying the effect on the performance of the proposed filters in terms of geometrical parameters, substrate thickness and angle of incidence. Several filters with different properties were fabricated by patterning aluminium layer on Zeonor® thin film by using standard UV photolithography. The fabricated filters exhibit most of the features that a high-quality filter ought to possess, namely:

i) high peak transmittance (low insertion losses),

ii) narrow linewidth (high 3-dB quality factor Q),

iii) high out-of-band rejection,

iv) possibility for polarization-independent or adjustable polarization-dependent operation,

v) low manufacturing cost,

vi) compact overall dimensions.

Furthermore, as for the previous devices reported in this dissertation, these new class of filtering elements can be easily fabricated by means of low-cost and large-area electronic fabrication processes paving the way for the development of the envisaged short range and indoor THz communication systems. Furthermore, they can be used in application such as ultrasensitive sensors [176], compact spectrometers [146], telecommunication [177], or radar science [147].

4.2 Design

Figure 39 shows the schematic diagram of the proposed THz bandpass filters with the relative geometrical parameters. In detail, Figure 39 (a) illustrates a periodic pattern of Al stripes (1D) whereas in Figure 39 (b) the pattern is composed of patches (2D). The dimensionality of the pattern represents an important parameter as is also shown in the insets of Figure 39, in fact the 1D design is polarization sensitive while the 2D is polarization insensitive owing to its C-4 symmetry. As we have already done for the devices reported in the previous chapters, we used thin foils of Zeonor® polymer as substrate.

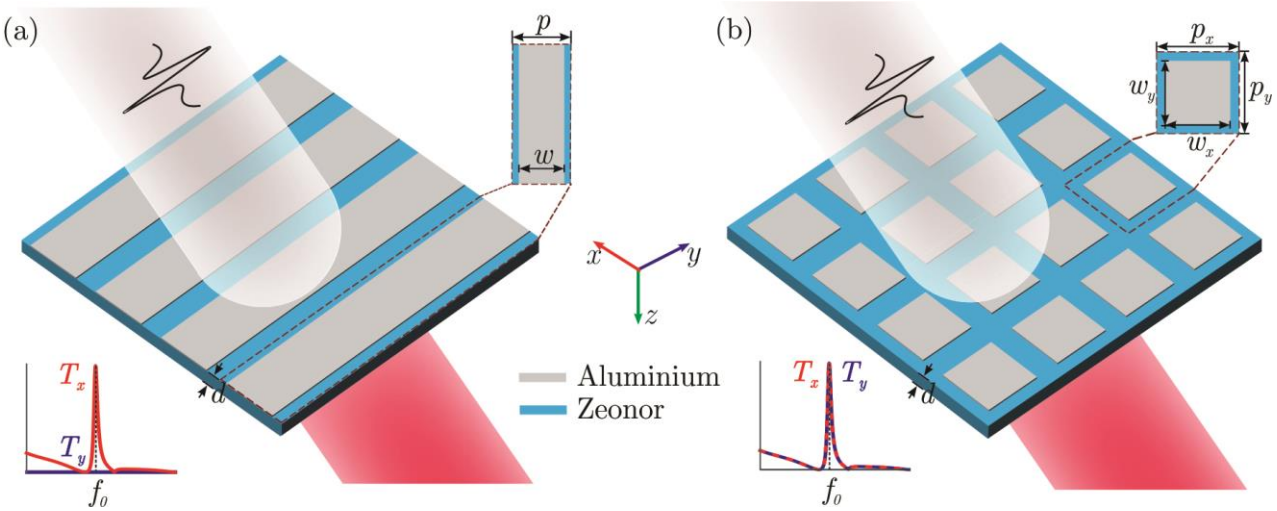

Figure 39: Schematic layout and definition of the geometrical parameters for the investigated GMR filtering elements based on a) 1D and b) 2D aluminum gratings patterned on cyclo-olefin Zeonor®. The thickness of the Al layer is 200 nm.

The operation principle behind these bandpass filters is represented by the GMR theory already reported in chapter 3. It is worth remaining that this theory states that THz radiation which is

diffracted by the Al periodic grating can be coupled to the polymer slab waveguide modes at resonant frequencies f_0 that satisfy Equation (13),

$$n_s = sin\,\theta + m\frac{c_0}{pf_0} \quad (13)$$

where n_s is the effective index of the guided mode at f_0, θ is the angle of incidence, p is the grating pitch, m is the diffraction order, and c_0 the speed of light in vacuum [164]. The guided mode effective index is constrained in the interval expressed by Equation (14)

$$1 \leq n_s \leq n_p \quad (14)$$

where n_z is the polymer refractive index.

Considering the case of normal incidence (θ=0°) and first diffraction order (m=±1), the interval where the resonances can occur is calculated by means of Equation (15)

$$c_0/n_z p \leq f_0 \leq c_0/p \quad (15)$$

The most used structure of GMR filters is based on all-dielectric gratings that operate in reflection, namely they block the transmittance at the GMR frequencies [159], [163], [178]–[180]. However, when the grating acts not only as the diffractive element, but also as a highly reflective screen, high transmittance is achieved only in a narrow band around f_0, even for a deeply subwavelength thickness of the filter [161], [162]. The proposed THz filtering elements design is based on this property.

The other important parameter that affects the performance of the filters is represented by the fill factor of the metal layer, defined as $F=w/p$, where w is the metal stripe/patch width. In particular, the fill factor influences mainly the peaks transmittance and the quality factor (Q), defined as the ratio between the resonant frequency (f_0) and the 3-dB linewidth (Δf). A secondary effect is the introduction of a frequency shift of f_0 toward lower frequencies, as shown later on in the chapter.

The numerical analysis, as for the previous chapters, was conducted via the frequency-domain finite-element method implemented in the commercial software Comsol Multiphysics©. In this case, the unit cell of the periodic structures was studied by applying Floquet periodic conditions at the lattice borders. The structure was excited by a plane-wave impinging from the top and the power transmittance of the 0^{th} order diffracted mode was calculated after transmission through the THz-GMR filter. The aluminium metal layer was modelled as a Drude medium and the Zeonor® as a dielectric, with refractive index of n_p=1.525-j0.0013, details are reported in the previous chapter.

4.3 Experimental results

Seven different chips were fabricated, whose geometrical parameters are reported in Table 1. First we have fabricated 1D filters with different period, successively 2D pattern filters with various period and thickness. Furthermore, Table 1 reports the comparison of the numerical and experimental operating frequency (f_0) and the quality factor (Q).

Table 1: Summary of the geometrical parameters and performance metrics of the fabricated GMR filters. Superscripts (N) and (E) stand for "numerical" and "experimental", respectively.

Chip	p_x [μm]	p_y [μm]	w_x [μm]	w_y [μm]	d [μm]	f_0^N [GHz]	f_0^E [GHz]	Q^N	Q^E
#1	390	-	351	-	100	668	667	29	29
#2	288	-	260	-	100	850	849	34	31
#3	288	288	260	260	100	850	851	3	32
#4	390	390	351	351	100	667	664	29	28
#5	340	340	306	306	100	745	748	30	30
#6	438	438	394	394	100	606	606	28	28
#7	288	288	260	260	40	985	984	62	73

For the 2D design, we have opted for square lattices ($p_x=p_y=p$, $w_x=w_y=w$) for inducing polarization-independent properties.

The period for chips #1-4 was chosen such that the resonant frequencies lie in the center of the low-loss atmospheric attenuation windows envisaged for next-generation THz wireless communications, i.e. 625-725 GHz and 780-910 GHz, where the attenuation is 10 dB per 100 m [81].

In order to perform a detailed parametric study on the influence of the period on the spectral response of this new type of THz filter, the other chips (#5-7) have different periods. However, all the fabricated filters have a fill factor of 0.9 which provides a good compromise between high peak transmittance, high quality factors, and high out-of-band rejection. The proposed filters were fabricated by means of UV photolithography (see chapter 2 for details). Successively they were characterized via THz-TDS (see chapter 3), using a spot-size of the collimated beam was ~10 mm in diameter and a terahertz time scan of 800 ps giving a spectral resolution of 1.25 GHz. All the experimental results agree very well with the numerical ones, as reported hereafter.

Figure 40 illustrates a comparison between the numerical results and the experimental measurements of the power transmittance in the spectral range of 0.3 -3 THz for chip #1 which has period of 390 μm and metal stripe width of 351 μm on a 100 μm thick Zeonor® substrate. As can be observed from the inset of Figure 40, the chip exhibits a single sharp peak with resonant frequency f_0 at 667 GHz, which lies in the first spectral telecom window, and a very high power transmittance equal to 86%. The transmitted peaks possess a 3-dB linewidth (Δf) of 23 GHz resulting in a good quality factor Q=29. A high-performance bandpass filter should also have a very low out-of-band transmittance that usually is quite difficult to achieve in a large spectral range. We opportunely engineered the parameters of the filter in order to obtain also this property. In fact, in Figure 40, it is clearly visible that the out-of-band transmittance of the chip stays below 10% in the complete spectral range between 0.5 and 3 THz. The THz-TDS data above 2.5 THz show some scattering owing to the decreasing signal-to-noise ratio of the instrument that affects the quality of the reference signal used for normalization. All the other fabricated chips (#2-7) possess this feature but in the remainder of this chapter the spectral window is zoomed to better visualize the transmitted peak.

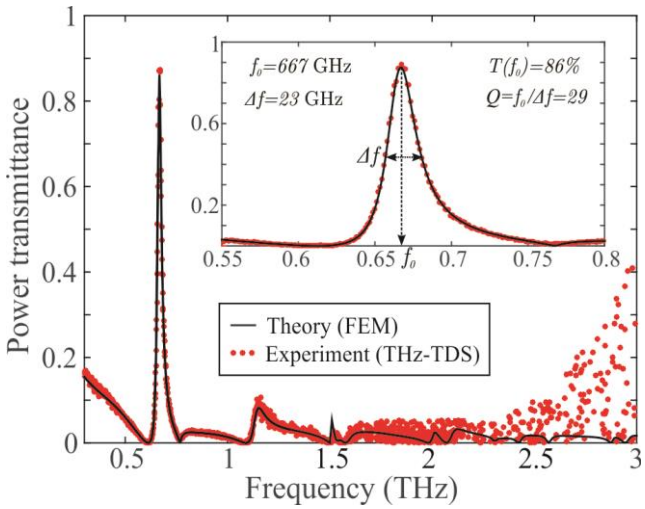

Figure 40: Numerically calculated and experimentally measured transmittance in the 0.3-3 THz range for a 1D GMR filter with p=390 μm, w=351 μm, and d=100 μm (chip #1) and relevant performance metrics. The inset shows a zoom around the resonant frequency of 667 GHz. The THz-TDS data above 2.5 THz show some scattering owing to the decreasing signal-to-noise ratio of the instrument.

We have numerically verified that the insertion losses of 14% (0.65 dB) at t\he resonant frequency stem from reflection (7%) and absorption in Zeonor® (5%) and in Al (2%), as observed in Figure 41. In fact, the latter reports the comparison of the numerically calculated transmittance for chip #1 in the range 0.55 – 0.8 THz assuming three cases: polymer and metal losses (Al/Zeonor®), no loss of polymer (nj=0) and no loss of metal (PEC) indicated as black, blue and red lines respectively.

Successively, for the same filter, we investigated the influence of the polymer imaginary refractive index (n_j) on the transmittance and hence on the quality factor, results reported in Figure 42. We considered four different values of the imaginary refractive index of the polymer, namely $n_j = 0$ (no

loss), n_j = 0.0013 (Zeonor® imaginary refractive index), n_j = 0.005 and n_j = 0.01. From Figure 42 shows, as expected, that the power transmittance decrease as nj increases leading in reduction of the Q-factor, which decreases from 29 to 24. It is remarked that, the transmittances of the Zeonor® polymer in the idealized case (n_j = 0) and in the reals case (n_j = 0.0013) overlap.

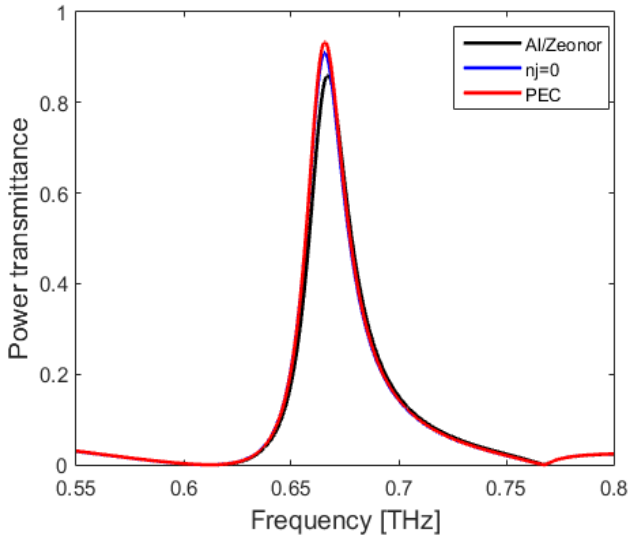

Figure 41: Numerically calculated transmittance in the 0.55-0.8 THz range for a 1D GMR filter with p=390 µm, w=351 µm, and d=100 µm (chip #1) varying the loss of metal and polymer.

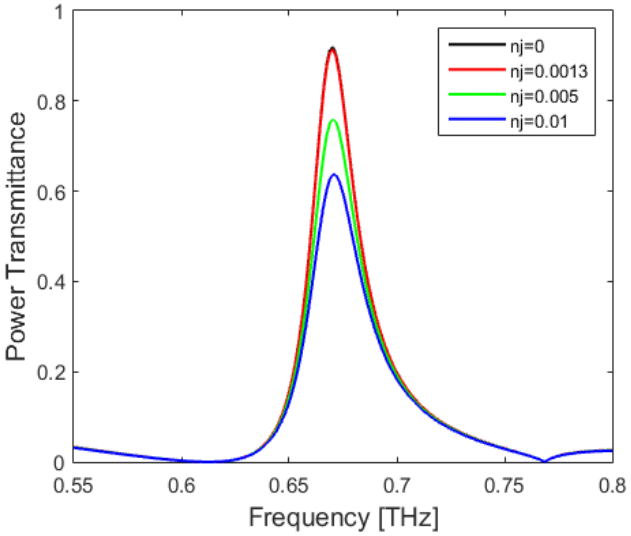

Figure 42 Numerically calculated transmittance in the 0.55-0.8 THz range for a 1D GMR filter with p=390 µm, w=351 µm, and d=100 µm (chip #1) versus the polymer imaginary refractive index.

The 1D design of the proposed filter resembles the design of the polarizer reported in chapter 2. In both cases, only the incoming THz beam that is polarized perpendicularly to the Al stripes, i.e. along the x-axis, can pass through the sample and can be measured by the detector. The other polarization component, which is parallel to the Al stripes, is totally reflected since the grating acts as a practically ideal mirror.

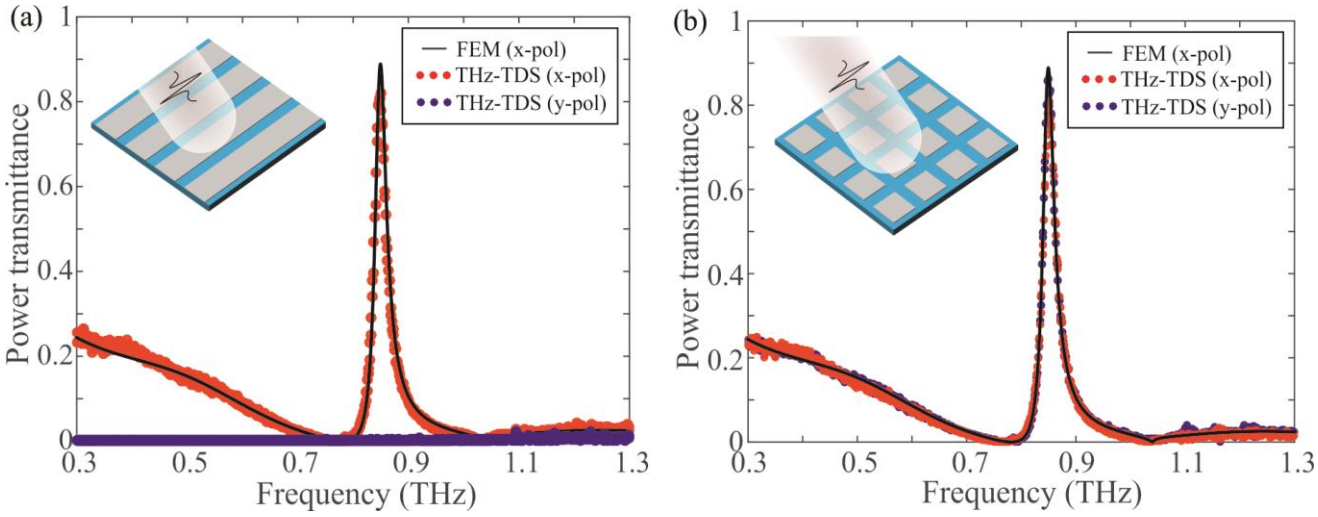

Figure 43: Transmittance for a a) 1D (chip #2) and b) 2D GMR filtering components (chip #3) with $p=p_x=p_y=288$ µm, $w=w_x=w_y=260$ µm, d=100 µm. Polarization-dependent and polarization-independent filtering is, respectively, achieved.

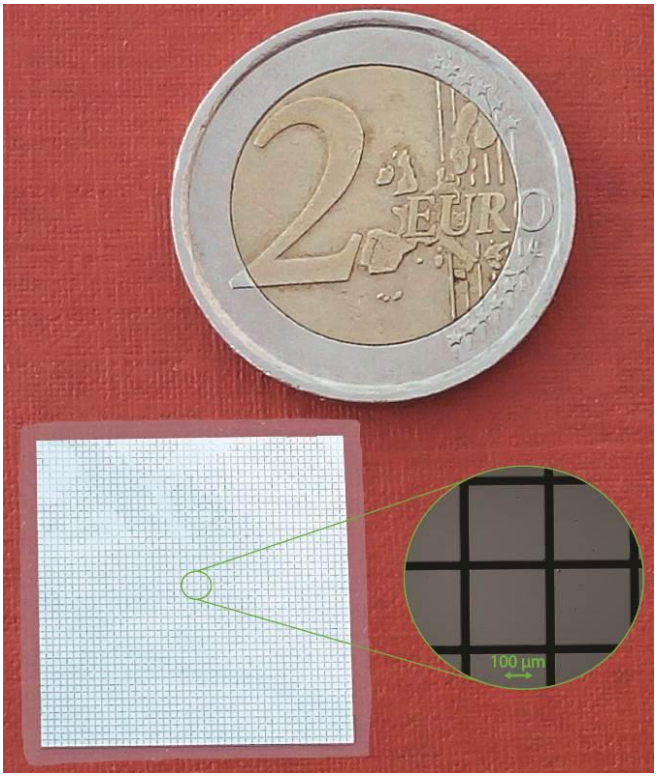

Figure 44: A photograph of chip #3 and a zoomed micrograph taken under microscope in reflection mode, showing the Al bi-dimensional grating defined by photolithography on the Zeonor® substrate.

The polarization-sensitive operation was experimentally studied in the case of chip #2, which is also based on 1D metallic pattern. The period and stripe width in chip #2 are 288 µm and 260 µm, respectively. The resulting resonant frequency is 850 GHz, in the second targeted spectral window. The numerical and experimental results agree very well, as observed in Figure 43, which also reports a comparison between chip #2 and chip #3. The latter is composed of a square lattice of Al patches with the same pitch and patch width of chip #2. Figure 43 (a) clearly demonstrates that the proposed 1D GMR-THz filters transmits only one polarization while the other is totally reflected, exhibiting

therefore a polarization-sensitive behaviour. Conversely, the 2D counterpart demonstrates a polarization-independent performance since the power transmittance is equal for both polarization components, as clearly shown in Figure 43 (b). This particular feature cannot be achieved in high-Q THz filters induced by symmetry breaking, which do not exhibit the C_4 symmetry of the square lattice GMR-THz filters. Moreover, it is worth noting that both filters have a peaks transmittance between 80-85% and a very good Q-factor, which exceeds 30.

The fabricated chip #3 is illustrated in Figure 44, which reports the photograph of the whole device while in the inset a micrograph of the patterned surface is shown. The latter, taken under optical microscope in reflection mode, shows the 2D pattern where the black lines represent the Zeonor® polymer while the greyish squares corresponds to the Al patches.

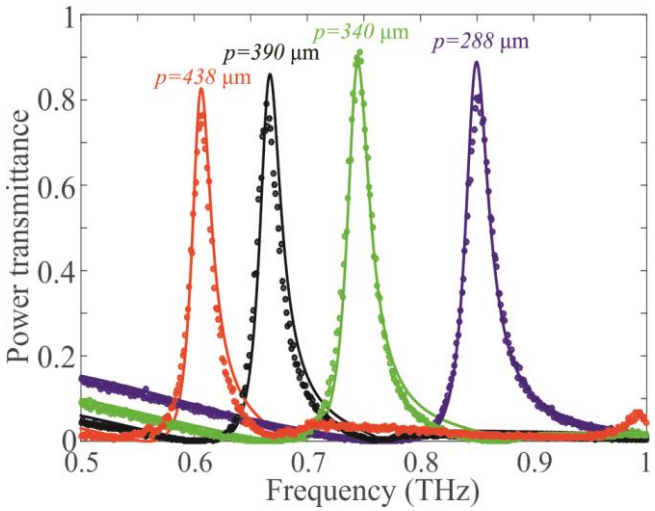

Figure 45: Numerically calculated and experimentally measured transmittance of 2D GMR filters for different values of the lattice pitch (chips #3-6). The fill factor is kept constant at 90% and d= 100 µm.

The exact position of the resonant frequencies mainly depends on the lattice pitch and the slab mode effective index that, for a fixed polymer material, is determined by the substrate thickness. Therefore, the spectral response of the filter can be modified by varying the pattern period and/or the substrate thickness. For a complete analysis, we first fixed the Zeonor® film thickness to 100 µm and varied the period of the metal patch; successively, we fixed the period to 288 µm and changed the substrate thickness. Results are reported in Figure 45 and Figure 46 respectively. In particular, Figure 45 shows the numerical and experimental comparison of the power transmittance of the fabricated chips #3-6 where the patch period varied from 288 to 438 µm. As expected, the longer the period the lower the resonant frequency. On the other hand, the transmittance and the quality factor are not influenced. For all chips, the peak transmittance is very high, above 80%, while the quality factor is around 30. Furthermore, very good agreement between FEM simulations and THz-TDS measurements is observed.

Figure 46 illustrates the numerically calculated and experimentally measured transmittance when the period is maintained constant to 288 μm and the Zeonor® substrate thickness varies from 40 to 130 μm. However, in this study the experimental results were reported for only two filters, according to the Zeonor® foils available to us, i.e. the ones with d=40 and 100 μm. A similar behavior of the previous case can be observed. As the film thickness shrinks, the slab modal index drops and thus the resonant frequency shifts towards the limit $f_{max}=c/p$, which is around 1.04 THz. This is also identifiable by observing the zero-transmittance point associated with Wood's anomaly [151]. It is remarked that for the case of d= 40 μm, an experimentally extremely high Q factor of 70 is achieved with a power transmittance around 80%. In addition, in this case the numerical and experimental results agree very well confirming the great accuracy of both the simulation and the fabrication-measurement steps.

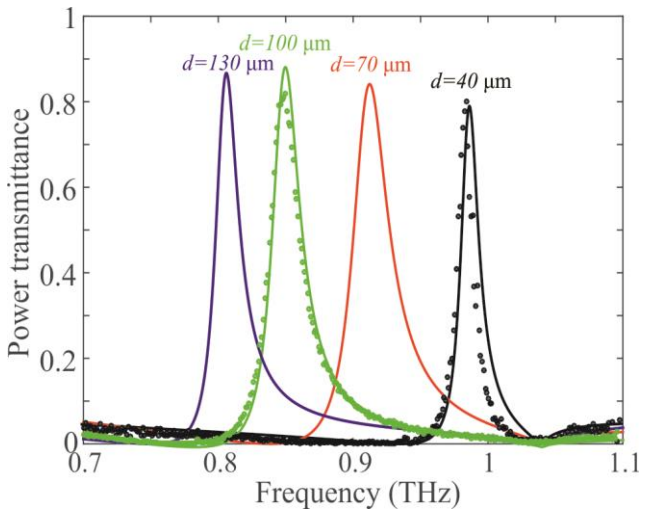

Figure 46: Numerically calculated and experimentally measured transmittance of 2D GMR filters for $p_x=p_y$=288 μm, $w_x=w_y$=260 μm and different values of the Zeonor® substrate thickness. The fabricated chips (chips #3 and #7) correspond to the only available Zeonor® film thicknesses of d=40 and 100 μm.

As we have already mentioned, until now, the fill factor of the metallic stripes/patches width w to the pitch p was a constant parameter equal to 0.9. However, in order to complete the investigation of this new class of filters, a study of the effect of a variation of the fill factor on the performance of the filters was performed.

We focused on chip #4 characterized by a period of 390 μm and the Zeonor® thickness of 100 μm. Then we varied the separation gap $s=p-w$ between adjacent Al patches from 60 μm to 0.5 μm. Figure 47 (a) reports the peak power transmittance whereas Figure 47 (b) the transmittance and quality factor as a function of the separation gap. As expected, shrinking the gap from 60 μm to 0.5 μm results in a narrower resonance (higher Q factor) at the expenses of a reduced transmittance. However, it is very important to remark that even for gap values below 1 μm, i.e. almost 500 times smaller than the free-space wavelength, a significant amount (above 30%) of THz power crosses through the filter. This

tight squeezing of electromagnetic radiation in extremely subwavelength slits and volumes has been observed in both non-diffracting gratings[181] and in GMR gratings working in the mid-infrared [162].

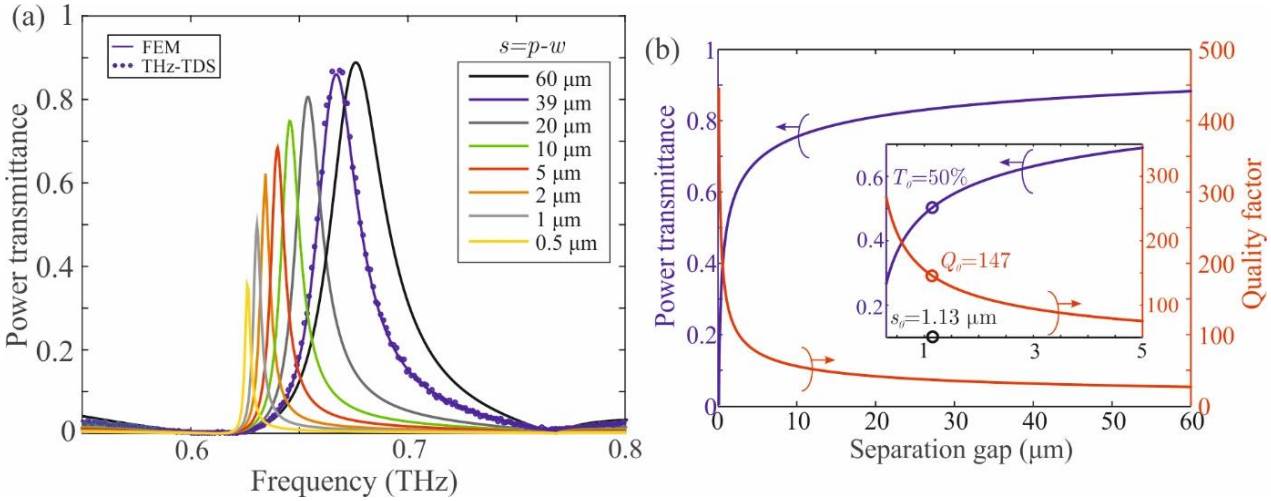

Figure 47: (a) Transmittance of a 2D GMR filter with p=390 μm and d=100 μm, as a function of the gap s=p-w in the Al patch lattice. (b) Dependence of the filter's transmittance and quality factor on the gap value. For s=1.13 μm (F=0.997), a Q=147 is obtained for 3 dB losses.

However, it is necessary to find a trade-off between high quality factor and high transmittance since, usually, they are inversely proportional. For this reason, Figure 47 (b) presents a design rule for the selection of the gap value, in accordance with the target performance characteristics. It is important to note that for s=1.13 μm that implies a fill factor equal to 0.997, a quality factor as high as 147 is obtained for insertion losses within 3 dB. With these geometrical parameters, the filters can be fabricated with standard UV photolithography without recurring to nano-fabrication techniques. The combination of such extremely high quality factors accompanied by single bandpass 50% transmittance and high out-of-band rejection has not yet been demonstrated in the field of THz filter technology to the best of our knowledge. This is the result of a careful design and of the intrinsic low loss of the material used for the substrate.

All the aforementioned investigation was conducted at normal incidence, therefore to conclude the analysis, we evaluated the spectral response of the filter at oblique incidence. It is well known that when a plane-wave impinges obliquely on a GMR filter the resonances for each diffracted mode split and follow two separate spectral branches as the angle of incidence increases. Figure 48 illustrates the comparison between the numerical and experimental results of the power transmittance for the chip #1 when the angle of incident varies from θ=0º, 2º, 4º, and 6º. The resonance splitting is evident and increases by increasing the incident angle. Furthermore, the results show excellent accordance between experiments and numerical modeling. The adjustment of the angle of incidence, using a

rotation stage as employed in the reported experiments, provides a means to tune dynamically the resonant frequency of the filter in a broad range and/or to achieve a dual-band operation.

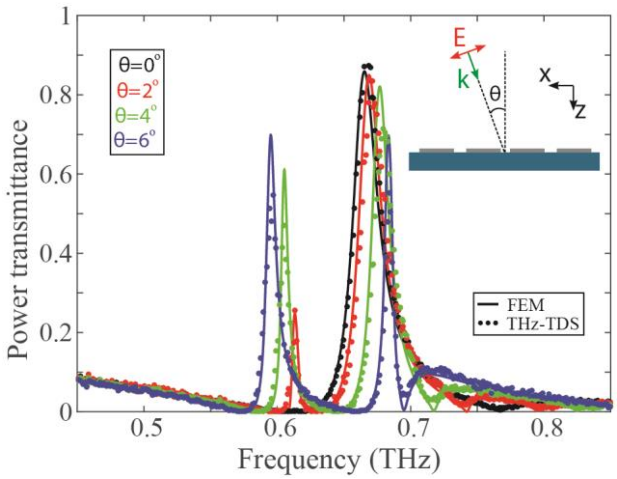

Figure 48: Numerically calculated and experimentally measured transmittance of chip #1 as a function of the angle of incidence of the probe radiation.

For example, when θ=6º the single narrow resonance observed at normal incidence degenerates into two narrower resonances at 595 GHz and 683.5 GHz. The transmittance for the two peaks is for both nearly 70 %, a bit lower from the 80% found at normal incidence. This little drawback is compensated, however, by much higher quality factors of 70 and 100, respectively, which favourably compares to the 29 value obtained at normal incidence. This feature could be helpful in applications when it is necessary to filter the transmit and receive communication channels with large out-of-band rejections using an individual simple filter.

4.4 Conclusion

In this chapter, we have reported a comprehensive numerical and experimental study of a new configuration of THz bandpass filtering elements based on the guided mode resonance effect. The proposed filters were fabricated by patterning 1D stripes or 2D square patches of aluminium on low loss Zeonor® polymer thin film substrates. The proposed filters combine all the six performance qualities illustrated in the introduction, such as high transmittance, narrow linewidth, high out-of-band rejection, compact dimensions, mechanical stability, and low manufacturing cost, which are for the first-time reported in the field of THz filter design. For instance, peak power transmittance values above 85% for Q values as high as 70, along with high out-of-band rejection, were measured. Moreover, by simple toggling the dimensionality of the patterned Al pattern the filters exhibited both polarization-selective and polarization-independent response.

One of the proposed filter was characterized at different incident angles showing a splitting of the GMR resonant frequency. This phenomenon can be exploited as a means to dynamically select the resonant frequency of the filter or to provide a double channel operation.

Even if the filters proposed in this chapter were explicitly engineered for operating in the two low loss THz atmospheric windows, the general design procedure and rules are also discussed.

Chapter 5:

Tuneable terahertz filters

Part of the work herein reported is reprinted/adapted, with permission, from [A. Ferraro, D.C. Zografopoulos, R. Caputo, and R. Beccherelli: 'Periodical Elements as Low-Cost Building Blocks for Tunable Terahertz Filters', IEEE Photonics Technology Letters, 2016]

5.1 Introduction

The previous chapters illustrate the experimental and numerical results of two classes of bandpass filters, namely frequency-selective surface (FSS) filter based on cross-shaped apertures [165], [166] and guided mode resonant (GMR) [175] based on 1D e 2D grating structures. Both filters have a common feature, i.e. they are composed of a thin layer of aluminium opportunely patterned on thin foils of Zeonor® polymer. Their fabrication process is very simple and involves a multi-step process including UV photolithography, as reported in chapter 2.

In this chapter, we present a low-cost mechanically tuneable Fabry-Perot filter [144], fabricated with a very simple stacking procedure [182] and successively characterized via THz time-domain spectroscopy. The filter is made of two Bragg mirrors put at controllable distance between each other. These mirrors are long known and broadly used in optical thin film technology [183]. In our case, the fabrication of the single Bragg mirror has been realized by simply alternating thin Zeonor® polymer layers separated by air gaps controlled by spacers made of bi-adhesive tape placed at the edge. The result is a low-cost building block showing a bandgap at a specific central frequency. When two of these blocks are facing each other and the periodicity is locally broken, e.g. by changing the thickness of one layer, localised defect modes appear in the bandgap and the whole device acts as a narrow bandpass filters. In an optical analogy, these filters can be thought of as Fabry-Perot interferometers, where the role of the reflective surfaces is played by the periodic Bragg reflectors. In our case, the defect cavity is void and its thickness is mechanically tuned by means of a translation stage. The filters show narrow linewidths and excellent transmittance thanks to the low loss of the Zeonor®

polymer [27]. Both the Bragg mirrors and the resulting bandpass Fabry-Perot are mechanically stable. In order to numerically predict the behaviour and provide general design rules of the proposed devices, an exhaustive parametric numerical study was performed.

5.2 Design

As mentioned, a Bragg mirror reflecting the incoming radiation at targeted frequency, constitutes the main component of the suggested tuneable filtering device. In theory, the former can be considered as a multilayer structure composed of a stack of alternated materials having different (high- and low-) refractive indices. In our case, the low-index material is air (n_a=1) while the Zeonor® film is the high-index one (n_z=1.525-j0.0013). Figure 49 illustrates the sketch of the proposed tuneable bandpass filter with the relevant geometric parameters as the period *p* of the Bragg structure and the quantities d_z, d_a and d_s respectively representing the thickness of the Zeonor® layer, the spacer and the defect cavity. The latter is mechanically controlled via a motorized PC-controlled linear translation stage. In details, Figure 49 (a) reports the 2D design of the basic element, which is constituted by a single stack Bragg mirror while Figure 49 (b) reports the 3D design of the proposed tuneable Fabry-Perot filter. The number of repeated pairs (N) of Zeonor®/Air layers in each Bragg mirror is equal to N= Z-1, where Z represent the number of Zeonor® layers.

The traditional design of a Bragg mirror is based on alternating layers with high and low refractive indices. For each layer, the optical layer thickness, defined as the product between refractive index and thickness, is one-quarter wave (in vacuum) at the targeted central frequency (f_0). This configuration gives the highest reflectivity. Equation (16) describes this concept.

$$f_0 = \frac{c_0}{4 n_i d_i} \tag{16}$$

being c_0 the speed of light in vacuum, n_i and d_i the refractive index and thickness of the layer where *i* stays for high- or low-index material.

In the employed devices, considering an operation frequency of 0.5 THz, (i.e.600 μm wavelength in vacuum) and n_a = 1 and n_z = 1.525-j0.0013 the resulting air spacer thickness (d_a) is 152 μm while the Zeonor® one (d_z) is 100 μm. Considering a multilayer stack, the reflection (*r*) of a single Bragg mirror stack is given by Equation (17) [183], [184]:

$$r = \frac{n_0 (n_2)^{2N} - n_s (n_1)^{2N}}{n_0 (n_2)^{2N} + n_s (n_1)^{2N}} \tag{17}$$

where n_o is the refractive index of the originated medium, n_1 and n_2, the indices of the alternating materials and n_s, the one of the substrate. In our case, Equation (17) simplifies to:

$$r = \frac{n_a(n_z)^{2N} - n_a(n_a)^{2N}}{n_a(n_z)^{2N} + n_a(n_a)^{2N}} \tag{18}$$

where n_a is the refractive index of air and n_z of Zeonor®.

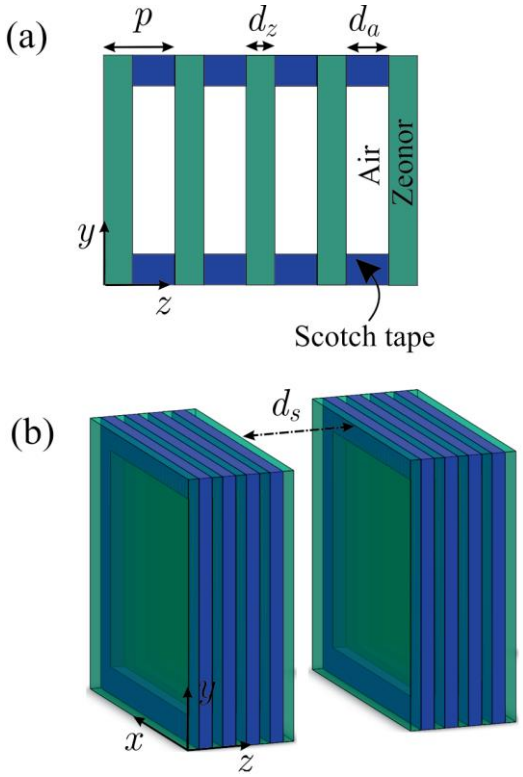

Figure 49: (a) 2D schematic drawing of a single stack Bragg mirror, (b) 3D schematic drawing of the proposed Fabry-Perot filter where p is the period of the Bragg structure, d_z, d_a and d_s represent the thickness of Zeonor® layer film, spacer and defect cavity respectively. The length of the defect cavity d_s is mechanically controlled via a linear translation stage.

From the reflection coefficient, we retrieve the transmission coefficient (*t*) as *t=1-r*, if the absorption can be neglected. Hereafter, we report the spectral response of the proposed devices in terms of transmittance since the tuneable filter exhibit a bandpass behaviour. From Equation (18) it is clear that the transmission depends on the number of pairs (N) in an inversely proportional way, namely by increasing N the transmittance in the bandgap decreases, as observed in Figure 50. The latter reports the numerical results, obtained by simulating with the commercial solver COMSOL Multiphysics©, the normalized electric field transmittance for a Zeonor® stack with d_z = 100 μm and d_a = 152 μm as a function of the number of repeated pairs (N). The normalized electric field transmittance is calculated as the ratio between the electric field transmission through the sample divided by the transmission without sample. It is remarked, that as in the previous chapters, the numerical analyses took into account the absorption loss of the polymer substrate Zeonor®.

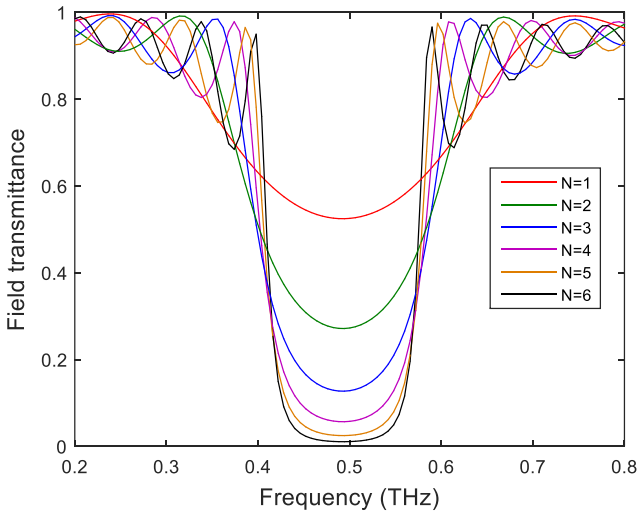

Figure 50: Simulations results of the normalized electric field transmittance $|E_t/E_{ref}|$ for a Zeonor® stack setting d_z=100 µm, d_a = 152 µm versus the number of repeated pairs (N).

The spectral width (Δf_0) of the obtained bandgap is given by:

$$\Delta f_0 = f_0 \frac{4}{\pi} arcsin\left(\frac{n_2 - n_1}{n_2 + n_1}\right) \qquad (19)$$

that for $n_1 = n_a$ and $n_2 = n_z$ becomes

$$\Delta f_0 = f_0 \frac{4}{\pi} arcsin\left(\frac{n_z - n_a}{n_z + n_a}\right) \qquad (20)$$

From Equation (19), it is evident that the bandwidth increases by increasing the refractive index contrast between the two alternating materials. Moreover, in Figure 50, it is possible to note that, by increasing N, the edge of the bandgap is steeper due to the increasing reflectance. For N=6, the bandgap is 165 GHz wide.

Figure 51, instead, reports the numerical results of the normalized electric field transmittance for a single Bragg mirror having 6 repeated pairs (N) for three different values (40, 50 and 60 µm) of the Zeonor® layer thickness. For each value, the corresponding d_a thickness is the ideal one for having a quarter-wave design, namely 61, 76 and 91 µm respectively. It is remarked that, as expected from the above Equation (16), the central frequency shifts toward the lower edge as the Zeonor® thickness increases. This shift results in the reduction of the bandgap width that decreases from 420 GHz to 250 GHz. Equation (19) describes this phenomenon where Δf_0 is proportional to f_0. In fact, by considering the relative spectral width ($f_0/\Delta f_0$), a 0.3 value is obtained in all cases. Moreover, it is remarked that, due to the absorption loss of the polymer, the transmittance in the bandgap decrease as the polymer thickness increase.

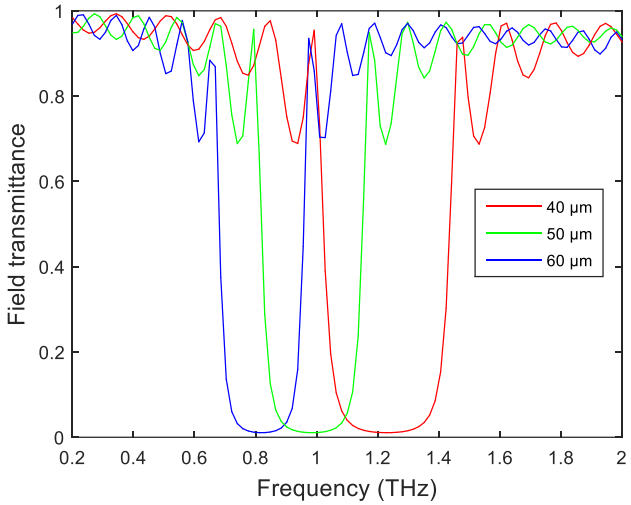

Figure 51: Simulations results of the normalized electric field transmittance | E_t/E_{ref} | for a single 6 repeated pairs (N) stack with ideal spacer thickness (d_a). For Zeonor® thickness (d_z) of 40, 50 and 60 µm the respectively ideal spacer thickness (d_a) is 61, 76, 91 µm.

For a detailed analysis of the Bragg mirror employed in this work, we fixed the Zeonor® thickness to 100 µm and varied the spacer thickness (d_a) from 100 to 200 µm, the results are illustrated in Figure 52. As predictable, the change in d_a results in a variation of the optical thickness, hence in a shift of the central frequency and, consequently, of the whole bandgap. As for the case reported in Figure 51, here we found a reduction in the width of the bandgap as the central frequency decreases.

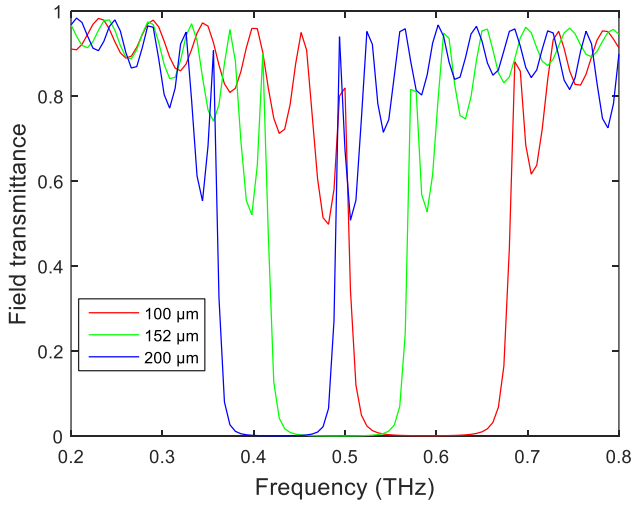

Figure 52: Simulations results of the normalized electric field transmittance | E_t/E_{ref} | for a single 6 repeated pairs (N) stack where the Zeonor® thickness (d_z) is 100 µm versus the spacer thickness (d_a).

After considering the behaviour of the single building block, we performed a numerical analysis on a Fabry-Perot filter constituted by two Bragg mirrors separated by a defect cavity having thickness d_s. In such configuration, similar to what happens in a photonic crystal, the cavity represents a resonator while the Bragg mirrors act as perfect reflectors. Hence, a narrow bandpass peak within the bandgap can be obtained. The central frequency of this peak depends on the optical thickness of the cavity, as illustrated in Figure 53 and Figure 54. In particular, Figure 53 shows the numerical simulation of the

normalized electric field transmittance for Fabry-Perot filter composed by two Bragg mirrors with 6 repeated pairs (N) of Zeonor® layer and air spacer, 100 and 152 µm thick, respectively, where the defect cavity thickness (d_s) is 100, 200 and 300 µm wide.

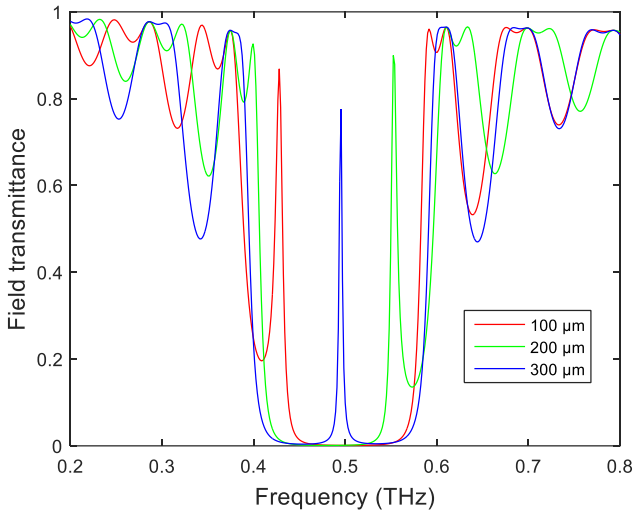

Figure 53: Simulations results of the normalized electric field transmittance | E_t/E_{ref} | for a single 6 repeated pairs (N) stack Fabry-Perot filter where the Zeonor® thickness (d_z) is 100 µm, the spacer thickness is 152 µm versus the defect cavity thickness (d_s).

In Figure 54, the resonator is studied as a possible sensor. The refractive index (n_d) of the defect cavity is varied while its thickness is fixed at 152 µm. For n_d=1 the whole device is still periodic and only the bandgap is obtained. For $n_d > 1$, the defect cavity breaks the periodicity with another optical thickness and the bandpass peaks appear.

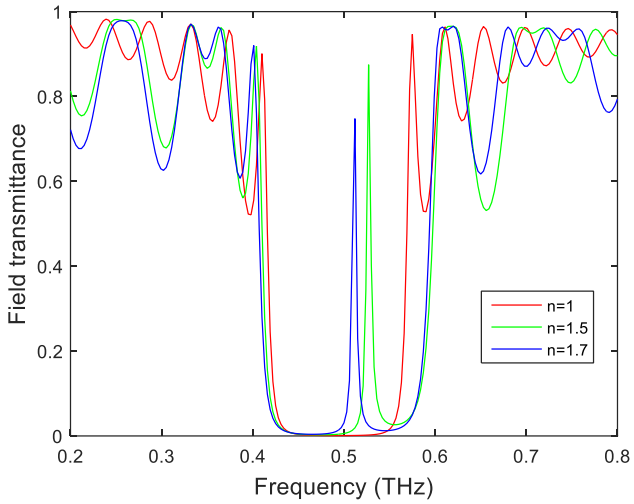

Figure 54: Simulations results of the normalized electric field transmittance | E_t/E_{ref} | for single 6 repeated pairs (N) stack Fabry-Perot filter where the Zeonor® thickness (d_z) is 100 µm, the spacer and defect thickness is 152 µm versus the refractive index of the cavity (n_d).

5.2 Experimental results

Based on the above numerical analysis, we fabricated the two Bragg mirrors building blocks and realized the tuneable Fabry-Perot filter. Figure 55 reports a photograph of one of the fabricated Bragg mirror.

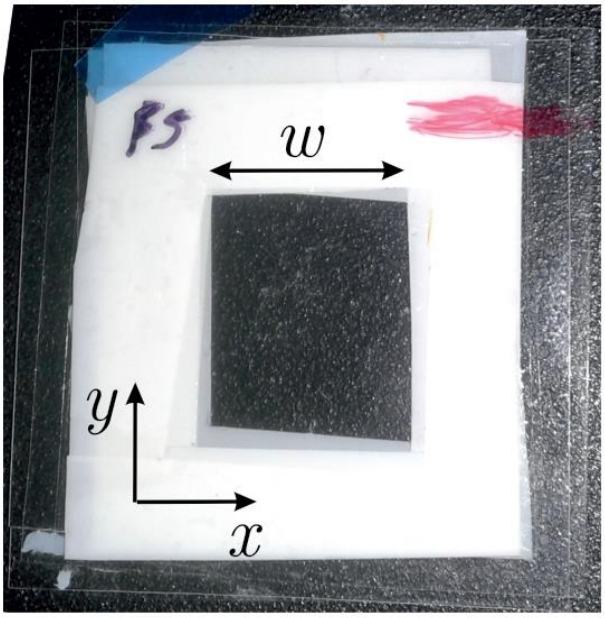

Figure 55: Photo of the fabricated Zeonor®/air Bragg mirror stack with an approximately square area with (w) of 1.5 cm.

The Bragg mirrors are easily assembled by alternating 100 μm thick Zeonor® foils separated by 125 μm spacing (d_a) defined by a simple bi-adhesive tape located outside the active area. Even if the spacer thickness is not optimized for a quarter-wave operation, it allows a very low cost and simple manufacturing process that can be easily customized to obtain different filter properties. Furthermore, since lithography or other critical process are not involved, it can be easily scaled to batch processing with the use of simple equipment. Each Bragg mirror is composed of five Zeonor® foils and four air gaps, therefore of four Zeonor®/Air pairs. The total thickness, measured with a micrometer, is 1 mm and it is uniform over the spacer frame while the active area is 1.5x1.5 cm^2.

The experimental characterization was performed using the Menlo K15 THz Time Domains Spectroscopy (TDS) setup in transmission mode by means of a collimated beam with 1cm diameter. First we characterized a single Bragg mirror several times, successively a second identical stack was mounted on a micron-precision PC-controlled linear translation stage on the same rail. In this way, it is possible to move one of the stack while the other remains fixed. Therefore, the distance between the stacks and hence the thickness of the defect cavity can be adjusted with micron accuracy. This mechanical tuning process allows to choose from a double Bragg mirror response, when $d_s=d_a$, to a

bandpass filter when the periodicity is broken. Moreover, in the latter case, the transmitted peak can be easily selected by varying the defect thickness, as we reported later on.

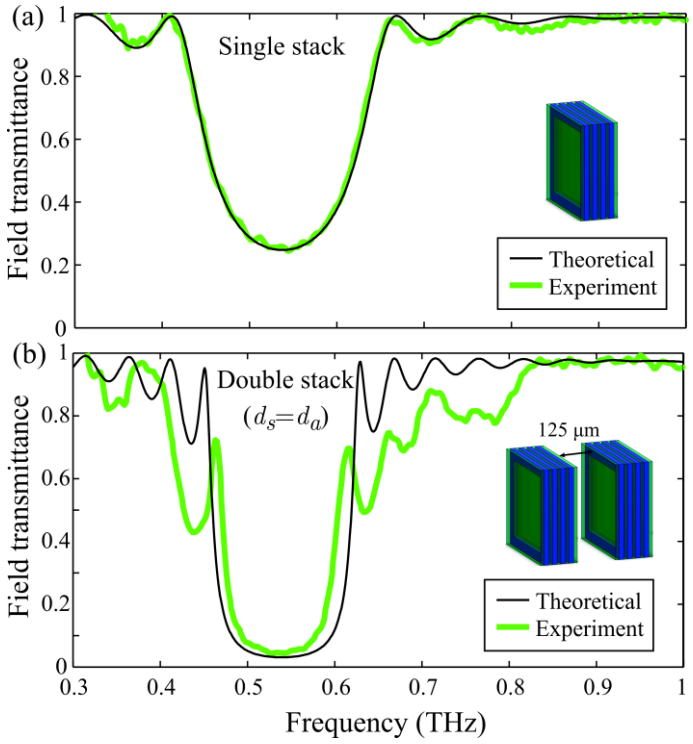

Figure 56: Experimental measurement and reference simulations of the normalized electric field transmittance | E_t/E_{ref} | for (a) a single 5-layer Zeonor® stack, i.e. 4 pairs and (b) a double periodic stack by setting $d_s = d_a = 125$ μm.

Figure 56 shows the comparison between the numerical simulations and the experimental results of the normalized electric field transmittance for a single Bragg mirror and for a double stack, Figure 56 (a) and (b), respectively. The former evidences an excellent agreement with the numerical results, confirmed by several measurements on both stacks, and exhibiting a central frequency at 0.54 THz and a width of 150 GHz. Then, a second Bragg mirror was mounted on the translation stage in order to perform a set of measurements at different d_s. The distance between the Bragg mirrors was set as $d_s = d_a = 125$ μm, hence the resulting device is still periodic with ten Zeonor® foils and nine air gap overall, and the spectral response is still a bandgap but with electric field transmittance below 10% in the entire region.

Successively, the periodicity is broken by mechanically tuning the distance d_s. This allows choosing the exact spectral position of narrow-band filters, namely the modes of the defect cavity. Results are illustrated in Figure 57. In order to demonstrate that a very narrow bandpass peak can be obtained in all the bandgap, we performed a characterization selecting six different value of the cavity thickness. From the figure, it is remarked that the number of defect modes depends on the d_s values, in fact when the latter exceeds the THz wavelength under consideration, more than one defect mode appears in the

bandgap as observed for the case d_s equal to 730 or 2000 μm. In other cases, we have only a defect mode whose position can be easily tuned.

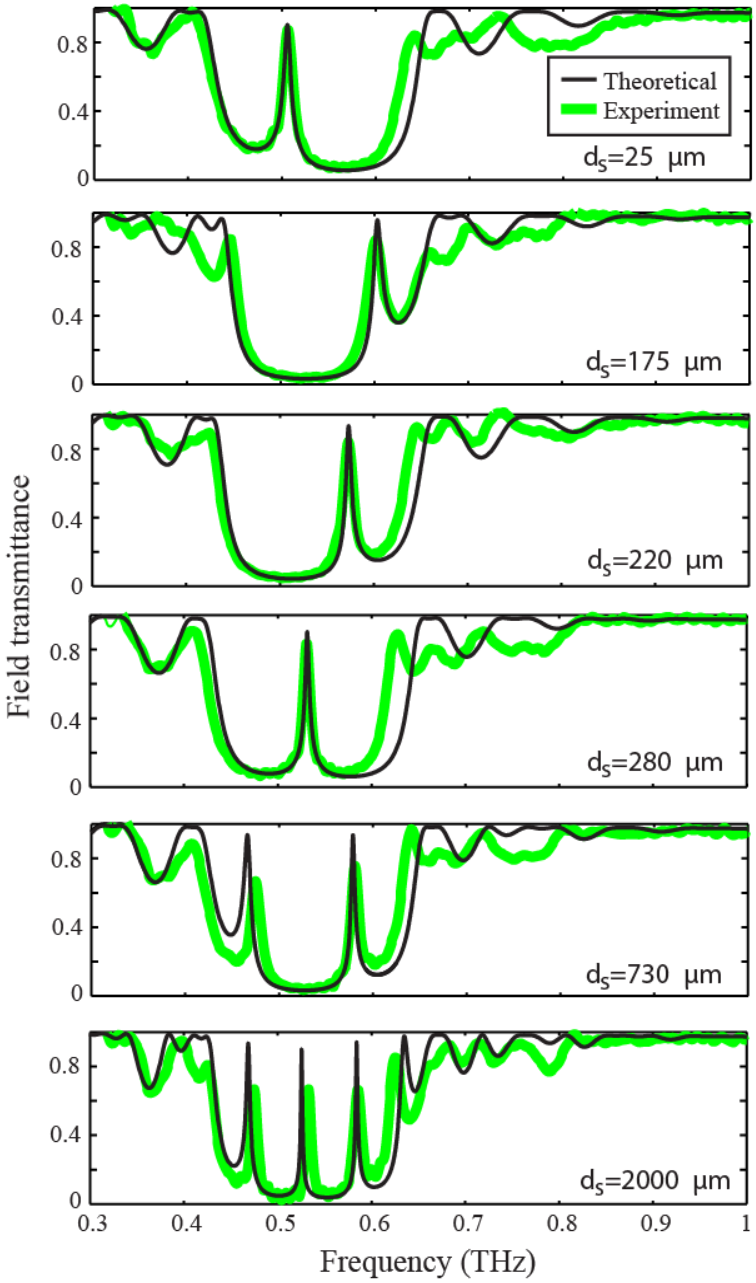

Figure 57: Mechanical tuning of the bandgap defect modes by controlling the distance between the two Bragg reflector stacks.

For all configurations, and hence defect modes, the experimental full-width at half-maximum (FWHM) was derived and compared to the simulated one showing a good accordance, as can be noted in Table 2. The latter, moreover, reports a comparison between the measured and the simulated central frequency and the electric field amplitude for the various defect modes originated at different defect layer thickness.

Table 2: Central frequency, electric field transmittance and FWHM of the mechanically tunable THz filter for various values of the defect cavity thickness.

d_s [μm]	f_0^{meas} [GHz]	f_0^{sim} [GHz]	$FWHM^{meas}$ [GHz]	$FWHM^{sim}$ [GHz]	E_t^{meas} [%]	E_t^{sim} [%]
25	506	506	15	12	89	90
175	601	604	27	16	84	95
220	573	573	15	9	84	93
280	530	532	10	7	83	90
730	475	470	15	13	67	93
730	580	580	12	6	75	93
2000	475	472	9	6	66	86
2000	533	530	7	2.5	66	90
2000	586	585	11	3.5	66	93

The measured central frequencies and linewidths of the various modes agree very well with the numerical simulations, while the filter peak intensity tends to become lower for increasing d_s.
This is attributed to slight misalignments between the faces of the two mounted Bragg mirrors and the limited resolution of 1 GHz of the measurement system, especially for high values of the defect cavity thickness. In fact, the case of very high values of d_s, i.e. 730 and 2000 μm are more sensitive to misalignments between the two mounted Bragg reflectors. Regarding the intensity, instead, the difference between the measured and simulated results can be due to higher absorption losses of the used Zeonor® foils when compared to the value n_z used in the calculations.

5.4 Conclusion

To sum up, we illustrated a novel tuneable bandpass filter based on Bragg mirror building blocks. In the first part of this chapter, a detailed study of the Bragg mirror structure and of the Fabry-Perot filter was performed by varying the principal parameters, i.e. thickness and refractive index of the repeated layer or of the defect cavity. Successively two Bragg mirrors were fabricated by stacking 100 μm thick foils of Zeonor® polymer separated by a frame of bi-adhesive tape. This solution represents a simple and very low-cost process for the fabrication of mechanically tuneable Bragg mirrors and

filters. In particular, the former exhibits a bandgap having central frequency of 0.54 THz and width of 150 GHz.

By combining the two building blocks and controlling their distance, the central frequency of narrow linewidth filters (appearing after breaking the periodicity) can be tuned within the entire bandgap. By properly selecting the defect cavity thickness, filters with a FWHM down to a few GHz have been demonstrated.

Conclusions

In this thesis, we carried out a research work aiming at the design, fabrication and characterization of novel low cost THz devices with outstanding properties. Common denominator of all devices is the Zeonor® cyclo-olefin polymer used as a substrate that possesses extraordinary characteristics, such as very low absorption loss, high mechanical stability, low water absorption and low cost. The procedure for the optimization of the design of the proposed devices has been performed by means of Finite Element Method (FEM) implemented in a commercial software. Successively the devices have been fabricated using standard UV-photolithography, except for of the tuneable Fabry-Perot filters. All the experimental measurements agree very well with the simulation results confirming the great quality of the work both in term of simulation and fabrication.

In particular, in Chapter 1 the THz radiation have been presented with a focus, also, on the potential market and on most common sources and detectors. Moreover, the applications in multidisciplinary fields of the THz wave have been described in detail. An exhaustive investigation on various materials to be used as substrate have been conducted, and the results have led to select the Zeonor® cyclo-olefin polymer, manufactured by Zeon Co, used for all devices presented in this thesis.

In Chapter 2, two wire grid polarizers have been illustrated exhibiting very low insertion losses and high extinction ratio. The latter has a value between 30 and 45 dB in the 0.3-2.5 THz range while the former is below 1.1 dB. Moreover, due to a refractive index of about 1.52, the polarizers have shown impedance matching behaviour and almost total transmittance at different frequencies for all considered Zeonor® thickness values. Finally, for the 100 μm thick Zeonor® have been demonstrated that its high-performance characteristics are preserved even when the latter is bent up to a curvature radius of 12.5 mm. Furthermore, a systematic parametric evaluation has been performed by varying the wire grid period, fill factor and polymer substrate.

Chapter 3 describes numerical and experimental investigations of aluminium based cross-aperture FSS bandpass filters on Zeonor® foil substrate, explaining in more detail the effect of the polymer on the overall performance of the filters. The presence of the substrate is responsible of a secondary effect that hasbeen observed in the fabricated filter, namely a series of Fano-like asymmetric narrow-line transmission peaks at higher frequencies that have been originated by the Guide Mode Resonance (GMR). A comprehensive study has been conducted in order to retrieve the parameters influencing the spectral response of the proposed filters. Moreover, a detailed analysis by taking in consideration angles of incidence and polarization of the incoming THz wave has been reported, demonstrating the

possibility to tune mechanically the properties of the proposed filters. Contrary to what happens for the polarizer, when the filter has been measured in bending condition the GMR peaks vanish while the FSS principal peak remains unaffected.

Based on the GMR concept, in Chapter 4, a new classes of high quality THz bandpasss filter has been presented. The spectral response has been focused on the two THz low-loss wireless communication windows approximately centered at 0.67 THz and 0.85. Furthermore, peak power transmittance values above 85%, associated with a Q factor of 70, along with the high out-of-band rejection, have been experimentally measured. Finally, a theoretical parametric analysis is presented to provide some guidelines on the design of the proposed filters.

The fifth and last chapter was dedicated to the analysis of a simple and very low-cost way for the fabrication of mechanically tunable Bragg mirrors and Fabry-Perot filters for THz applications. The Bragg mirrors have been realized by stacking thin foils of Zeonor® polymer, showing a bandgap centered at 0.54 THz and width of 150 GHz. These mirrors constituted the building blocks of a tunable Fabry-Perot filters whose central frequency possesses very high Q factor, in some case its bandwidth was few GHz.

To sum up, innovative THz devices with improved performance have been numerically and experimentally presented. These low-cost devices can pave the way for a new class of THz low cost components.

References

[1] "https://en.wikipedia.org/wiki/Terahertz_radiation." .

[2] P. H. Siegel, "Terahertz technology," *IEEE Trans. Microw. Theory Tech.*, vol. 50, no. 3, pp. 910–928, Mar. 2002.

[3] A. Rostami, H. Rasooli, and H. Baghban, *Terahertz technology : fundamentals and applications*. Heidelberg: Springer, 2011.

[4] Y.-S. Lee, *Principles of Terahertz Science and Technology*. Springer Publishing Company, Incorporated, 2008.

[5] X.-C. Zhang and J. Xu, *Introduction to THz Wave Photonics*. Boston, MA: Springer US, 2010.

[6] "https://en.wikipedia.org/wiki/X-ray." .

[7] E. Bründermann, H.-W. Hübers, and M. F. Kimmitt, *Terahertz techniques*. Berlin: Springer, 2012.

[8] "Terahertz absorption spectrum of para and ortho water vapors at different humidities at room temperature," *J. Appl. Phys.*, vol. 100, no. 9, p. 094905, Nov. 2006.

[9] T. Hochrein, "Markets, Availability, Notice, and Technical Performance of Terahertz Systems: Historic Development, Present, and Trends," *J. Infrared Millim. Terahertz Waves*, vol. 36, no. 3, pp. 235–254, Mar. 2015.

[10] "http://tematys.fr/Publications/en/terahertz/39-terahertz-components-systems-technology-and-market-trends-update-2016.html." .

[11] "http://www.thintri.com/Terahertz-report.htm." .

[12] "http://www.reportlinker.com/p097906-summary/Terahertz-Radiation-Systems-Technologies-And-Global-Markets.html." .

[13] "https://globenewswire.com/news-release/2016/02/19/812278/0/en/Terahertz-Components-and-Systems-Market-to-Reach-US-415-0-mn-by-2023-Transparency-Market-Research.html." .

[14] G. Liu, "Visualization of patents and papers in terahertz technology: a comparative study," *Scientometrics*, vol. 94, no. 3, pp. 1037–1056, Mar. 2013.

[15] "Scopus - Welcome to Scopus." [Online]. Available: https://www.scopus.com/. [Accessed: 21-Jan-2017].

[16] "The Lens." [Online]. Available: https://www.lens.org/lens/. [Accessed: 21-Jan-2017].

[17] D. Saeedkia, *Handbook of Terahertz Technology for Imaging, Sensing and Communications*. Elsevier, 2013.

[18] H. B. Liu, H. Zhong, N. Karpowicz, Y. Chen, and X. C. Zhang, "Terahertz Spectroscopy and Imaging for Defense and Security Applications," *Proc. IEEE*, vol. 95, no. 8, pp. 1514–1527, Aug. 2007.

[19] I. F. Akyildiz, J. M. Jornet, and C. Han, "Terahertz band: Next frontier for wireless communications," *Phys. Commun.*, vol. 12, pp. 16–32, Sep. 2014.

[20] A. Cosentino, "Terahertz and Cultural Heritage Science: Examination of Art and Archaeology," *Technologies*, vol. 4, no. 1, 2016.

[21] A. G. Davies, A. D. Burnett, W. Fan, E. H. Linfield, and J. E. Cunningham, "Terahertz spectroscopy of explosives and drugs," *Mater. Today*, vol. 11, no. 3, pp. 18–26, 2008.

[22] K. Kawase, Y. Ogawa, Y. Watanabe, and H. Inoue, "Non-destructive terahertz imaging of illicit drugs using spectral fingerprints," *Opt. Express*, vol. 11, no. 20, pp. 2549–2554, Oct. 2003.

[23] K. Kawase, "Terahertz Imaging For Drug Detection And Large-Scale Integrated Circuit Inspection," *Opt. Photonics News*, vol. 15, no. 10, pp. 34–39, Oct. 2004.

[24] D. Zimdars and J. S. White, "Terahertz reflection imaging for package and personnel inspection," 2004, vol. 5411, pp. 78–83.

[25] "An Industrial THz Killer Application? | Optics & Photonics News." [Online]. Available: http://www.osa-opn.org/home/articles/volume_26/november_2015/departments/an_industrial_thz_killer_application/.

[26] M. Naftaly and R. E. Miles, “Terahertz Time-Domain Spectroscopy for Material Characterization,” *Proc. IEEE*, vol. 95, no. 8, pp. 1658–1665, Aug. 2007.
[27] A. Podzorov and G. Gallot, “Low-loss polymers for terahertz applications,” *Appl. Opt.*, vol. 47, no. 18, pp. 3254–3257, 2008.
[28] P. A. George, W. Hui, F. Rana, B. G. Hawkins, A. E. Smith, and B. J. Kirby, “Microfluidic devices for terahertz spectroscopy of biomolecules,” *Opt. Express*, vol. 16, no. 3, pp. 1577–1582, Feb. 2008.
[29] M. Scheller, C. Jansen, and M. Koch, “Analyzing sub-100-µm samples with transmission terahertz time domain spectroscopy,” *Opt. Commun.*, vol. 282, no. 7, pp. 1304–1306, Apr. 2009.
[30] C. Russell *et al.*, “Integrated On-Chip THz Sensors for Fluidic Systems Fabricated Using Flexible Polyimide Films,” *IEEE Trans. Terahertz Sci. Technol.*, vol. 6, no. 4, pp. 619–624, Jul. 2016.
[31] M. Naftaly and R. E. Miles, “Terahertz time-domain spectroscopy: A new tool for the study of glasses in the far infrared,” *J. Non-Cryst. Solids*, vol. 351, no. 40–42, pp. 3341–3346, Oct. 2005.
[32] R. Piesiewicz, C. Jansen, S. Wietzke, D. Mittleman, M. Koch, and T. Kürner, “Properties of Building and Plastic Materials in the THz Range,” *Int. J. Infrared Millim. Waves*, vol. 28, no. 5, pp. 363–371, Apr. 2007.
[33] W. Tu, S. Zhong, Y. Shen, and A. Incecik, “Nondestructive testing of marine protective coatings using terahertz waves with stationary wavelet transform,” *Ocean Eng.*, vol. 111, pp. 582–592, Jan. 2016.
[34] J.-W. Park *et al.*, “Terahertz radiation NDE of composite materials for wind turbine applications,” *Int. J. Precis. Eng. Manuf.*, vol. 15, no. 6, pp. 1247–1254, Jun. 2014.
[35] J. Kitagawa, T. Ohkubo, M. Onuma, and Y. Kadoya, “THz spectroscopic characterization of biomolecule/water systems by compact sensor chips,” *Appl. Phys. Lett.*, vol. 89, no. 4, p. 041114, Jul. 2006.
[36] K. Ahi and M. Anwar, “Advanced terahertz techniques for quality control and counterfeit detection,” 2016, vol. 9856, p. 98560G–98560G–14.
[37] G. Ok, K. Park, H. J. Kim, H. S. Chun, and S.-W. Choi, “High-speed terahertz imaging toward food quality inspection,” *Appl. Opt.*, vol. 53, no. 7, pp. 1406–1412, Mar. 2014.
[38] C. D. Stoik, M. J. Bohn, and J. L. Blackshire, “Nondestructive evaluation of aircraft composites using transmissive terahertz time domain spectroscopy,” *Opt. Express*, vol. 16, no. 21, pp. 17039–17051, Oct. 2008.
[39] C. Jansen, S. Wietzke, H. Wang, M. Koch, and G. Zhao, “Terahertz spectroscopy on adhesive bonds,” *Polym. Test.*, vol. 30, no. 1, pp. 150–154, Feb. 2011.
[40] F. Rutz, M. Koch, S. Khare, M. Moneke, H. Richter, and U. Ewert, “TERAHERTZ QUALITY CONTROL OF POLYMERIC PRODUCTS,” *Int. J. Infrared Millim. Waves*, vol. 27, no. 4, pp. 547–556, Apr. 2006.
[41] M. Haaser, K. C. Gordon, C. J. Strachan, and T. Rades, “Terahertz pulsed imaging as an advanced characterisation tool for film coatings—A review,” *Int. J. Pharm.*, vol. 457, no. 2, pp. 510–520, Dec. 2013.
[42] K. Krügener *et al.*, “Terahertz meets sculptural and architectural art: Evaluation and conservation of stone objects with T-ray technology,” *Sci. Rep.*, vol. 5, Oct. 2015.
[43] C. Jördens *et al.*, “Terahertz spectroscopy to study the orientation of glass fibres in reinforced plastics,” *Compos. Sci. Technol.*, vol. 70, no. 3, pp. 472–477, Mar. 2010.
[44] S. Wietzke, C. Jansen, F. Rutz, D. M. Mittleman, and M. Koch, “Determination of additive content in polymeric compounds with terahertz time-domain spectroscopy,” *Polym. Test.*, vol. 26, no. 5, pp. 614–618, Aug. 2007.
[45] N. Krumbholz *et al.*, “Monitoring polymeric compounding processes inline with THz time-domain spectroscopy,” *Polym. Test.*, vol. 28, no. 1, pp. 30–35, Feb. 2009.
[46] C. D. Stoik, M. J. Bohn, and J. L. Blackshire, “Nondestructive evaluation of aircraft composites using transmissive terahertz time domain spectroscopy,” *Opt. Express*, vol. 16, no. 21, pp. 17039–17051, Oct. 2008.
[47] K. Fukunaga, “21 - Terahertz applications in art conservation A2 - Saeedkia, Daryoosh,” in *Handbook of Terahertz Technology for Imaging, Sensing and Communications*, Woodhead Publishing, 2013, pp. 615–623.

[48] J. B. Jackson *et al.*, “A Survey of Terahertz Applications in Cultural Heritage Conservation Science,” *IEEE Trans. Terahertz Sci. Technol.*, vol. 1, no. 1, pp. 220–231, Sep. 2011.
[49] “PlasThick - TeTechS.” [Online]. Available: http://tetechs.com/plasthick/.
[50] K. Su, Y. C. Shen, and J. A. Zeitler, “Terahertz Sensor for Non-Contact Thickness and Quality Measurement of Automobile Paints of Varying Complexity,” *IEEE Trans. Terahertz Sci. Technol.*, vol. 4, no. 4, pp. 432–439, Jul. 2014.
[51] S. Krimi, J. Klier, J. Jonuscheit, G. von Freymann, R. Urbansky, and R. Beigang, “Highly accurate thickness measurement of multi-layered automotive paints using terahertz technology,” *Appl. Phys. Lett.*, vol. 109, no. 2, p. 021105, Jul. 2016.
[52] C. Jördens, S. Wietzke, M. Scheller, and M. Koch, “Investigation of the water absorption in polyamide and wood plastic composite by terahertz time-domain spectroscopy,” *Polym. Test.*, vol. 29, no. 2, pp. 209–215, Apr. 2010.
[53] F. Ospald *et al.*, “Aeronautics composite material inspection with a terahertz time-domain spectroscopy system,” *Opt. Eng.*, vol. 53, no. 3, pp. 031208–031208, 2013.
[54] D. T. Petkie *et al.*, “Nondestructive terahertz imaging for aerospace applications,” 2009, vol. 7485, p. 74850D–74850D–9.
[55] M. Schirmer, M. Fujio, M. Minami, J. Miura, T. Araki, and T. Yasui, “Biomedical applications of a real-time terahertz color scanner,” *Biomed. Opt. Express*, vol. 1, no. 2, pp. 354–366, Sep. 2010.
[56] P. Bawuah *et al.*, “Detection of porosity of pharmaceutical compacts by terahertz radiation transmission and light reflection measurement techniques,” *Int. J. Pharm.*, vol. 465, no. 1–2, pp. 70–76, Apr. 2014.
[57] R. P. Cogdill *et al.*, “Comparison of Terahertz Pulse Imaging and Near-Infrared Spectroscopy for Rapid, Non-Destructive Analysis of Tablet Coating Thickness and Uniformity,” *J. Pharm. Innov.*, vol. 2, no. 1–2, pp. 29–36, Oct. 2007.
[58] M. Haaser *et al.*, “Application of terahertz pulsed imaging to analyse film coating characteristics of sustained-release coated pellets,” *Int. J. Pharm.*, vol. 457, no. 2, pp. 521–526, Dec. 2013.
[59] C. J. Strachan, T. Rades, D. A. Newnham, K. C. Gordon, M. Pepper, and P. F. Taday, “Using terahertz pulsed spectroscopy to study crystallinity of pharmaceutical materials,” *Chem. Phys. Lett.*, vol. 390, no. 1–3, pp. 20–24, May 2004.
[60] Y.-C. Shen, “Terahertz pulsed spectroscopy and imaging for pharmaceutical applications: A review,” *Int. J. Pharm.*, vol. 417, no. 1–2, pp. 48–60, Sep. 2011.
[61] S. Zhong *et al.*, “Non-destructive quantification of pharmaceutical tablet coatings using terahertz pulsed imaging and optical coherence tomography,” *Opt. Lasers Eng.*, vol. 49, no. 3, pp. 361–365, Mar. 2011.
[62] J. Labaune, J. B. Jackson, S. Pagès-Camagna, I. N. Duling, M. Menu, and G. A. Mourou, “Papyrus imaging with terahertz time domain spectroscopy,” *Appl. Phys. A*, vol. 100, no. 3, pp. 607–612, Sep. 2010.
[63] K. Fukunaga, T. Ikari, and K. Iwai, “THz pulsed time-domain imaging of an oil canvas painting: a case study of a painting by Pablo Picasso,” *Appl. Phys. A*, vol. 122, no. 2, p. 106, Feb. 2016.
[64] M. Picollo, K. Fukunaga, and J. Labaune, “Obtaining noninvasive stratigraphic details of panel paintings using terahertz time domain spectroscopy imaging system,” *J. Cult. Herit.*, vol. 16, no. 1, pp. 73–80, Jan. 2015.
[65] C. L. K. Dandolo, M. Picollo, C. Cucci, and P. U. Jepsen, “Non-invasive Florentine Renaissance Panel Painting Replica Structures Investigation by Using Terahertz Time-Domain Imaging (THz-TDI) Technique,” *J. Infrared Millim. Terahertz Waves*, vol. 37, no. 11, pp. 1148–1156, Nov. 2016.
[66] K. Fukunaga and M. Picollo, “Terahertz spectroscopy applied to the analysis of artists’ materials,” *Appl. Phys. A*, vol. 100, no. 3, pp. 591–597, Sep. 2010.
[67] M. R. Leahy-Hoppa, M. J. Fitch, X. Zheng, L. M. Hayden, and R. Osiander, “Wideband terahertz spectroscopy of explosives,” *Chem. Phys. Lett.*, vol. 434, no. 4–6, pp. 227–230, Feb. 2007.
[68] Y. C. Shen, T. Lo, P. F. Taday, B. E. Cole, W. R. Tribe, and M. C. Kemp, “Detection and identification of explosives using terahertz pulsed spectroscopic imaging,” *Appl. Phys. Lett.*, vol. 86, no. 24, p. 241116, 2005.

[69] M. C. Kemp, P. F. Taday, B. E. Cole, J. A. Cluff, A. J. Fitzgerald, and W. R. Tribe, “Security applications of terahertz technology,” 2003, vol. 5070, pp. 44–52.
[70] J. F. Federici *et al.*, “THz imaging and sensing for security applications—explosives, weapons and drugs,” *Semicond. Sci. Technol.*, vol. 20, no. 7, p. S266, 2005.
[71] *THz and Security Applications - Detectors, Sources and | Carlo Corsi | Springer*. .
[72] K. Shiraga, Y. Ogawa, T. Suzuki, N. Kondo, A. Irisawa, and M. Imamura, “Characterization of Dielectric Responses of Human Cancer Cells in the Terahertz Region,” *J. Infrared Millim. Terahertz Waves*, vol. 35, no. 5, pp. 493–502, May 2014.
[73] M. Grognot and G. Gallot, “Quantitative measurement of permeabilization of living cells by terahertz attenuated total reflection,” *Appl. Phys. Lett.*, vol. 107, no. 10, p. 103702, Sep. 2015.
[74] P. H. Siegel, “Terahertz technology in biology and medicine,” *IEEE Trans. Microw. Theory Tech.*, vol. 52, no. 10, pp. 2438–2447, Oct. 2004.
[75] E. P. J. Parrott, Y. Sun, and E. Pickwell-MacPherson, “Terahertz spectroscopy: Its future role in medical diagnoses,” *J. Mol. Struct.*, vol. 1006, no. 1–3, pp. 66–76, Dec. 2011.
[76] X. Yang *et al.*, “Rapid and label-free detection and assessment of bacteria by terahertz time-domain spectroscopy,” *J. Biophotonics*, vol. 9, no. 10, pp. 1050–1058, Oct. 2016.
[77] A. Ramundo Orlando and G. P. Gallerano, “Terahertz Radiation Effects and Biological Applications,” *J. Infrared Millim. Terahertz Waves*, Aug. 2009.
[78] M. Nagel, M. Först, and H. Kurz, “THz biosensing devices: fundamentals and technology,” *J. Phys. Condens. Matter*, vol. 18, no. 18, pp. S601–S618, May 2006.
[79] S. Jia *et al.*, “THz Wireless Transmission Systems Based on Photonic Generation of Highly Pure Beat-Notes,” *IEEE Photonics J.*, vol. 8, no. 5, pp. 1–8, Oct. 2016.
[80] S. Koenig *et al.*, “Wireless sub-THz communication system with high data rate,” *Nat. Photonics*, vol. 7, no. 12, pp. 977–981, Dec. 2013.
[81] T. Nagatsuma, G. Ducournau, and C. C. Renaud, “Advances in terahertz communications accelerated by photonics,” *Nat Photon*, vol. 10, no. 6, pp. 371–379, Jun. 2016.
[82] R. Piesiewicz, M. Jacob, M. Koch, J. Schoebel, and T. Kurner, “Performance analysis of future multigigabit wireless communication systems at THz frequencies with highly directive antennas in realistic indoor environments,” *IEEE J. Sel. Top. Quantum Electron.*, vol. 14, no. 2, pp. 421–430, 2008.
[83] K. R. Jha and G. Singh, *Terahertz Planar Antennas for Next Generation Communication*. Cham: Springer International Publishing, 2014.
[84] J. Federici and L. Moeller, “Review of terahertz and subterahertz wireless communications,” *J. Appl. Phys.*, vol. 107, no. 11, p. 111101, 2010.
[85] I. A. Ibraheem, N. Krumbholz, D. Mittleman, and M. Koch, “Low-Dispersive Dielectric Mirrors for Future Wireless Terahertz Communication Systems,” *IEEE Microw. Wirel. Compon. Lett.*, vol. 18, no. 1, pp. 67–69, Jan. 2008.
[86] T. Kleine-Ostmann, K. Pierz, G. Hein, P. Dawson, and M. Koch, “Audio signal transmission over THz communication channel using semiconductor modulator,” *Electron. Lett.*, vol. 40, no. 2, p. 1, 2004.
[87] K.-E. Peiponen, J. A. Zeitler, and M. Kuwata-Gonokami, Eds., *Terahertz spectroscopy and imaging*. Berlin: Springer, 2013.
[88] E. Castro-Camus and M. Alfaro, “Photoconductive devices for terahertz pulsed spectroscopy: a review [Invited],” *Photonics Res.*, vol. 4, no. 3, pp. A36–A42, Jun. 2016.
[89] “Menlo Systems.” [Online]. Available: http://www.menlosystems.com/.
[90] “TOPTICA Photonics AG,” *TOPTICA Photonics AG*, 11-Jan-2017. [Online]. Available: http://www.toptica.com/.
[91] F. Miyamaru, Y. Saito, K. Yamamoto, T. Furuya, S. Nishizawa, and M. Tani, “Dependence of emission of terahertz radiation on geometrical parameters of dipole photoconductive antennas,” *Appl. Phys. Lett.*, vol. 96, no. 21, p. 211104, May 2010.
[92] K. Sakai, Ed., *Terahertz optoelectronics*. Berlin: Springer, 2005.
[93] H.-J. Song and T. Nagatsuma, *Handbook of Terahertz Technologies: Devices and Applications*. CRC Press, 2015.

[94] J. Barros *et al.*, “Coherent synchrotron radiation for broadband terahertz spectroscopy,” *Rev. Sci. Instrum.*, vol. 84, no. 3, p. 033102, Mar. 2013.
[95] K. A. McIntosh, E. R. Brown, K. B. Nichols, O. B. McMahon, W. F. DiNatale, and T. M. Lyszczarz, “Terahertz photomixing with diode lasers in low-temperature-grown GaAs,” *Appl. Phys. Lett.*, vol. 67, no. 26, pp. 3844–3846, Dec. 1995.
[96] S. Preu, G. H. Döhler, S. Malzer, L. J. Wang, and A. C. Gossard, “Tunable, continuous-wave Terahertz photomixer sources and applications,” *J. Appl. Phys.*, vol. 109, no. 6, p. 061301, Mar. 2011.
[97] J. Faist, F. Capasso, D. L. Sivco, C. Sirtori, A. L. Hutchinson, and A. Y. Cho, “Quantum Cascade Laser,” *Science*, vol. 264, no. 5158, p. 553, Apr. 1994.
[98] R. Köhler *et al.*, “Terahertz semiconductor-heterostructure laser,” *Nature*, vol. 417, no. 6885, pp. 156–159, May 2002.
[99] B. S. Williams, “Terahertz quantum-cascade lasers,” *Nat. Photonics*, vol. 1, no. 9, pp. 517–525, 2007.
[100] M. S. Vitiello and A. Tredicucci, “Tunable Emission in THz Quantum Cascade Lasers,” *IEEE Trans. Terahertz Sci. Technol.*, vol. 1, no. 1, pp. 76–84, Sep. 2011.
[101] M. S. Vitiello, G. Scalari, B. Williams, and P. D. Natale, “Quantum cascade lasers: 20 years of challenges,” *Opt. Express*, vol. 23, no. 4, pp. 5167–5182, Feb. 2015.
[102] A. Wade *et al.*, “Magnetic-field-assisted terahertz quantum cascade laser operating up to 225 K,” *Nat. Photonics*, vol. 3, no. 1, pp. 41–45, Jan. 2009.
[103] “Zoterac.” [Online]. Available: http://www.zoterac.eu/.
[104] G. L. Carr, M. C. Martin, W. R. McKinney, K. Jordan, G. R. Neil, and G. P. Williams, “High-power terahertz radiation from relativistic electrons,” *Nature*, vol. 420, no. 6912, pp. 153–156, Nov. 2002.
[105] “Virginia Diodes.” [Online]. Available: http://www.vadiodes.com/index.php/en/.
[106] F. Sizov, “THz radiation sensors,” *Opto-Electron. Rev.*, vol. 18, no. 1, pp. 10–36, 2009.
[107] “Terahertz Spectroscopy: Principles and Applications,” *CRC Press*, 22-Dec-2007. [Online]. Available: https://www.crcpress.com/Terahertz-Spectroscopy-Principles-and-Applications/Dexheimer/p/book/9780849375255.
[108] Q. Wu, M. Litz, and X.-C. Zhang, “Broadband detection capability of ZnTe electro-optic field detectors,” *Appl. Phys. Lett.*, vol. 68, no. 21, pp. 2924–2926, 1996.
[109] H.-W. Hubers, “Terahertz Heterodyne Receivers,” *IEEE J. Sel. Top. Quantum Electron.*, vol. 14, no. 2, pp. 378–391, 2008.
[110] M. Perenzoni, Ed., *Physics and applications of terahertz radiation*. Dordrecht: Springer, 2014.
[111] D. C. Zografopoulos and R. Beccherelli, “Tunable terahertz fishnet metamaterials based on thin nematic liquid crystal layers for fast switching,” *Sci. Rep.*, vol. 5, p. 13137, Aug. 2015.
[112] G. Isić, B. Vasić, D. C. Zografopoulos, R. Beccherelli, and R. Gajić, “Electrically Tunable Critically Coupled Terahertz Metamaterial Absorber Based on Nematic Liquid Crystals,” *Phys. Rev. Appl.*, vol. 3, no. 6, p. 064007, Jun. 2015.
[113] Y. Fan, N.-H. Shen, T. Koschny, and C. M. Soukoulis, “Tunable Terahertz Meta-Surface with Graphene Cut-Wires,” *ACS Photonics*, vol. 2, no. 1, pp. 151–156, Jan. 2015.
[114] L. Wang *et al.*, “Broadband tunable liquid crystal terahertz waveplates driven with porous graphene electrodes,” *Light Sci. Appl.*, vol. 4, no. 2, p. e253, Feb. 2015.
[115] R. Yan, S. Arezoomandan, B. Sensale-Rodriguez, and H. G. Xing, “Exceptional Terahertz Wave Modulation in Graphene Enhanced by Frequency Selective Surfaces,” *ACS Photonics*, vol. 3, no. 3, pp. 315–323, Mar. 2016.
[116] P. D. Cunningham *et al.*, “Broadband terahertz characterization of the refractive index and absorption of some important polymeric and organic electro-optic materials,” *J. Appl. Phys.*, vol. 109, no. 4, p. 043505, 2011.
[117] “TOPAS.” [Online]. Available: http://www.topas.com/.
[118] Y.-S. Jin, G.-J. Kim, and S.-G. Jeon, “Terahertz dielectric properties of polymers,” *J. Korean Phys. Soc.*, vol. 49, no. 2, pp. 513–517, 2006.
[119] B. Ung, A. Mazhorova, A. Dupuis, M. Rozé, and M. Skorobogatiy, “Polymer microstructured optical fibers for terahertz wave guiding,” *Opt. Express*, vol. 19, no. 26, pp. B848–B861, 2011.

[120] M. Naftaly, A. P. Foulds, R. E. Miles, and A. G. Davies, “Terahertz Transmission Spectroscopy of Nonpolar Materials and Relationship with Composition and Properties,” *Int. J. Infrared Millim. Waves*, vol. 26, no. 1, pp. 55–64, Jan. 2005.
[121] C. Brückner, B. Pradarutti, R. Müller, S. Riehemann, G. Notni, and A. Tünnermann, “Design and evaluation of a THz time domain imaging system using standard optical design software,” *Appl. Opt.*, vol. 47, no. 27, pp. 4994–5006, Sep. 2008.
[122] “TYDEX Research&Industrial Optics.” [Online]. Available: http://www.tydexoptics.com/.
[123] A. Dupuis, K. Stoeffler, B. Ung, C. Dubois, and M. Skorobogatiy, “Transmission measurements of hollow-core THz Bragg fibers,” *JOSA B*, vol. 28, no. 4, pp. 896–907, 2011.
[124] “ZEON CORPORATION.” [Online]. Available: http://www.zeon.co.jp/index_e.html.
[125] K. Obuchi, M. Komatsu, and K. Minami, “High performance optical materials cyclo olefin polymer ZEONEX,” 2007, vol. 6671, p. 66711I–66711I–9.
[126] L. Ren *et al.*, “Broadband Terahertz Polarizers with Ideal Performance Based on Aligned Carbon Nanotube Stacks,” *Nano Lett.*, vol. 12, no. 2, pp. 787–790, Feb. 2012.
[127] C.-F. Hsieh, Y.-C. Lai, R.-P. Pan, and C.-L. Pan, “Polarizing terahertz waves with nematic liquid crystals,” *Opt. Lett.*, vol. 33, no. 11, pp. 1174–1176, 2008.
[128] W. Zhang *et al.*, “Thz polarizer using tunable metamaterials,” in *Micro Electro Mechanical Systems (MEMS), 2013 IEEE 26th International Conference on*, 2013, pp. 713–716.
[129] K. Shiraishi, S. Oyama, and C. S. Tsai, “A Polarizer Using Thin Metallic-Film Subwavelength Grating for Infrared to Terahertz Region,” *J. Light. Technol.*, vol. 29, no. 5, pp. 670–676, Mar. 2011.
[130] K. Shiraishi and K. Muraki, “Metal-film subwavelength-grating polarizer with low insertion losses and high extinction ratios in the terahertz region,” *Opt. Express*, vol. 23, no. 13, p. 16676, Jun. 2015.
[131] M. Aghadjani and P. Mazumder, “THz Polarizer Controller Based on Cylindrical Spoof Surface Plasmon Polariton (C-SSPP),” *IEEE Trans. Terahertz Sci. Technol.*, vol. 5, no. 4, pp. 556–563, Jul. 2015.
[132] http://www.tydexoptics.com, “TYDEX THz Band Pass Filters.” [Online]. Available: http://www.tydexoptics.com/products/thz_optics/thz_band_pass_filter/. [Accessed: 19-Dec-2016].
[133] “Microtech Instruments, Inc. - THz Components & Systems.” [Online]. Available: http://www.mtinstruments.com/.
[134] I. Yamada, K. Takano, M. Hangyo, M. Saito, and W. Watanabe, “Terahertz wire-grid polarizers with micrometer-pitch Al gratings,” *Opt. Lett.*, vol. 34, no. 3, pp. 274–276, 2009.
[135] Z. Huang, H. Park, E. P. J. Parrott, H. P. Chan, and E. Pickwell-MacPherson, “Robust Thin-Film Wire-Grid THz Polarizer Fabricated Via a Low-Cost Approach,” *IEEE Photonics Technol. Lett.*, vol. 25, no. 1, pp. 81–84, Jan. 2013.
[136] Z. Huang, E. P. J. Parrott, H. Park, H. P. Chan, and E. Pickwell-MacPherson, “High extinction ratio and low transmission loss thin-film terahertz polarizer with a tunable bilayer metal wire-grid structure,” *Opt. Lett.*, vol. 39, no. 4, p. 793, Feb. 2014.
[137] Y. Kishi, M. Nagai, J. C. Young, K. Takano, M. Hangyo, and T. Suzuki, “Terahertz laminated-structure polarizer with high extinction ratio and transmission power,” *Appl. Phys. Express*, vol. 8, no. 3, p. 032201, Mar. 2015.
[138] K. Takano, H. Yokoyama, A. Ichii, I. Morimoto, and M. Hangyo, “Wire-grid polarizer sheet in the terahertz region fabricated by nanoimprint technology,” *Opt. Lett.*, vol. 36, no. 14, pp. 2665–2667, 2011.
[139] A. Ferraro, D. C. Zografopoulos, M. Missori, M. Peccianti, R. Caputo, and R. Beccherelli, “Flexible terahertz wire grid polarizer with high extinction ratio and low loss,” *Opt. Lett.*, vol. 41, no. 9, pp. 2009–2012, May 2016.
[140] A. Ferraro, D. C. Zografopoulos, R. Caputo, and R. Beccherelli, “Terahertz polarizing component on cyclo-olefin polymer,” *submitted*.
[141] S. Khan, L. Lorenzelli, and R. S. Dahiya, “Technologies for Printing Sensors and Electronics Over Large Flexible Substrates: A Review,” *IEEE Sens. J.*, vol. 15, no. 6, pp. 3164–3185, Jun. 2015.
[142] G. Grau, R. Kitsomboonloha, and V. Subramanian, “Fabrication of a high-resolution roll for gravure printing of 2µm features,” 2015, p. 95680M.

[143] F. Yan, C. Yu, H. Park, E. P. J. Parrott, and E. Pickwell-MacPherson, “Advances in Polarizer Technology for Terahertz Frequency Applications,” *J. Infrared Millim. Terahertz Waves*, vol. 34, no. 9, pp. 489–499, 2013.
[144] A. Ferraro, D. C. Zografopoulos, R. Caputo, and R. Beccherelli, “Periodical Elements as Low-Cost Building Blocks for Tunable Terahertz Filters,” *IEEE Photonics Technol. Lett.*, vol. 28, no. 21, pp. 2459–2462, Nov. 2016.
[145] N. Born *et al.*, “Terahertz Metamaterials with Ultrahigh Angular Sensitivity,” *Adv. Opt. Mater.*, vol. 3, no. 5, pp. 642–645, 2015.
[146] H.-A. Lin, H.-Y. Hsu, C.-W. Chang, and C.-S. Huang, “Compact spectrometer system based on a gradient grating period guided-mode resonance filter,” *Opt. Express*, vol. 24, no. 10, p. 10972, May 2016.
[147] R. J. Williams, A. J. Gatesman, T. M. Goyette, and R. H. Giles, “Radar cross section measurements of frequency selective terahertz retroreflectors,” 2014, p. 91020R.
[148] L. Minkevičius *et al.*, “Focusing Performance of Terahertz Zone Plates with Integrated Cross-shape Apertures,” *J. Infrared Millim. Terahertz Waves*, vol. 35, no. 9, pp. 699–702, Sep. 2014.
[149] S. T. Chase and R. D. Joseph, “Resonant array bandpass filters for the far infrared,” *Appl. Opt.*, vol. 22, no. 11, pp. 1775–1779, Jun. 1983.
[150] D. W. Porterfield, J. L. Hesler, R. Densing, E. R. Mueller, T. W. Crowe, and R. M. Weikle, “Resonant metal-mesh bandpass filters for the far infrared,” *Appl. Opt.*, vol. 33, no. 25, pp. 6046–6052, 1994.
[151] M. E. MacDonald, A. Alexanian, R. A. York, Z. Popovic, and E. N. Grossman, “Spectral transmittance of lossy printed resonant-grid terahertz bandpass filters,” *IEEE Trans. Microw. Theory Tech.*, vol. 48, no. 4, pp. 712–718, 2000.
[152] B. Voisiat, A. Bičiūnas, I. Kašalynas, and G. Račiukaitis, “Band-pass filters for THz spectral range fabricated by laser ablation,” *Appl. Phys. A*, vol. 104, no. 3, pp. 953–958, Sep. 2011.
[153] Y. Ma, A. Khalid, T. D. Drysdale, and D. R. Cumming, “Direct fabrication of terahertz optical devices on low-absorption polymer substrates,” *Opt. Lett.*, vol. 34, no. 10, pp. 1555–1557, 2009.
[154] A. C. Strikwerda, M. Zalkovskij, D. Lund Lorenzen, A. Krabbe, A. V. Lavrinenko, and P. Uhd Jepsen, “Metamaterial composite bandpass filter with an ultra-broadband rejection bandwidth of up to 240 terahertz,” *Appl. Phys. Lett.*, vol. 104, no. 19, p. 191103, May 2014.
[155] O. Paul, R. Beigang, and M. Rahm, “Highly selective terahertz bandpass filters based on trapped mode excitation,” *Opt. Express*, vol. 17, no. 21, pp. 18590–18595, 2009.
[156] L. Liang *et al.*, “A flexible wideband bandpass terahertz filter using multi-layer metamaterials,” *Appl. Phys. B*, vol. 113, no. 2, pp. 285–290, Nov. 2013.
[157] D. S. Wang, B. J. Chen, and C. H. Chan, “High-Selectivity Bandpass Frequency-Selective Surface in Terahertz Band,” *IEEE Trans. Terahertz Sci. Technol.*, vol. 6, no. 2, pp. 284–291, Mar. 2016.
[158] Y.-J. Chiang, C.-S. Yang, Y.-H. Yang, C.-L. Pan, and T.-J. Yen, “An ultrabroad terahertz bandpass filter based on multiple-resonance excitation of a composite metamaterial,” *Appl. Phys. Lett.*, vol. 99, no. 19, p. 191909, 2011.
[159] R. Magnusson and S. S. Wang, “New principle for optical filters,” *Appl. Phys. Lett.*, vol. 61, no. 9, p. 1022, 1992.
[160] R. Magnusson and S. S. Wang, “Transmission bandpass guided-mode resonance filters,” *Appl. Opt.*, vol. 34, no. 35, pp. 8106–8109, 1995.
[161] E. Sakat *et al.*, “Guided mode resonance in subwavelength metallodielectric free-standing grating for bandpass filtering,” *Opt. Lett.*, vol. 36, no. 16, pp. 3054–3056, Aug. 2011.
[162] E. Sakat *et al.*, “Free-standing guided-mode resonance band-pass filters: from 1D to 2D structures,” *Opt. Express*, vol. 20, no. 12, pp. 13082–13090, 2012.
[163] Z. S. Liu, S. Tibuleac, D. Shin, P. P. Young, and R. Magnusson, “High-efficiency guided-mode resonance filter,” *Opt. Lett.*, vol. 23, no. 19, pp. 1556–1558, 1998.
[164] S. Song, F. Sun, Q. Chen, and Y. Zhang, “Narrow-Linewidth and High-Transmission Terahertz Bandpass Filtering by Metallic Gratings,” *IEEE Trans. Terahertz Sci. Technol.*, vol. 5, p. 131, 2015.

[165] Ferraro A., Zografopoulos D. C., Caputo R., and Beccherelli R., “Broad- and narrow-line terahertz filtering in frequency-selective surfaces patterned on thin low-loss polymer substrates,” *IEEE J. Sel. Top. Quantum Electron.*, vol. accepted, 2017.
[166] A. Ferraro, D. C. Zografopoulos, R. Caputo, and R. Beccherelli, “Angle-resolved and polarization-dependent investigation of cross-shaped frequency-selective surface terahertz filters,” *submitted*.
[167] F. Medina, F. Mesa, and R. Marques, “Extraordinary Transmission Through Arrays of Electrically Small Holes From a Circuit Theory Perspective,” *IEEE Trans. Microw. Theory Tech.*, vol. 56, no. 12, pp. 3108–3120, Dicembre 2008.
[168] J. Marae-Djouda *et al.*, “Angular plasmon response of gold nanoparticles arrays: approaching the Rayleigh limit,” *Nanophotonics*, vol. 6, no. 1, pp. 279–288, 2016.
[169] “OMS.” [Online]. Available: http://www.computational-photonics.eu/oms.html.
[170] S. Peng and G. M. Morris, “Resonant scattering from two-dimensional gratings,” *JOSA A*, vol. 13, no. 5, pp. 993–1005, 1996.
[171] A. M. Melo, A. L. Gobbi, M. H. O. Piazzetta, and A. M. P. A. da Silva, “Cross-Shaped Terahertz Metal Mesh Filters: Historical Review and Results,” *Adv. Opt. Technol.*, vol. 2012, pp. 1–12, 2012.
[172] “Thorlabs, Inc.” [Online]. Available: https://www.thorlabs.com/.
[173] S. S. Wang and R. Magnusson, “Theory and applications of guided-mode resonance filters,” *Appl. Opt.*, vol. 32, no. 14, pp. 2606–2613, 1993.
[174] R. Magnusson, J. W. Yoon, M. S. Amin, T. Khaleque, and M. J. Uddin, “Extraordinary capabilities of optical devices incorporating guided-mode resonance gratings: application summary and recent examples,” 2014, p. 89880I.
[175] A. Ferraro, D. C. Zografopoulos, R. Caputo, and R. Beccherelli, “Squeezing narrow band terahertz radiation through extremely subwavelength slits in guided-mode resonant cyclo-olefin thin films,” *submitted*.
[176] Y.-K. Tu, M.-Z. Tsai, I.-C. Lee, H.-Y. Hsu, and C.-S. Huang, “Integration of a guided-mode resonance filter with microposts for in-cell protein detection,” *The Analyst*, vol. 141, no. 13, pp. 4189–4195, 2016.
[177] G. Niederer, H. P. Herzig, J. Shamir, H. Thiele, M. Schnieper, and C. Zschokke, “Tunable, oblique incidence resonant grating filter for telecommunications,” *Appl. Opt.*, vol. 43, no. 8, pp. 1683–1694, 2004.
[178] S. S. Wang and R. Magnusson, “Design of waveguide-grating filters with symmetrical line shapes and low sidebands,” *Opt. Lett.*, vol. 19, no. 12, pp. 919–921, 1994.
[179] S. T. Thurman and G. M. Morris, “Controlling the spectral response in guided-mode resonance filter design,” *Appl. Opt.*, vol. 42, no. 16, pp. 3225–3233, 2003.
[180] X. Fu, K. Yi, J. Shao, and Z. Fan, “Nonpolarizing guided-mode resonance filter,” *Opt. Lett.*, vol. 34, no. 2, pp. 124–126, 2009.
[181] A. P. Hibbins, J. R. Sambles, C. R. Lawrence, and J. R. Brown, “Squeezing Millimeter Waves into Microns,” *Phys. Rev. Lett.*, vol. 92, no. 14, p. 143904, Apr. 2004.
[182] B. Scherger, M. Scheller, N. Vieweg, S. T. Cundiff, and M. Koch, “Paper terahertz wave plates,” *Opt. Express*, vol. 19, no. 25, pp. 24884–24889, Dec. 2011.
[183] H. A. Macleod, *Thin-film optical filters*, 4. ed. Boca Raton, Fla.: CRC Press, 2010.
[184] C. J. R. Sheppard, “Approximate calculation of the reflection coefficient from a stratified medium,” *Pure Appl. Opt. J. Eur. Opt. Soc. Part A*, vol. 4, no. 5, p. 665, 1995.